NASA Contractor Report 174916

Predictions and Measurements of Isothermal Flowfields in Axisymmetric Combustor Geometries

D.L. Rhode and D.G. Lilley

Oklahoma State University
Stillwater, Oklahoma

May 1985

Prepared for
Lewis Research Center
Under Grant NAG 3-74

National Aeronautics and
Space Administration

TABLE OF CONTENTS

Chapter		Page
I.	INTRODUCTION	1
	1.1 Combustor Design and Development	1
	1.2 Practical Needs and the Present Research	2
	1.3 Theoretical Investigation	3
	1.4 Experimental Investigation	4
	1.5 Swirl Flow Concepts	5
	1.6 The Present Contribution	7
II.	REVIEW OF PREVIOUS AXISYMMETRIC RECIRCULATING FLOW STUDIES	9
	2.1 Experimental Work in Nonswirling Flows	9
	2.2 Experimental Work in Swirling Flows	11
	2.3 Theoretical Work in Nonswirling Flows	13
	2.4 Theoretical Work in Swirling Flows	14
III.	COMPUTATIONAL TECHNIQUES	19
	3.1 The Governing Equation	20
	3.2 The Finite Difference Formulation	21
	3.3 The Solution Procedure	23
IV.	EXPERIMENTAL FACILITY AND TECHNIQUES	25
	4.1 Wind Tunnel	25
	4.2 Test Section	26
	4.3 Flow Visualization	27
	4.4 Mean Velocity Measurements	35
V.	GROSS FLOWFIELD CHARACTERIZATION	44
	5.1 Artistic Impressions of Streamline Patterns From Flow Visualization	44
	5.2 Flow Visualization Results	46
	5.3 Predicted Streamline Patterns	51
	5.4 Parametric Effects	53
VI.	VELOCITY MEASUREMENTS, PREDICTIONS, AND COMPARISON WITH EXPERIMENT	55
	6.1 Five-Hole Pitot Probe Velocity Measurements	55
	6.2 General Velocity Predictions	58
	6.3 The Specific Test Case	60

Chapter Page

6.4 Reliability of Predictions and Measurements 61
6.5 Prediction of Coannular Swirling Pipe Flow 64

VII. CLOSURE 68

7.1 Conclusions 68
7.2 Recommendations for Further Work 70

REFERENCES 71

APPENDIX A - TABLE 79

APPENDIX B - FIGURES 80

APPENDIX C - DATA REDUCTION COMPUTER PROGRAM FOR FIVE-HOLE PITOT PROBE MEASUREMENTS 157

NOMENCLATURE

a	coupling coefficient
C	constant
D	test section diameter
d	inlet nozzle diameter
G	axial flux of momentum; k-generation term
I, J	mesh point indices
k	kinetic energy of turbulence
p	time-mean pressure
R	residual source; radius of test chamber
Re	Reynolds number
S	swirl number = $2G_\theta/(G_x D)$; source term (with subscript)
S_P, S_U	components of linearized source term
$\underline{v} = (u, v, w)$	time-mean velocity (in x-, r-, θ-directions)
V, $\bar{V}$	time-mean vector velocity magnitude
x, r, θ	axial, radial, azimuthal cylindrical polar coordinates
α	side-wall expansion angle
β	yaw angle of probe
Γ	turbulent exchange coefficient
δ	pitch angle of probe
ε	turbulence energy dissipation rate
μ	effective viscosity
ρ	time-mean density
σ	Prandtl-Schmidt number

ϕ	swirl vane angle [$\tan^{-1}$ (w_{in}/u_{in}), assuming perfect vanes]; general dependent variable
ψ	probe rotation angle

Superscripts

$(\ )'$	turbulent fluctuation of quantity
$(\overline{\ })$	time-average of quantity
u, v, w	axial, radial, swirl momentum

Subscripts

C	central pitot pressure
in	inlet conditions
n, s, e, w	north, south, east, west faces of cell
o	value at inlet to flowfield
P, N, S, E, W	point, north, south, east, west neighbors; north, south, east, west pitot pressures
h	swirl vane hub; expansion step height
ℓ	laminar value
p	probe sensing tip

CHAPTER I

INTRODUCTION

1.1 Combustor Design and Development

The combustor of the gas turbine engine illustrated in Figure 1 contains high intensity combustion and, as far as possible, must burn fuel completely, cause little pressure drop, produce gases of nearly uniform temperature, occupy small volume, and maintain stable combustion over a wide range of operating conditions (1). Efforts are continually being expended to produce efficient clean combustion. The designer has a formidable problem in aerothermochemistry, and more accurate analysis procedures can provide a route which leads to the accomplishment of design objectives more quickly and less expensively than current practice permits (2, 3).

In design situations, the engineer has to seek an optimum path between alternatives of, for example, efficiency and pollution. The general aim of most research investigation is to provide information which is useful to designers by "characterizing" or "modeling" certain features of the phenomenon in question. Investigations may be theoretical or experimental; the two approaches are complementary. Until recently, designers have relied heavily on the experimental approach, but traditional design methods (empirical formulas and experimentation) are now being supplemented by analytical methods (numerical solution of the appropriate governing partial differential equations). The mathematical modeling

approach is now finding favor and is being used to supplement existing design procedures. Current combustor design and development problems, the needs of the combustion engineer in practice, and proposed research tasks which will assist in the attainment of design objectives are becoming clear. Improvements and new developments (both experimental and theoretical) can and should be made, theoretical modeling being aided by specific carefully chosen experiments (4).

1.2 Practical Needs and the Present Research

Many details of combustor phenomena remain poorly understood at the macroscopic as well as the microscopic level. Knowledge of these will undoubtedly reduce combustor development time and cost substantially, and lead to increases in performance. Some of these research needs are:

1. Physical processes--turbulence, radiation, combustion, and multiphase effects.

2. Computer programs--0-, 1-, 2-, and 3-dimensional approaches in steady state and transient cases.

3. Unresolved problems--effect of swirl, recirculation, and wall proximity on turbulence; turbulence-reaction interaction; and multiphase simulation.

The present research work is concerned with complementary experimental and theoretical studies on a specific subproblem of this general problem and is described in a recent paper (5). The specific problem being investigated experimentally is concerned with steady turbulent flow in axisymmetric geometries, under low speed and nonreacting conditions--a study area highlighted recently as a fundamental research requirement in combustion modeling (2, 6, 7). The particular problem is concerned with

turbulent flow of a given turbulence distribution in a round pipe entering an expansion into another round pipe, as illustrated in Figure 2. The in-coming flow may possess a swirl component of velocity via passage through swirl vanes at angle ϕ (equal approximately to $\tan^{-1}[w_{in}/u_{in}]$), and the side-wall may slope at an angle α, to the main flow direction. The resulting flowfield domain may possess a central toroidal recirculation zone in the middle of the region on the axis, in addition to the possibility of a corner recirculation zone near the upper corner provoked by the rather sudden enlargement of the cross-sectional area. Of vital concern is the characterization of flows of this type in terms of the effects of side-wall angle α, swirl vane angle ϕ, turbulence intensity k_{in} of the inlet stream, and expansion ratio D/d on the resulting flowfield in terms of its time-mean and turbulence quantities. Such problems have received little attention, yet there is a definite need for work in this area even under nonreacting flow conditions.

1.3 Theoretical Investigation

A mathematical solution of the flowfield of interest should provide results more economically, quickly, and correctly than possible by other means (for example, experiments on real-life systems or models). In order to achieve this, the model should simulate the flow in all its important respects (geometry, boundary conditions, physical properties of gases, turbulence, etc.) and provide a means whereby the governing equations may be solved. Mathematical models of steadily increasing realism and refinement are now being developed, both in the dimensionality of the model (together with the computational procedures) and in problems associated with the simulation of the physical processes occurring. Clearly there

are two areas of difficulty: the simulation and the solution. Recent publications discuss these difficulties in the context of combustor flowfield predictions (4, 5, 8, 9, 10).

An advanced prediction computer program, which solves the governing partial differential equations in finite difference form, has been developed. A detailed discussion of this program, including a user-oriented section, has been prepared recently (11). Therefore, extensive discussion of this program in Chapter III of this document is not necessary and only highlights of the technique are included.

1.4 Experimental Investigation

Prediction work in the form of computing the flowfield is being complemented by an associated experimental study which is used to evaluate the final predictive capability. The experiments, under way at Oklahoma State University, are concerned with measuring the effects of swirl and side-wall angle on streamlines as well as mean flow and turbulence parameters in nonreacting flow. Use is made of the confined jet facility shown schematically in Figure 3.

The facility has an axial flow fan whose speed can be changed by means of a varidrive mechanism. Numerous fine screens and straws produce flow in the settling chamber of relatively low turbulence intensity. The contraction section leading to the test section has been designed to produce a minimum adverse pressure gradient on the boundary layer and thus avoid unsteady problems associated with local separation regions. The sudden expansion consists of a 15 cm diameter circular jet nozzle, exiting abruptly into a 30 cm diameter test section, as shown in Figure 3.

The substantial size of this test model provides excellent probe resolution for five-hole pitot measurements. The test section is constructed of plexiglass to facilitate flow visualization. The side-wall angle and swirl vane angle ϕ are variable. The side-wall angle is set by inserting one of three blocks with a side-wall angle α of 90, 70, or 45 degrees. The swirl vane angle is continuously variable with discrete values of ϕ = 0, 45, and 70 degrees being chosen for the present study. The experiments are concerned with nonreacting flow, and the following two aspects of the study are addressed in the present thesis:

1. Photography of neutrally-buoyant helium-filled soap bubbles, tufts, and smoke, so as to characterize the time-mean streamlines, recirculation zones, and regions of highly turbulent flow.

2. Five-hole pitot probe pressure measurements to determine time-mean velocities u, v, and w.

Complete details of these experimental studies appear in Chapter IV.

1.5 Swirl Flow Concepts

Most practical combustion equipment includes the phenomenon of swirl and it is convenient to recall here some of the basic concepts of its generation and characterization (12). Swirling flows result from the application of a spiraling motion, with a swirl velocity component (also known as a tangential or azimuthal velocity component) being imparted to the flow via the use of swirl vanes, in an axial-plus-tangential entry swirl generator or by direct tangential entry into the combustion chamber. Experimental studies show that swirl has large scale effects on flowfields; jet growth, entrainment, and decay (for inert jets) and flame size, shape, stability, and combustion intensity (for reacting flows) are affected by

the degree of swirl imparted to the flow. This degree of swirl usually is characterized by the swirl number S, which is a nondimensional number representing axial flux of swirl momentum divided by axial flux of axial momentum times equivalent nozzle radius. That is

$$S = \frac{G_\theta}{G_x \; d/2} \tag{1.1}$$

where

$$G_\theta = \int_0^\infty (\rho uw + \rho \overline{u'w'}) \, r^2 \, dr$$

is the axial flux of swirl momentum, including the $x\theta$-direction turbulent shear stress term;

$$G_x = \int_0^\infty (\rho u^2 + \rho \overline{u'^2} + (p - p_\infty)) \, r \, dr$$

is the axial flux of axial momentum, including the x-direction turbulent normal stress term and a pressure term; d/2 is the nozzle radius; and u,v,w are velocity components in (x,r,θ) cylindrical polar coordinate directions.

In a free jet in stagnant surroundings, G_x and G_θ are constants, that is, invariants of the jet, as may be deduced from radial integration of the appropriate governing Reynolds equation (13).

It is especially convenient to be able to relate the angle of a swirl vane pack to the swirl number produced. In this context, for comparison purposes it is worth noting that swirl vane angle ϕ and swirl number S are related approximately by

$$S = \frac{2}{3}\left(\frac{1 - (d_h/d)^3}{1 - (d_h/d)^2}\right) \tan\phi \tag{1.2}$$

where d and d_h are nozzle and vane pack hub diameters, respectively. This relationship follows from assumptions of plug flow axial velocity u_o in the annular region, and very thin vanes at constant angle ϕ to the main direction so imparting a constant swirl velocity $w_o = u_o \tan\phi$ to the flow. From the G_x and G_θ definitions, integration over the range R_h (= $d_h/2$) to R (= d/2) gives

$$G_\theta = 2\pi\rho u_o^2 \left(\frac{R^3 - R_h^3}{3} \right) \tan\phi \tag{1.3a}$$

$$G_x = \pi\rho u_o^2 \, (R^2 - R_h^2) \tag{1.3b}$$

from which the quoted relationship follows. In the case of a hubless swirler (or one for which d_h/d is very small) the expression simplifies to

$$S = \frac{2}{3} \tan\phi \tag{1.4}$$

so that vane angles of 15, 30, 45, 60, 70, and 80 degrees, for example, correspond to S values of approximately 0.2, 0.4, 0.7, 1.2, 2.0, and 4.0. Here 100 percent efficiency also is assumed for the swirl vanes, which deteriorates as the vane angle increases. In fact, flat blades are not perfect, and indeed the assumption of flat axial and swirl velocity radial profiles immediately after the swirler is not correct, as may be seen from experimental measurements in Chapter VI of this thesis and elsewhere (12, 13, 14).

1.6 The Present Contribution

The basic objectives of the present research include the development of a computer code for the computation of swirling, axisymmetric, confined

jet flows using state-of-the-art computational procedures and the k-ε turbulence model. Further objectives entail mean flowfield measurements and flow visualization to characterize this particular flow and to evaluate the developed prediction procedure. The computations and experiments have been performed for six basic confined jet flowfields, all of which conform to the schematic diagram of Figure 2 and have an expansion ratio D/d = 2. The parameter combinations which define these flowfields are side-wall angle α = 90 and 45 degrees and swirl vane angle ϕ = 0, 45, and 70 degrees. The computational techniques are discussed in Chapter III.

The experimental program consisted of performing mean velocity measurements with a five-hole pitot probe and flow visualization of neutrally-buoyant soap bubbles, tufts, and smoke. Details of the experimental methods are presented in Chapter IV. The pitot probe measurements resulted in maps of axial, radial, and swirl velocity components while the flow visualization provided streamline patterns and recirculation zone geometries. Results of the overall flowfield characteristics highlighted by the recirculation region geometries, both predicted and visualized, are presented in Chapter V. Chapter VI contains results of predictions and measurements of time-mean velocity components. Finally, Chapter VII summarizes the conclusions of the present investigation and gives recommendations for further work.

CHAPTER II

REVIEW OF PREVIOUS AXISYMMETRIC RECIRCULATING FLOW STUDIES

Previous experimental and theoretical work in axisymmetric recirculating flows provides an important background for this investigation. Information regarding both swirling and nonswirling, nonreacting, turbulent flows has been extensively surveyed. Noteworthy results are included in the following summary where the emphasis is on nonreacting turbulent swirling flows.

2.1 Experimental Work in Nonswirling Flows

The effect of expansion angle α was investigated by Chaturvedi (15) who measured mean and turbulent flow quantities behind expansion half-angles of 15, 30, 45, and 90 degrees for air flow in a pipe. The expansion diameter ratio was 2.0. Measurements of velocity head in regions of high turbulence intensity and where the direction of the velocity vector was unknown were made with a 2.5 mm diameter pitot tube. Mean velocity was also measured with a constant temperature hot-wire anemometer using a single wire. A cross-wire was used to measure all the Reynolds stresses.

Krall and Sparrow (16) utilized an orifice in an electrically heated tube to create flow separation. It was presumed that the peak Nusselt number occurred at the reattachment point. Their results agreed with those of Phaneuf and Netzer (17) in that reattachment length was unaffected

by Reynolds number in the turbulent range. Also, they found that peak Nusselt number became spread out into a broad zone for strong separations caused by large step heights. This transition from a point to a broad zone occurred between h/D = 0.16 and h/D = 0.25, where D is the pipe diameter and h is the step height. Also, it was found that increasing the step height moved the peak point slightly downstream.

Back and Roschke (18, 19) investigated the reattachment length behind a pipe step by visual observation in water flows. The diameter expansion ratio was 2.6 and a conical contraction section just upstream reduced the boundary layer thickness. Small 0.76 mm diameter holes were located along the larger diameter tube one step height apart. Reattachment locations were determined by slowly metering dye through these holes and observing whether it moved upstream or downstream.

Wall static pressure was measured by Phaneuf and Netzer (17) as well as mean axial velocity behind abrupt pipe steps wherein the step heights were 0.303 and 0.195 outlet diameters. They found that the reattachment zone spreads out with both increasing Reynolds number (for a given step height) and increasing step height provided the Reynolds number is in the turbulence transition range. It was further concluded that the point of maximum heat transfer does not coincide with the zone of reattachment, and furthermore, it is dependent upon the inlet mass flux.

Ha Minh and Chassaing (20) studied the restructuration of a turbulent pipe flow past three types of geometric perturbations, one of which was the abrupt pipe expansion. Agreement between hot-wire and pitot probe measurements of time-mean axial velocity was exhibited. Owing to probe resolution considerations, only normal or inclined single wire

probes were used. All Reynolds stresses were measured, and the rotated inclined hot-wire technique was utilized.

Both a one-color and two-color laser-Doppler system were utilized by Moon and Rudinger (21) to measure mean axial velocities behind an abrupt pipe step. The diameter expansion ratio D/d was 1.43. Velocity reverses in the recirculation zone were easily detectable through use of a Bragg cell to shift the frequency of one probe beam relative to the other.

An experimental technique was developed by Johnson and Bennett (22) for measuring mean and fluctuating velocity and concentration distributions along with their cross correlations. Measurements were obtained using a laser-Doppler velocimeter to measure velocities, and a laser-induced fluorescence technique to measure the concentration of fluorescent tracer particles. Such measurements were displayed for coaxial jets discharging into a larger axisymmetric duct with D/d = 2.07.

2.2 Experimental Work in Swirling Flows

Both an aircraft and an industrial type combustor were investigated by Hiett and Powell (23) under reacting and nonreacting conditions. A water-cooled three-dimensional pitot probe was developed. Mean velocity profiles, recirculation boundaries, and temperature contours were presented. Also, cotton tufts were employed to visualize the nonreacting flow.

Extensive studies of free and enclosed swirling jets from vane swirlers were undertaken by Mathur and MacCallum (24). In the enclosed case, the expansion ratio was approximately D/d = 2.5 into a square-sectioned test section. An evaluation of swirler efficiency was conducted for both annular (with hub) and hubless swirlers. Extensive presentation is given

of velocity profiles and recirculation zone sizes as functions of the degree of inlet swirl.

Laser velocimeter measurements were made by Owen (25) in the initial mixing region of a confined turbulent diffusion flame burner. The experimental facility consisted of an axisymmetric combustor in which a central gaseous fuel stream mixed with a high speed coaxial annular air stream. The expansion diameter ratio was approximately 1.3 and swirl numbers of 0, 0.3, and 0.6 were chosen to contrast swirling with nonswirling combusting flowfields. Measurements were presented for axial and tangential mean velocity profiles along with the rms and probability density distributions of velocity fluctuations.

Three mean velocity components and normal stresses were measured with a laser anemometer by Baker et al. (26) in an experimental facility of a small scale axisymmetric furnace. The test chamber has an expansion diameter ratio of 3.33 and contains a constricted outlet. Measurements were obtained in both an isothermal air flow and a combusting mixture of natural gas and air, with exit swirl numbers of 0 and 0.52. The boundary and field measurements of three components of time-mean velocity and corresponding normal stresses were designed to be of good use in the evaluation of turbulent flow prediction procedures. It was clear from the results that regions of recirculation under reacting flow conditions differed substantially from those under nonreacting conditions. Surprisingly, they were found to be in general larger under reacting flow conditions. The turbulence was found to be far from isotropic over most of the flow field.

Beltaqui and MacCallum (27, 28) studied premixed vane swirled flames in furnaces with expansion ratios D/d = 2.5 and 5.0, where D and d are chamber and nozzle diameters, respectively. They found that a given vane

swirler can produce different velocity profiles as D is varied, and that the size and shape of the central recirculation zone are primarily functions of D rather than d. A modified swirl number using D rather than d was suggested as being more characteristic.

Mean velocity measurements were obtained by Vu and Gouldin (29) for coaxial jet mixing in a pipe under coswirl and counterswirl conditions. Both the central and annular flows had a swirl number of approximately 0.5. In the counterswirl case, a recirculation zone formed on the axis with very steep velocity gradients. In the coswirl case, no recirculation was observed.

Syred et al. (30) concentrated on turbulence measurements in strongly swirling flows via a single-wire six-orientation hot-wire technique. Local turbulence intensities were found to be extremely high in and near the central recirculation zone. Measurements of all six turbulent stress components showed strong variations of absolute turbulent kinetic energy levels and strong nonisotropy of the stresses and associated turbulent viscosity.

Further work of less importance to the present study is readily available (31, 32, 33, 34).

2.3 Theoretical Work in Nonswirling Flows

Laminar flow over a pipe step has been computed for the diameter expansion ratio 2.0 by Macagno and Hung (35). Computations for Reynolds numbers up to 200 were undertaken using stream function and vorticity variables. Flow visualization results were in good agreement with predicted values.

Runchal et al. (36) also predicted the flow downstream of a pipe step, solving transport equations for stream function, vorticity, enthalpy, and turbulence energy. The turbulence length scale was empirically determined to ensure that the reattachment point was accurately predicted. The effects of the outlet boundary condition are significant for only a short distance upstream, for example, one pipe diameter. The Stanton number was correctly predicted to vary as the -0.38 power of the Reynolds number.

As previously mentioned, Ha Minh and Chassaing (20) investigated the flow behind a pipe step. They obtained good agreement between measured and predicted values considering the extent of the flow perturbation. The k-ε turbulence model was employed for most of the computations, although the five-equation Reynolds stress transport model predicted the centerline kinetic energy more accurately.

Other predictive studies on nonswirling flow are discussed in section 2.4, where the emphasis is on swirling flows and in which the nonswirling case appears as a degenerate case. Selected theoretical work on turbulence modeling is also useful (37, 38, 39, 40).

2.4 Theoretical Work in Swirling Flows

Roberts (41) investigated similar axisymmetric, swirling flowfields by developing a finite difference code incorporating the k-W turbulence model while using stream function and vorticity variables. Poor performance of the k-W model led to the crude approach of specifying constant effective viscosities where $\mu_{axial}/\mu_{tangential} = 40$. Also, static wall pressures were measured and visualization information recorded for a water model experiment which gave general agreement with predictions.

Khalil et al. (42) predicted the flowfield of several two-dimensional model furnaces for which various measured quantities are available using a similar finite difference algorithm. As detailed knowledge of inlet boundary conditions are rarely known, a parametric study was undertaken, and results indicated that the inlet velocity profile has negligible effect. Also, provided that total enthalpy of the inlet flow is held constant, changes in the radial temperature profile exhibited a very small effect. However, it was found that inlet distributions of k and ε exert an appreciable influence, and of the three inlet k profiles tested for the flowfield measured by Baker et al. (26), values for k/u_o^2 of 0.009 for near wall nodes and 0.003 for central nodes gave closest agreement for axial velocity. Nonswirling flows are more sensitive to inlet profiles and thus the above numerical tests were conducted without swirl. Also, no significant differences could be observed for various outlet boundary conditions tested for axial velocity, enthalpy, mixture fraction, and concentration fluctuation.

An axisymmetric, combusting, swirling flow computer code was used by Hutchinson et al. (43) to compare predicted and measured quantities in the furnace test facility studied by Baker et al. (26) except at higher flow rates. The furnace consisted of a coaxial burner with swirling annular air flow and a constricted exit. Measurements of mean velocity and normal stress in both axial and tangential directions were generally predicted along with mean temperature and wall heat flux. Similar calculations using the same physical information but with a different numerical scheme showed that differences of up to 15 percent can be introduced by the numerical arrangement, whereas the rms differences were less than 5 percent. Discrepancies in axial velocity ranged up to 40 percent of the

maximum in the appropriate plane. The largest discrepancies were in the burner wake and it was suggested that the two-equation turbulence model is inadequate there.

A finite difference code was developed by Lilley (44) for inert and reacting recirculating flows with strong swirl. The effect of swirl number on mean axial and swirl velocities was presented along with predicted streamlines in an axisymmetric combustor. Also, the effect of swirl vane angle on central recirculation zone length and flame length was exhibited.

Serag-Eldin and Spalding (45) predicted the nonaxisymmetric, swirling, combusting flow in a can combustor with air entering through a 45-degree vane angle swirler in an annular tube enclosing a central jet of fuel. Temperature contours were measured with a bare 13 percent Rh-Pt versus Pt thermocouple wire of 3.8×10^{-3} mm diameter. Predicted results gave the same trend as measured ones, but quantitative agreement was not always acceptable.

Swirling, combusting flow in axisymmetric prechamber dump combustors was predicted by Novick et al. (46) using a finite difference procedure. Application of the computer code to specific combustor designs is stressed, and consideration is given to the relative effect of certain important design parameters: main chamber to prechamber expansion ratio, swirler dimensions, double concentric reverse swirler, constricted outlet, and fuel concentration profile. The standard base configuration consists of a 70-degree swirl vane angle inlet flow (stoichiometric mixture) which proceeds over a central hub, enters a prechamber, followed by a sudden expansion. Computed streamlines and temperature contours for this case are shown.

Details of the above model including physical assumptions, governing equations, finite difference equations, and solution procedure are found in a recent paper by Novick et al. (47). The predictive capability is demonstrated for a flowfield with coaxial jets entering a sudden expansion. Computed streamline patterns are presented for various swirl strengths with and without combustion in a prechamber dump combustor.

Other advances to prediction procedures have been made elsewhere and applied to other two-dimensional axisymmetric problems involving swirl flows in expansions of interest to the combustor designer. Habib and Whitelaw (48) compared hot-wire and laser measurements with predictions in confined coaxial jets with and without swirl.

Predictions of the swirl mixing pipe flow data of Vu and Gouldin (29) were made by Srinivasan and Mongia (49) for both coswirl and counterswirl cases. The measured inlet profiles were utilized as inlet boundary conditions with both the original k-ε turbulence model and the version extended to include Richardson number effects. The extended model gave better agreement with measurements, but the recirculation zone was somewhat elongated.

Sturgess and colleagues have predicted a variety of flow types with and without combustion as part of a continuing validation study of turbulence and reaction models for aircraft gas turbine combustor application (50, 51, 52). Associated sudden expansion experiments are yielding much needed data for this evaluation (22).

Lilley et al. (9) discussed the predicted effects of swirl vane angle ϕ and inlet side-wall expansion angle α on axisymmetric idealized gas turbine combustor flowfields. Also, the predicted effects of α and ϕ on both the corner and central recirculation zone lengths were presented, under

both reacting and nonreacting flow conditions, so extending earlier isothermal studies.

Other papers presented at a recent conference address turbulent reacting flows in practical combustion systems (53). The computation of flows with complex chemical kinetics problems, complex fluid mechanic problems, and complex simulation problems are all considered.

Fully three-dimensional flowfields are not specifically addressed in the present thesis. However, by way of introduction, interested readers are referred to the work of Mongia and Reynolds (54), Serag-Eldin and Spalding (45), and Swithenbank et al. (55). Mongia and Reynolds (54) developed and applied an advanced fully three-dimensional prediction technique to compute the reacting flowfield as part of an analytical design procedure for gas turbine combustion systems. Complexities such as the eddy-breakup chemical reaction model, and fuel spray droplet phenomena were included. Good qualitative agreement was found to be quite rewarding in developing a number of relatively complex combustion systems. Gaseous phase diffusion flames in can-type combustors have been predicted (45). Patterns of velocity and temperature show that qualitative trends may be simulated. A three-dimensional two-phase mathematical model of a Lycoming combustor has been amalgamated by Swithenbank et al. (55). Some 30 partial differential equations were solved and encouraging results were obtained.

CHAPTER III

COMPUTATIONAL TECHNIQUES

The economical design and operation of practical fluid flow equipment can be greatly facilitated by the availability of prior predictions of the flowfield. These may be obtained by use of a mathematical model incorporating a numerical finite difference solution procedure, and several textbooks discuss the approach at length (56, 57, 58). Several recent review papers also provide useful details (14, 37, 42, 44, 45, 47, 52, 59). These theoretical studies complement associated experimental studies, and their improvement and use can significantly increase understanding and reduce the time and cost of development work. In the context of the present study, the main goals include improved flowfield simulation and turbulence model development, and computer code development plays a significant role in this endeavor.

The computer program STARPIC (acronym for swirling turbulent axisymmetric recirculating flow in practical isothermal combustor geometries) has been developed and employed in the theoretical aspects of this investigation. It is used in a parametric study to predict mean velocity profiles and streamline patterns under various flow conditions. The development of STARPIC began with the nonswirling TEACH (teaching elliptic axisymmetric characteristics heuristically) computer program (60) as opposed to that of Lilley (44) because the latter contains extensive combustion calculations which are inappropriate under the present objectives.

Besides the incorporation of all swirl momentum effects, numerous special features were included, such as: (1) a generalized "stairstep" simulation of the sloping combustor wall, (2) an advanced nonuniform grid system, (3) momentum wall functions derived from a recent experiment, (4) use of advanced estimates of initial field values, and (5) streamline calculation and plotting.

Discussion of this finite difference computer program is minimized here because it is extensively described in a recent NASA report (11). The report deals with the complete computational problem, showing how the mathematical basis and computational scheme may be translated into an effective computer program. A flow chart, FORTRAN IV listing, notes about various subroutines, and a user's guide are also supplied.

3.1 The Governing Equations

The turbulent Reynolds equations for conservation of mass, momentum (in x, r, and θ directions), turbulence energy k, and turbulence dissipation rate ε which govern the two-dimensional, axisymmetric, swirling, steady flow may be taken as previously (40, 42, 44, 47, 48, 49, 61). The transport equations are all similar and contain terms for convection and diffusion (via turbulent flux terms) of a general dependent variable ϕ. The source term S_ϕ contains terms describing the generation (creation) and consumption (dissipation) of ϕ. Introducing turbulent exchange coefficients and the usual turbulent diffusion-flux (stress ~ rate of strain type) laws, it can be shown that the similarity between the differential equations and their diffusion relations allows them all to be put in the common form:

$$\frac{1}{r}\left[\frac{\partial}{\partial x}(\rho u r\phi) + \frac{\partial}{\partial r}(\rho v r\phi) - \frac{\partial}{\partial x}\left(r\Gamma_\phi \frac{\partial\phi}{\partial x}\right)\right.$$

$$\left. - \frac{\partial}{\partial r}\left(r\Gamma_\phi \frac{\partial\phi}{\partial r}\right)\right] = S_\lambda \tag{3.1}$$

The forms of the source term S_ϕ are given in Table I and other quantities are defined as follows:

$$S^u = \frac{\partial}{\partial x}\left(\mu \frac{\partial u}{\partial x}\right) + \frac{1}{r}\frac{\partial}{\partial r}\left(r\mu \frac{\partial v}{\partial x}\right) \tag{3.2a}$$

$$S^v = \frac{\partial}{\partial x}\left(\mu \frac{\partial u}{\partial r}\right) + \frac{1}{r}\frac{\partial}{\partial r}\left(r\mu \frac{\partial v}{\partial r}\right) \tag{3.2b}$$

$$S^w = 0 \tag{3.2c}$$

$$G = \mu\left[2\left\{\left(\frac{\partial u}{\partial x}\right)^2 + \left(\frac{\partial v}{\partial r}\right)^2 + \left(\frac{v}{r}\right)^2\right\} + \left(\frac{\partial u}{\partial r} + \frac{\partial v}{\partial x}\right)^2\right.$$

$$\left. + \left\{r\frac{\partial}{\partial r}\left(\frac{w}{r}\right)\right\}^2 + \left(\frac{\partial w}{\partial x}\right)^2\right] \tag{3.2d}$$

Implicit here is the use of the two-equation k-ε turbulence model (62, 63) and constant Prandtl-Schmidt numbers from which exchange coefficients are calculated:

$$\mu = C_\mu \rho k^2/\varepsilon + \mu_\ell \tag{3.3}$$

$$\Gamma_\phi = \mu/\sigma_\phi \tag{3.4}$$

The total equation set must be solved for the time-mean pressure p, velocity components u, v, and w, etc. Then other useful designer information, like streamline plots, breakaway and reattachment points, recirculation zones and stagnation points, for example, may be readily deduced.

3.2 The Finite Difference Formulation

Solution may be via the stream function-vorticity, or primitive

pressure-velocity approach. Whereas the former approach, used in the 1968 computer program from Imperial College for example (64), reduces by one the number of equations to be solved and eliminates the troublesome pressure (at the expense of trouble with the vorticity equation), the preferred approach now is SIMPLE (mnemonic for semi-implicit method for pressure linked equations) which focuses attention directly on the latter variables.

Because it possesses many advantages, the present work has been developed using this new technique, which was incorporated in the TEACH program (60).

The finite difference equations are solved on a complex mesh system, shown in Figure 4. The intersections, the point P for example, of the solid lines mark the grid nodes where all variables except the u and v velocity components are stored. The latter are stored at points which are denoted by arrows (and labeled w and s, respectively) located midway between the grid intersections. Details of the special merits of this staggered grid system have been reported previously (60, 65). The different control volumes C, U, and V, which are appropriate for the P, w, and s locations, respectively, are also given in the figure. Thus the u- and v-cell boundaries lie either exactly on or exactly halfway between the grid intersection points P. This improves the accuracy of calculating pressure gradient effects on the u and v velocities (as pressure values now lie directly on appropriate cell faces) and of calculating certain cell boundary fluxes. The flowfield domain boundaries are positioned midway between grid points so that they coincide with normal velocities as in Figure 5, which shows an example of grid specification for the geometry under consideration.

In obtaining the finite difference equations using the primitive approach, it is common to use a hybrid formulation, which is a combination of the central and upwind differencing scheme. It is applied to the representation of the convection and diffusion terms and provides (when needed) the required degree of upstream differencing. In this manner the finite difference equation for a typical variable becomes

$$a_P^{\phi} \phi_P = \Sigma_j a_j^{\phi} \phi_j + S_U^{\phi} \tag{3.5}$$

where

$$a_P^{\phi} = \Sigma_j a_j^{\phi} - S_P^{\phi}$$

Σ_j = sum over N, S, E, and W neighbors

for each variable ϕ at each point P of a grid system covering the flow domain.

3.3 The Solution Procedure

The flowfield is covered with a nonuniform rectangular grid system; typically the boundary of the solution domain falls halfway between its immediate nearby parallel gridlines; and clearly specification of the x and r coordinates of the gridlines, together with information concerned with the position of the boundary, is sufficient to determine the flowfield of interest. The curved or sloping boundaries are simulated by means of a stairstep approach with sloping boundary segments where appropriate.

Finite difference equations like Equation (3.5) hold for all variables at all internal points of the mesh system, except those adjacent to wall boundaries. At these points, the correct boundary influence is

inserted by a linearized source technique, using wall functions so as to avoid detailed calculations in near-wall regions. The effect of swirl on wall function specification is handled as follows. The previous ideas are extended to find total tangential wall shear stress near boundaries (involving x and θ directions for an r = constant wall, and r and θ directions for an x = constant wall). Then appropriate components are deduced directly (for the u and w velocities which are tangential to an r = constant wall, and v and w velocities which are tangential to an x = constant wall). The effects on u, v, and w momentum equations are incorporated via the usual linearized source technique (11).

The finite difference equations and boundary conditions constitute a system of strongly-coupled simultaneous algebraic equations. Though they appear linear they are not, since the coefficients and source terms are themselves functions of some of the variables; and the velocity equations are strongly linked through the pressure. In the solution procedure algebraic equations like Equation (3.5) are solved many times, coefficient and source updating being carried out prior to each occasion. The practice used here is to make use of the well-known tri-diagonal matrix algorithm (TDMA), whereby a set of equations, each with exactly three unknowns in a particular order except the first and last which have exactly two unknowns, may be solved sequentially. In the two-dimensional problem one considers the values at gridpoints along a vertical gridline to be unknown (values at P, N, and S for each point P), and the most recent values at each E and W neighbor are considered known. The TDMA is then applied to this vertical gridline. In this manner one can traverse along all lines in the vertical direction sequentially from left to right of the integration domain, using a certain degree of underrelaxation to enhance convergence.

CHAPTER IV

EXPERIMENTAL FACILITY AND TECHNIQUES

4.1 Wind Tunnel

The Oklahoma State University swirling confined jet test facility is used in the experimental study. A schematic of the overall facility is shown in Figure 3. Ambient air enters the low-speed wind tunnel through an air filter consisting of foam rubber. Then it flows through an axial flow fan whose speed is continuously variable over a wide range in that it is driven by a 5 h.p. varidrive motor manufactured by U.S. Electrical Motors, Inc. Next, the flow gradually expands with the tunnel cross section without separation because numerous fine mesh screens are encountered along the way.

The flow conditioning section is next. It consists of: a perforated aluminum plate (2 mm diameter holes), followed by a fine mesh screen, a 12.7 cm length of packed straws, and five more fine mesh screens. Next is the contoured nozzle leading to the test section. This axisymmetric nozzle was designed by the method of Morel (66) to produce a minimum adverse pressure gradient on the boundary layer to avoid the flow unsteadiness phenomenon associated with local separation regions. The area ratio of the flow conditioner cross section to that of the nozzle throat is approximately 22.5. Further details are available elsewhere regarding the design and construction of the nozzle, flow conditioner, and idealized test model which is described in the next section (67, 68).

4.2 Test Section

The test section consists of a swirl vane assembly and an idealized combustion chamber model which is mounted onto the throat of the wind tunnel nozzle. A photograph of the general arrangement in the laboratory is given in Figure 6. The swirl vane assembly contains ten brass vanes which are individually adjustable for any vane angle ϕ. The diameter of the flow passage within the swirler matches that of the contour nozzle throat which is approximately 15 cm. A solid hub of 4 cm diameter is located at the center of the swirler with a streamlined nose facing upstream, as seen in Figure 7. The downstream end is simply a flat face, simulating the geometric shape of a typical fuel spray nozzle. Figure 8 shows the swirler assembly from the downstream side. A special jig, also seen in the figure, is employed to set each vane at the desired angle.

The idealized combustion chamber model is composed of an expansion block and a long plexiglass tube. The expansion block is a 30 cm diameter disk of oak wood which is mounted to the downstream section of the swirl generator. The block has a 15 cm diameter hole centered on its axis through which the air entering the model flows smoothly. The downstream face of the expansion block has been shaped to provide the desired flow expansion angle α which is shown in Figure 9. There are currently three interchangeable expansion blocks and the appropriate choice gives α = 90, 70, or 45 degrees. Figure 9 shows a view of the swirler with two of the expansion blocks.

The actual combustor of a gas turbine engine, which is illustrated in Figure 1, is idealized in the present study as there are no film cooling holes or dilution air holes, and the simulated chamber wall consists

of a straight pipe. The inside diameter of the pipe is 30 cm and the length is approximately 125 cm. The substantial size of the test model provides excellent probe resolution for five-hole pitot probe measurements, and it also enhances flow visualization. Plexiglass was the chosen material for the test section pipe in order to facilitate flow visualization. It is supported by a wooden cradle which is mounted on a table.

The test section is carefully aligned with the wind tunnel so that the test section and wind tunnel centerlines are colinear. The swirl vane assembly and the expansion block are always securely centered on the wind tunnel centerline, as they are both positioned on the discharge end of the contoured contraction with dowel pins. The test section inlet is centered since it slips snugly over the expansion block which was carefully machined with a lathe. The test section discharge, however, is aligned with a low-power Spectra-Physics Stabilite, model 120, laser beam which passes through its center. A plexiglass disk which fits tightly in the model discharge identifies this center.

A removable length scale exhibiting axial distances downstream is mounted above the test section for flow visualization photography.

4.3 Flow Visualization

Flow visualization experiments using three different techniques were conducted during this investigation and each is described in the following subsections. Such experiments serve as an important investigative tool by immediately providing a clear view of the flowfield. During the initial phase of this study, it was employed: (1) to examine the overall flowfield; (2) to detect unforeseen difficulties with measurements; (3)

to check the gross characteristics of the computer predictions; (4) to locate possible regions of interest in which additional probe measurements might be desired; and (5) to help interpret measured data. The unforeseen difficulties with measurements mentioned above include time-dependent instability effects, regions of severe turbulence, or probe interference.

Probably the most widely used flow tracer to date is smoke. Smoke particles are very small, typically less than 1.0×10^{-3} mm in diameter. Hence they follow air motion quite well; however, they cannot be viewed or photographed individually. Thus one can only create a relatively dense cloud of particles and view the motion of its edges. The cloud will diffuse if the air flow is turbulent, the edges becoming indistinct and then disappearing as the particle concentration drops. An attractive flow visualization technique for both detailed as well as overall characterization in strongly turbulent flows employs neutrally-buoyant helium-filled soap bubbles. Although much larger than particles of smoke, soap bubbles are almost ideal because they trace particle paths and have the average density of air (5).

4.3.1 Neutrally-Buoyant Soap Bubbles

Apparently soap bubbles were first used as flow tracers by H. C. H. Townend, whose work was reported by Lock (69) in 1928. Coal gas was used to make the bubbles neutrally-buoyant for use in a propeller flowfield study. Redon and Vinsonneau (70) injected air and also hydrogen into soap bubbles in a wind tunnel and concluded that air-filled bubbles gave essentially correct trajectories. Some statistical measurements of turbulence using bubbles in a wind tunnel were reported by Kampé de Fériet

(71). Of all the previous work with soap bubbles, that most related to the present study was conducted by Owen (72), who employed them to study the flowfield in a cylindrical vortex tube.

The bubble flow visualization system used in this study is composed of (1) the bubble generator, (2) the light source, and (3) two cameras and tripods. The arrangement of some of these components is schematically illustrated in Figure 10. The bubble generator is model 3, manufactured by Sage Action, Inc. It consists of the injector, shown in Figure 11, in which the bubbles are actually formed, and a console that supplies the constituents to the injector. Only the injector is situated in the tunnel. It is located far enough upstream of the test section to avoid any disturbance to the flow pattern under study. The injector currently employed is 1.6 cm in diameter and approximately 11.5 cm long with a 1 cm diameter stem perpendicular to the main body. Compressed air at a gauge pressure of 4.1 bar is supplied to the injector through this stem, while helium at a gauge pressure of 1.4 bar and bubble film solution are introduced through smaller tubes directly upstream of the stem. The bubble film solution is a special soap mixture, which is commercially available from Sage Action, Inc. After formation, 0.5 to 1.0 mm diameter bubbles are injected into the surrounding freestream and reach the freestream velocity within a short distance. They are then carried by the air stream through the test section. The bubbles are injected at a fairly even rate. It is estimated by Hale et al. (73) from photographs that this bubble production rate is as high as 500 bubbles per second.

The bubble generator console is placed in a convenient location near the tunnel. Three lengths of plastic tubing carry the compressed air, helium, and bubble film solution from the console to the injector. The

console contains micro-metering valves to control the constituent flow-rates, a pressurized cylinder to hold the bubble film solution, and inlet connections for high-pressure air and helium.

An American Optical Co. slide projector, model 1389, served as the light source for illumination of the bubbles. A vertical sheet of light 4 cm thick was produced to illuminate the rx-plane of the bubble flow pattern. This was provided by using a cardboard slide which is opaque except for a thin slit cut out for light passage to the test section.

Tri-X Pan, a very light-sensitive photographic film rated at ASA 400, along with a large camera aperture of f 2.0, were employed in order to obtain photographs of acceptable contrast. Moreover, the film was substantially overdeveloped to compensate for underexposure; this is equivalent to using a severely light-sensitive film rated at approximately ASA 6,000.

A typical procedure begins with adjustment of the flow metering valves for air, helium, and bubble film solution in order to obtain a high generation rate of small bubbles. Then a Polaroid Land Camera, model 180, is used to obtain preliminary photographs since immediate results are obtainable. Once the lighting and camera orientation, camera settings, and glare are resolved the desired production photographs are taken with a 35 mm Minolta single lens reflex camera, model SRT200, with a 45 mm lens.

Each bubble leaves an image of its path, or a streak, on the film and this streak becomes a record of the air movement within this time frame. The record of a number of streaks on a single photograph produces a history of the air motion. The intensity of each streak on the film is not dependent on shutter speed, but rather on the aperture and bubble

velocity, as well as the sensitivity of the film itself. The length of pathlines and (for the slower shutter speeds) the number of pathlines are, however, strongly dependent on shutter speed. A relatively large number of streaks provides an overall picture of the flow pattern. A much smaller number though is useful to see details of the air motion that are evident only by following individual streaks for an appreciable distance. Production photographs were typically taken at shutter speeds ranging from 1/60 to 1/4 second for each flow condition.

4.3.2 Smoke-Wire

Although smoke particles may not be observed individually, small and discrete smoke streaklines can be located within the flowfield so that small scale details may be studied. For example, zero velocity points within a large recirculation zone may be identified.

This is accomplished with the smoke-wire technique, originally developed by Raspet and Moore in the early 1950s. It has been improved and extended since then to generate sheets of very fine streaklines (74, 75, 76). However, much of the present smoke-wire capability results from the development of Nagib and his coworkers (77, 78).

The method consists of a fine wire positioned in the flowfield, coated with oil, and heated by passing an electrical current through the wire. As the wire is coated with the oil, small beads of the oil form on the wire and at each of these beads the smoke filaments originate when the wire is heated. Cornell (79) studied the materials used in generating "smoke" for flow visualization, and explained that particles created with this technique are actually a vapor-condensation aerosol. That is, they are very small liquid particles near 1.0×10^{-3} mm in diameter rather

than products of a combustion process. However, in keeping with the literature, these particles are referred to as smoke.

The apparatus, some of which is shown in Figure 12, consists of a 0.28 mm diameter and 0.6 m long constantan wire, a wooden scaffold support frame, a 4 cc medical syringe, a 0.45 kg weight, and a solid state power supply, model TR36-4M, manufactured by Electronic Research Associates, Inc. The support frame holds the medical syringe oil reservoir on the upper horizontal member, allowing the wire to pass through the syringe needle, the test section, and finally through the lower horizontal member. The frame is easily relocated so that local details at virtually any axial station can be examined.

The wire is kept taut as the weight is attached to its lower end and is free to move as the wire elongates from thermal expansion. The electrical leads of the power supply are connected to each end of the constantan wire, and conduct about 3.5 amps at 25 volts d.c. The same slide projector described for the soap bubble experiment provides the vertical sheet of light to illuminate the rx-plane.

The smoke-wire technique requires air velocities of less than approximately 10 m/s; otherwise the oil droplets are blown off the wire before it is properly coated, and also the smoke diffuses too quickly. Hence the smoke experiments were conducted at lower air flow rates than other experiments.

The procedure begins with applying a slight force on the syringe plunger, which causes several oil drops to run down the wire, coating it with small beads while the wind tunnel is not running. A uniform coating of fine oil beads is necessary, as each bead is a source of a distinct streakline. Several types of oil were tried, although highly refined

kerosene is utilized for all production photographs. Then the wind tunnel motor is turned on. The photographer waits approximately 1 second before manually activating the shutter while the required heat is supplied to the oil. A heavy sheet of streaklines then appears, typically for a duration of about 0.5 second. Only slight experience with this system is required for effective photography. Further details concerning construction of the apparatus and photography of the nonswirling flowfields are found elsewhere (80).

The smoke-wire has primarily been used in considerably less complicated flow situations such as the flow over airfoils and bluff bodies. The present swirling flows exhibit very high levels of turbulent mixing, causing the smoke to diffuse very quickly. Since only very localized results are possible under such flow conditions, this experiment was conducted at several axial stations for each flowfield under investigation.

A large camera aperture of f 2.0 was used for most production photographs. As for soap bubbles, faster shutter speeds such as 1/60 second provide a more detailed observation whereas slower speeds, for example, 1/8 second, give a more time-averaged view. Therefore, shutter speeds for each flow condition typically include at least 1/60, 1/30, 1/15, and 1/8 second. The same film development procedure used for soap bubble photographs is employed here.

4.3.3 Tufts

Perhaps one of the simplest ways of visualizing a flowfield is by inserting a wire grid with a tuft attached at each intersection point of the mesh. These tufts respond to the flow patterns and generally point in the local flow direction. Furthermore, their vascillating motion

indicates the degree of turbulence in steady mean turbulent flow situations. Very large tuft fluctuations, however, can be produced by the combined effects of mean flow unsteadiness and turbulence. Such tuft screens have been employed to visualize the vortex shedding behind swept wings by Bird (81) and Gersten (82). They have also been used by McMahon et al. (83) to observe the interaction of an air jet and a cross wind.

Observations or photographs from a position normal to the tuft screen indicate the flow direction in the plane of the screen. Since the combustor flowfield entails three mean velocity components, a tuft screen was constructed for each of the rx- and rθ-planes. The rx-screen slides into the combustor model with only slight wall clearance, to minimize the flow disturbance.

The overall dimensions of the rx-screen in the radial and axial directions are 29.7 cm and 1.52 m, respectively. Two pieces of extruded aluminum, with 2.5 cm and 0.6 cm as cross-sectional dimensions, are employed as axial frame members, spaced to provide a flow passage radial height of 28.5 cm. Four 1.8 mm diameter steel rods provide radial support and are intermittently positioned axially. Music wire of 0.33 mm diameter traverses the frame with a uniform grid spacing of 1.9 cm radially. A uniform axial spacing of 1.9 cm, 3.2 cm, and 4.4 cm is used for each of three axial sections of length 61 cm, 40 cm, and 46 cm, respectively. The tufts consist of 1.1 mm diameter cotton thread and are 16 mm in length. In construction, the tufts are consistently tied around each wire intersection point and a 3.0 mm diameter rod which was then removed, resulting in an oversized loop around each wire intersection giving enhanced freedom of movement.

The $r\theta$-screen is composed of similar materials, except that its frame is a strip of 24 gauge steel 2.5 cm wide, wrapped into a 29.7 cm diameter ring. It has a uniform grid spacing of 1.9 cm in both directions. The tufts are identical for both screens.

The light source previously described for soap bubble visualization was used as well as the same photographic equipment and technique of over-developing the film. Again, slower shutter speeds indicate the time-averaged motion, and speeds of 1/2, 1/15, and 1/60 second were typically used.

4.4 Mean Velocity Measurements

4.4.1 Instrumentation

Many instruments are used for separately measuring the magnitude and direction of fluid velocity (84). However, there are only a few instruments capable of simultaneously sensing both magnitude and direction. The simplest of these senses pressure at certain locations on the surface of a sphere, hemisphere, or some other shape of probe. Spherical pitot probes using five holes were used by Janes (85) as early as 1915, Meyer and Borren (86) in 1928, and Gutsche (87) in 1931. Pien (88) in 1958, further developed the technique upon realizing the fact that the three pressure measurements on a great circle of a sphere uniquely determine the velocity component in that plane.

The five-hole pressure probe is recommended by Beer and Chigier (13) for mean velocity measurements in turbulent swirling flows and several investigators have successfully used it (23, 89, 90). The probe employed in this study is model DC-125-12-CD from United Sensor and Control Corp.

It is shown schematically in Figure 13 and has a 3.2 mm diameter steel sensing tip and shaft containing five tubes. The sensing head is hook-shaped to allow probe shaft rotation without altering the probe tip location. At the opposite end of the shaft, which is 30.5 cm long, is a manifold for the five tubes.

There are basically three methods of operations. The first and most direct is to adjust the orientation of the probe until both pairs of opposing, direction-sensing pressures are nulled, which means the probe is aligned with the local flow direction. With the second method, the probe is fixed and the flow direction is determined from the calibration relationship between probe pressures and flow direction. The third method is simply a hybrid of the first two, wherein the yaw angle in the horizontal plane is nulled and the pitch angle in the vertical plane is correlated.

The first method is avoided since complicated probe orientation equipment is required. Further, this equipment would probably disturb the flowfield more seriously than the other methods. The second approach is completely unacceptable. This is because the probe cannot properly sense pitch or yaw angles relative to its axis greater than approximately 60 degrees, and the yaw angle often exceeds this limit. This limit is caused by flow separation at the probe tip. Therefore, the third method is exclusively employed in this investigation, as pitch angles are always less than 60 degrees except in a very small fraction of the measurement locations.

The instrumentation system, in addition to the five-hole pitot probe, consists of a manual traverse mechanism, two five-way ball valves, a very sensitive pressure transducer, a power supply, and an integrating volt-

meter. The probe is mounted vertically on the test chamber, as shown in Figure 14, using a manual traverse mechanism, model C1000-18 from United Sensor and Control Corp. This mechanism, shown in Figure 15, is made entirely of steel with a linear vernier accurately readable within ±0.25 mm. This allows the probe to vertically traverse across the chamber radius with the capability of manually rotating the probe about its shaft axis to null the yaw angle felt by the pressure sensing tip. This yaw angle is read from the rotary vernier of the traverse unit which is accurately readable within ±0.2 degree.

The differential pressure transducer is model 590D from Datametrics, Inc. It has a differential pressure range from 0 to 1.3×10^3 N/m^2. The sensing element is a high precision stable capacitive potentiometer in which the variable element is a thin, highly prestressed metal diaphragm. Power for the transducer is provided by a model 721A Hewlett Packard power supply.

The pressure transducer output is read as the d.c. signal from the TSI model 1076 integrating voltmeter. Use of an integrating voltmeter removes pressure fluctuations from the vibrating tygon tubing connecting the probe to the valves and transducer. The five-way ball valves are model SS-43ZF2 by Whitey Valve Co. These valves along with the pressure transducer are mounted on a small portable platform, shown in Figure 14, in order to minimize the length of tygon tubing for improved dynamic response of the measurement system. Thus the traverse unit and platform are moved together to each successive axial station.

Finally, auxiliary equipment is used, including model 631-B strobotac from General Radio, Inc., to measure fan speed. Also, a barometer/

thermometer unit from Cenco Corp. is used for local pressure and temperature readings.

4.4.2 Measurement Technique

The basic measurement technique entails aerodynamically nulling the yaw in the horizontal plane by rotation of the probe about its vertical shaft and then reading two differential pressures ($p_N - p_S$ and $p_C - p_W$). These pressures along with the yaw angle β are used in data reduction to obtain pitch angle δ in the vertical plane and the three mean velocity components. The data reduction employs two calibration curves which were obtained for a single calibration velocity. The underlying principle is that the calibration is independent of probe Reynolds number Re_p, which is based on probe tip diameter.

Careful calibration experiments reveal that this condition exists for $Re_p \geq 1090$, or a local velocity of 5.4 m/s. Hence measurements of such low velocities suffer from a necessary calibration error. However, this error affects the velocity measurements typically by less than 6 percent for $Re_p \geq 400$, corresponding to a local velocity greater than 2.0 m/s.

Prior to production measurements, the five-hole pitot rotary vernier must be zeroed for yaw so that the x and θ axes of the measurement coordinate frame coincide with those of the test section, which are illustrated in Figure 14. This is accomplished by rotating the probe until the yaw is aerodynamically nulled near the center of the test section inlet for nonswirling flow. The radial axes of the probe and the test section coincide since the traverse unit base has been carefully machined to mount vertically on the plexiglass tube.

Each traverse begins at the centerline, and this location is verified if the probe casts its shadow in the center of a laser beam which passes upstream along the center of the test section. If necessary, the traverse mechanism is carefully shimmed until the above condition is obtained.

After the pressure transducer is zeroed, the measurement procedure for each location within a traverse begins with rotation of the probe until the yaw is aerodynamically nulled. This is indicated by a zero reading for $p_W - p_E$, where the pressures are identified in Figure 13. The resulting probe rotation angle ψ is read from the rotary vernier. Then the five-way switching valves are set so that $p_N - p_S$ is sensed by the transducer. Finally, the reading of $p_C - p_W$ is similarly obtained.

Mass flow rate entering the test section must be determined for the calculation of inlet Reynolds number Re_d and spatial mean inlet velocity. This quantity is obtained for each flowfield from a measurement of dynamic pressure with a conventional pitot-static probe. The probe tip is located on the centerline and slightly upstream of the contour nozzle exit. It has been experimentally verified with a radial traverse of the nozzle discharge that, in this facility, the centerline exit velocity is extremely close to the spatial mean velocity. This results from the fact that the boundary layer momentum deficit is counterbalanced by a slightly higher-than-average momentum value just outside the boundary layer. Thus the nozzle exit spatial mean velocity for each flowfield is obtained from a single pitot-static reading. Finally, a continuity correction for the slight flow area difference between the measurement and exit stations provides the necessary value.

The ambient pressure and temperature were monitored near the facility

for the determination of density. Also, the wind tunnel fan speed was frequently checked with the strobotac.

An initial experiment was performed to investigate the asymptotic invariance of Re_d on the flowfield. This is needed to ensure that the dimensionless measurements will be applicable to actual combustor hardware, which often operates at considerably higher Re_d values than those desired for the present test facility. Measurement traverses were performed at selected axial stations at increased values of Re_d for each flowfield. Adjustment of the varidrive fan motor provides excellent and stable control of Re_d. The resulting velocity profiles are discussed in Chapter VI.

4.4.3 Data Reduction

The differential pressure readings from the five-hole pitot probe are utilized directly to obtain the square of the vector velocity. In turbulent flow conditions, the time-mean pressures give rise to the time-mean average of the square of the vector velocity $\overline{V^2}$. Since

$$\overline{V^2} = \overline{V}^2 + \overline{V'^2} \tag{4.1}$$

where V' is the fluctuating portion of the velocity magnitude and the overbars denote time-averaging, it is slightly incorrect to infer that $\overline{V^2}$ is equal to the square of the magnitude of the time-mean velocity vector $\overline{V}^2$. However, the fluctuation term $\overline{V'^2}$ is not known and very little information is available for the effect of turbulence in swirl flows on pressure probes, which is probably considerable for turbulence intensities greater than about 20 percent (12). Furthermore, the procedures for making corrections for turbulence levels are long and tedious, and even

then the confidence in their applicability is unknown. Therefore, no attempt is presently made to incorporate such corrections, and the deduced velocity is taken to be the time-mean velocity magnitude $\overline{V}$ which is written without the overbar from here onward.

The data at each measurement location are reduced with the FORTRAN computer program listed in Appendix C by first calculating the pitch coefficient $(p_N - p_S)/(p_C - p_W)$. From this value a cubic spline interpolation technique is used to obtain the pitch angle δ in the vertical plane from the calibration characteristic presented in Figure 16. The resulting value of δ is similarly utilized to determine the velocity coefficient $\rho V^2/[2(p_C - p_W)]$ from the calibration characteristic given in Figure 17.

Values for V as well as the axial, radial, and swirl velocity components u, v, and w, shown in Figure 18, are easily calculated from the velocity coefficient, pitch angle, and yaw angle β, which is in the horizontal plane. The latter angle is given by

$$\beta = 360° - \psi \tag{4.2}$$

where ψ is the probe rotation angle read on the rotary vernier of the traverse mechanism. The magnitude of the velocity vector is given by

$$V = \frac{2}{\rho}\left[\frac{V^2}{2(p_C - p_W)}(p_C - p_W)\right]^{1/2} \tag{4.3}$$

and the velocity components are obtained from

$$u = V \cos\delta \cos\beta \tag{4.4a}$$

$$v = V \sin\delta \tag{4.4b}$$

and

$$w = V \cos\delta \sin\beta \tag{4.4c}$$

Further calculations include that for mass flow rate and axial flux of angular momentum, which are respectively expressed as

$$\dot{m} = 2\pi \int_0^R \rho\, ur\, dr \tag{4.5}$$

and

$$G_\theta = \int_0^R \rho\, uw\, r^2\, dr \tag{4.6}$$

These are evaluated from the velocity measurements with the data reduction computer program.

4.4.4 Calibration

Proper calibration of the five-hole pressure probe is extremely critical to the accuracy of the experimental work. Consequently, considerable care was exercised in the construction and use of the calibration equipment. The calibration equipment consists of a small air jet, a rotary table, a probe mounting bracket, and the instrumentation system previously described. The calibration jet supply line consists of a compressed air line, which delivers the desired flow rate through a small pressure regulator and a Fischer and Porter model 10A1735A rotameter. The jet housing consists of an effective flow management section followed by a contoured nozzle with a 3.5 cm diameter throat.

The rotary table is model BH-9 from Troyke Manufacturing Co. Its rotary vernier is readable within ±0.5 minute. As shown in Figure 19, the aluminum probe mounting bracket is secured to the rotary table, and it supports the probe which rests in a cylindrical steel collet.

The motion of the rotary table orients the probe at the desired pitch angle, whereas the yaw is aerodynamically nulled. The probe sensing tip remains at the centerline within the potential core of the jet and less than one throat diameter downstream of the nozzle discharge plane. The pitch angle is zeroed by very carefully aligning the probe shaft in a plane parallel to that of the nozzle throat.

The calibration procedure consists of recording the voltage output from the pressure transducer for differential pressures $p_N - p_S$ and $p_C - p_W$, where these pressures are identified in Figure 13. These data are obtained at 5 degree increments in δ over the range $-55° \leq \delta \leq 55°$. The measurement technique requires the entire calibration to be conducted at a constant jet velocity. This is permitted since the dimensionless calibration coefficients are independent of Re_p for $Re_p \geq 1090$ (5.4 m/s) determined by careful calibration experiments. Measurements of much lower velocities suffer from a calibration error. However, this is rarely over 6 percent for $Re_p \geq 400$ (2.0 m/s).

Figures 16 and 17 show the calibration characteristics from which δ and velocity coefficient $\rho V^2/[2(p_C - p_W)]$ are obtained, respectively. Both curves exhibit considerable symmetry, as the five pressure sensing holes are almost symmetrical about the probe tip axis.

CHAPTER V

GROSS FLOWFIELD CHARACTERIZATION

Recirculation zones are important to combustor designers because most of the burning occurs in these regions and they exhibit the highest temperatures (47). The size and location of these regions is determined by flow visualization experiments and predicted by numerical computations. The predicted time-mean streamline patterns are compared with corresponding artistic impressions deduced from flow visualization photographs of tufts, smoke, and bubbles responding to the experimental flowfield patterns. Selected photographs of the visualization experiments are also presented and discussed in the subsequent sections.

5.1 Artistic Impressions of Streamline Patterns From Flow Visualization

Photographs of each of the six flowfields resulting from ϕ = 0, 45, and 70 degrees with α = 90 and 45 degrees have been examined in detail for each of the three flow visualization methods currently employed. The characteristics of the overall flowfield are illustrated and discussed via the resulting time-mean dividing streamline patterns. These are sketched in Figures 20 and 21 from information obtained from the entire collection of flow visualization photographs. Results from the smoke-wire experiment are utilized near the inlet, whereas tuft and bubble data are used in approximating the size and shape of the recirculation zones downstream.

Bubble flow patterns also reveal the existence of a precessing vortex core, which occurs downstream of the central region.

The resulting streamlines for the three cases of the sudden expansion α = 90 degree geometry are shown in Figure 20. The nonswirling flow sketch in part (a) exhibits a large corner recirculation zone which is in excellent agreement with the corresponding streamlines from the measurements of Chaturvedi (15). Appropriate prior measurements for the present swirling flows have not been found. For the moderate swirl vane angle case of ϕ = 45 degrees a central recirculation region appears in conjunction with a decrease in size of the corner zone. A thin precessing vortex core, discussed by Syred and Beer (91), is observed near the centerline extending from the end of the central region to the test section exit. The axial location of the upstream varies, ranging approximately from x/D = 1.25 to 1.75. This vortex core is essentially a three-dimensional time-dependent instability which occurs as a swirling region of negligible axial velocity whose center winds around the test section centerline. A further increase in vane angle to ϕ = 70 degrees results in continued enlargement of the central zone; however, the corner bubble is essentially unaffected. For this flowfield the vortex core is expanded in the radial as well the axial direction, as its upstream edge fluctuates from approximately x/D = 1.0 to 1.5.

The corresponding sequence of dividing streamlines is found in Figure 21 for the gradual flow expansion case with α = 45 degrees. As with Figure 20, the nonswirling flowfield exhibits excellent agreement with corresponding measurement of Chaturvedi. No evidence of a corner zone is found from examination of the photographs for the intermediate vane angle case, although the flow pattern is otherwise very similar to the corresponding

flow for $\alpha = 90$ degrees. The flowfield with $\phi = 70$ degrees produces exactly the same effects as in the abrupt expansion case of Figure 20.

5.2 Flow Visualization Results

5.2.1 Tufts

Tuft visualization is very important in that it supplies an overall view of zones very clearly. As discussed in section 4.3.3, photographs at various shutter speeds were obtained. Slower speeds show more of the temporal behavior, although the tufts are sometimes not distinctly visible in portions of the flowfield. Some of the more noteworthy photographs are presented here, encompassing a range of shutter speeds. Velocities in recirculation zones are often somewhat lower than in other portions of the flowfield, and thus under such conditions there may be insufficient drag on a tuft to align it accurately with the local flow direction. However, this is taken into consideration in interpreting the photographed results.

The three sudden expansion flowfields are characterized in Figure 22 as photographs of the rx-screen tufts. Figure 22(a) identifies the corner zone reattachment point for the nonswirling flowfield. It is found from the length scale as $x/D = 2.1$, wherein tufts showing no air motion are considered stagnation points. Further, an indication of the turbulence level is depicted as the rather slow shutter speed of 1/15 second was used.

For swirl vane angle $\phi = 45$ degrees, Figure 22(b) is a photograph taken at 1/125 second. The swirl is in the counterclockwise direction when viewed from downstream. Both the corner and central recirculation regions are clearly visible, and their downstream stagnation points appear to be at $x/D = 0.4$ and $x/D = 1.6$, respectively. The large vane angle case

is photographed in Figure 22(c), again at 1/125 second shutter speed. Although the upper corner is not well illuminated in this photograph, the lower corner region is seen to extend to $x/D = 0.4$ and the central zone to $x/D = 1.75$.

Photographs of the flowfields with $\alpha = 45$ degrees are shown in Figure 23. The nonswirling case in Figure 23(a) is almost identical to Figure 22(a), with a corner zone length of $x/D = 2.0$. For $\phi = 45$ degrees, Figure 23(b) shows no evidence of a corner zone using 1/125 second shutter speed and the central region apparently extends to $x/D = 1.5$. Finally, the $\phi = 70$ degree case exhibits a central region extending downstream as far as $x/D = 1.85$ for 1/15 second shutter speed.

Figures 24 and 25 are photographs of the $r\theta$-screen of tufts for $\alpha = 90$ and $\phi = 45$ degree flow conditions at $x/D = 0.5$, 1.0, 1.5, and 2.5. The shutter speed is 1/2 second in order to capture information regarding turbulence levels as well as flow direction. The camera is positioned slightly downstream and on the centerline of the test facility, and hence an annular ring of distorted tufts appears around the tuft screen because of the reflectivity of the plexiglass tube. The variation in brightness of the tufts is merely caused by the angle at which the light strikes each particular tuft.

Figure 24(a) apparently shows noticeable but random asymmetry in turbulence levels at $x/D = 0.5$, whereas Figures 24(b) and 25(a) seem to reveal a horizontal strip of highly fluctuating tufts. However, it may be unrealistic to conclude from this that such a region of intense turbulence exists because the effect of gravity acting on tufts pointing vertically upward or downward is different from that on horizontal tufts. Figure 25(b) shows that at $x/D = 2.5$, large direction fluctuations occur only

near the centerline. This probably results from the tendency of the center of the precessing vortex core to randomly oscillate about the test section centerline (91).

5.2.2 Smoke-Wire

Local details in the nonswirling flowfields are clearly revealed through the visualization of streaklines indicated from the generation of illuminated smoke, as discussed in section 4.3.2. In the swirling flows strong mixing diffuses the smoke so that streaklines are not distinguishable. However, under such conditions recirculation zone outlines are visible, especially in the region near the smoke-generation wire. A selected photograph is exhibited and discussed for each of the six flowfields considered in previous sections.

The corner recirculation bubble in the nonswirling case with wall expansion angle α = 90 degrees is revealed in Figure 26(a) using 1/15 second shutter speed. Also, the radial location of the zero velocity point within the upper and lower corner bubble is estimated to be approximately 0.15 D from the respective walls of the test facility. This agrees with the velocity measurements presented in Chapter VI.

The moderate swirl vane angle flow with a 1/30 second exposure is shown in Figure 26(b). The shortened corner zone is easily identified because the adjacent downstream flow contains no smoke near the inlet. This bubble is seen to extend to approximately x/D = 0.45. The tufts in Figure 22 indicate a slightly shorter zone ending at approximately x/D = 0.4. The upstream portion of the central zone is also clearly seen, as low velocity fluid carries a dense mass of smoke which slowly moves upstream of the inlet. Further, the precessing vortex core is seen to

contain no smoke. Since it exhibits negligible axial velocity, the smoke is essentially carried around it by the high velocity fluid outside the core.

Figure 26(c) is a photograph at 1/8 second of the ϕ = 70 degree case wherein this core is not as distinct. In this case some smoke has diffused into the core due to a slightly longer delay before activating the camera shutter. Observe that both the corner and central zones near the inlet reveal that the only change from those for ϕ = 45 degrees is a slightly wider central region.

The same swirl sequence for the gradual expansion geometry with α = 45 degrees is presented in Figure 27. The nonswirling case at 1/15 second reveals about the same details as the corresponding case in Figure 26. The ϕ = 45 degree flowfield at 1/60 second exhibits no evidence of a corner bubble and a thinner central bubble at the wire position of x/D = 0.25. The existence and location of the vortex core is very similar to that in Figure 26(b). The large vane angle case shown in Figure 27(c) using 1/15 second reveals no evidence of a corner zone. Also, the central zone at x/D = 0.25 appears considerably wider than that for ϕ = 45 degrees shown in Figure 27(b).

5.2.3 Neutrally-Buoyant Soap Bubbles

Soap bubbles injected into the air flow upstream of the test section trace pathlines clearly when illuminated. This technique is discussed in detail in section 4.3.1. Photographs of illuminated bubbles are taken with various shutter speeds and camera positions. In relatively lower turbulence intensity portions of the flowfield mean flow directions can be obtained by ensemble averaging local tangents to pathlines traced out

by soap bubbles. This helps define the flowfield geometry in terms of the outline of recirculation regions.

A sample flow visualization photograph is presented in Figure 28(a) corresponding to the zero swirl, 90 degree expansion angle flowfield. The photograph, taken with a relatively long time exposure (1/8 second), clearly shows a great number of individual pathlines. Photographs of this type can be used to indicate regions of highly turbulent flow such as that near the centerline of the flowfield which exhibits smoother, straighter pathlines. In addition, the outline of the corner recirculation region can be estimated from Figure 28(a) (and numerous additional photographs taken at the identical run condition). For this geometry the mean stagnation point defining the end of the recirculation zone appears to be at $x/D = 2.0$.

A photograph with $\phi = 45$ degrees and 1/8 second shutter speed is shown in Figure 28(b), where the precessing vortex core is clearly seen extending from $x/D = 1.5$ to the exit. Its upstream edge fluctuates randomly from approximately $x/D = 1.25$ to 1.75. The corner bubble is observed in both the upper and lower portions of the flowfield, extending to approximately $x/D = 0.4$, which agrees almost exactly with the smoke flow pattern for this flowfield in Figure 26(b). A photograph using 1/15 second shutter speed is presented in Figure 28(c) for the $\phi = 70$ degree flowfield where a thicker vortex core is obvious. Also, it extends farther upstream to $x/D = 1.25$ in this photograph, although this fluctuates from about $x/D = 1.0$ to 1.5. The corner zone is faintly visible here, and its axial length seems to extend to about $x/D = 0.4$.

Figure 29(a) is a 1/15 second exposure of the nonswirling case with $\alpha = 45$ degrees. Essentially the same result is found as in the

corresponding α = 90 degree flowfield in Figure 28(a). The intermediate vane angle case is visualized using 1/4 second shutter speed in Figure 29(b). As with the smoke flow pattern in Figure 27(b), there is apparently no evidence of a corner bubble. Otherwise, there is little difference between Figures 29(b) and 28(b). The ϕ = 70 degree flow shown in Figure 29(c) is photographed at 1/8 second, and agrees with the smoke pattern in Figure 27(c) that there is no apparent corner zone. Further, the vortex core extends upstream to x/D = 1.25, as in the corresponding swirl case in Figure 28(c).

5.3 Predicted Streamline Patterns

The inlet boundary condition for the flowfield prediction program consists of a flat velocity profile as in plug flow for both u and w, whereas v = 0. This approximation has often been employed when pertinent measurements are not available (46, 47). It was discovered near the end of this investigation from the five-hole pitot velocity measurements for the swirling flowfields, that in the test facility, the inlet velocity profiles are actually much different in shape and magnitude from those assumed for the general predictions. These measurements are presented and further discussed in Chapter VI. This difference results from: (a) imperfect blade efficiency, (b) the existence of a hub, and (c) the fact that the downstream edge of the swirl vanes of the test facility is actually located approximately 4 cm upstream of the flow expansion corner, where x/D = 0. This swirler location allows the central recirculation zone to begin upstream of x/D = 0, thereby changing the velocity profiles there. Hence swirling flow streamline predictions in Figures 30 and 31, parts (b) and

(c), are not expected to exhibit excellent agreement with experiments, particularly near x/D = 0.

Figures 30 and 31 are calculated and plotted by computer to show time-mean streamline patterns for α = 90 and 45 degrees, respectively. Although the solution of the swirling flows is not entirely realistic, the trends are generally correct. The nonswirl predictions do not suffer from the inlet boundary condition error described above. The results shown in Figure 30(a) exhibit excellent agreement with the flow visualization results in Figure 20(a) and also with the streamline pattern resulting from corresponding measurements of Chaturvedi (15). The intermediate case of ϕ = 45 degree vanes shows reasonable agreement with the results in Figure 20(b) except at x/D = 0. Discrepancies include central recirculation zone lengths of 1.35 D and 1.6 D for predictions and visualization, respectively. The corner recirculation region lengths, however, are in exact agreement. Surprisingly, for ϕ = 70 degrees the predicted and photographed central zone lengths are x/D = 3.0 and 1.75, respectively. Further, no corner zone is predicted, whereas the photographs reveal one with axial length x/D = 0.4.

As with the α = 90 degree case, the nonswirling flowfield with α = 45 degrees, shown in Figure 31(a), is very well predicted by comparison with Chaturvedi's measurements and the present photographs. No corner zone is predicted in this geometry for either the intermediate or large vane angle flows, which agrees with visualization results of Figure 21(b) and 21(c). For ϕ = 45 degrees, the predicted central zone length is x/D = 1.35 whereas that photographed is approximately 1.5. The central region length for the strongly swirling flow from computations and visualization

is x/D = 1.75 and 1.85, respectively. Hence the central zone is more accurately predicted for α = 45 degrees than for α = 90 degrees.

5.4 Parametric Effects

Streamline plots, including those deduced from flow visualization as well as those predicted, allow recirculation zones to be characterized parametrically. The parametric effects are illustrated in Figures 32 and 33 for predictions and visualization, respectively. Figure 32 shows the predicted effects of α and ϕ on the corner and central recirculation zone lengths. Several observations should be noted. First, zone lengths are only slightly affected by α, as found previously for the corner bubble under isothermal nonswirling conditions (15, 31). Further, at these high Reynolds numbers, the corner region length is independent of Reynolds number (33, 34). As α decreases from 90 to 45 degrees, the zone lengths tend to decrease slightly and the inlet flow is encouraged to impinge on the confining walls. Second, the corner bubble length decreases upon increasing ϕ from 0 to 45 degrees, and also the central region and the precessing vortex core appear. Increasing the vane angle to 70 degrees slightly enlarges the central zone and the vortex core.

Visualization results exhibit close agreement with predictions for the shape of both corner and central regions for ϕ = 0 and ϕ = 45 degrees. Further, this also occurs for ϕ = 70 degrees with the gradual expansion geometry where α = 45 degrees. However, for the abrupt expansion case where α = 90 and ϕ = 70 degrees, the visualized corner zone is not predicted. Moreover, the central region length is seriously overpredicted at x/D = 3.0 as compared with 1.75. A lack of prediction accuracy for swirling

flows is expected because of complicated inlet conditions and/or the lack of realism in the turbulence model; however, it is surprising that the α = 45 degree case exhibits close agreement while that for α = 90 degrees does not.

CHAPTER VI

VELOCITY MEASUREMENTS, PREDICTIONS, AND COMPARISON WITH EXPERIMENT

Each of the six flowfields under investigation is first characterized in terms of axial and swirl time-mean velocity measurements obtained using a five-hole pitot probe. Then general velocity predictions using estimated inlet conditions are presented. A special test case is described also which serves as a validity check of the computer code for the abrupt expansion angle α = 90 degrees using measured inlet conditions. Next, reliability of predictions and measurements is discussed, and finally, the results of another validity test for a non-expanding geometry is described.

6.1 Five-Hole Pitot Probe Velocity Measurements

Details of the five-hole pitot measurement apparatus and technique are discussed in section 4.4. Readings were taken at approximately 20 positions across the test facility radius at the various axial stations for which velocities are presented. Before production measurements began, readings were taken for ϕ = 0, 45, and 70 degrees at various values of inlet Reynolds number. Comparison of these data determined the Reynolds number required to ensure that the nondimensionalized measurements are independent of Reynolds number. A sample of these data is presented and discussed in section 6.4.2.

Figures 34, 35, and 36 show the axial and swirl velocity profiles for ϕ = 0, 45, and 70 degrees with α = 90 degrees. Note that the scale of dimensionless u/u_o shown at the inlet in Figures 34(a) and 35(a) is different from that of w/u_o which is found in Figure 35(b). These scales apply to all figures through section 6.3. Radial velocities are consistently much smaller than the axial and swirl components, and they are indicated in the dividing streamline patterns deduced from flow visualization experiments depicted in Figures 20 and 21. Therefore, they are not presented here. Figure 34 shows the corner recirculation region for the nonswirling flow on the verge of reattachment at x/D = 1.5 and also at 2.0, whereas it occurs at x/D = 2.1 for the corresponding visualization results shown in Figure 20(a). The corresponding measurements of Chaturvedi (15) yielded a value of x/D = 2.3.

Both of the inlet profiles in Figures 35 and 36 differ in magnitude and shape from the flat profiles used as inlet boundary conditions for the general predictions. This is discussed in section 5.3 where it is mentioned that the swirl vanes in the facility are not 100 percent efficient. It can be seen in Figure 35 that a 45 degree swirl vane angle produces a maximum swirl flow angle $[\tan^{-1}(w/u)]$ of 30 degrees at the test chamber inlet. The maximum swirl flow angle for the 70 degree vane angle case shown in Figure 36 is only 34 degrees. Thus there is only a slight increase of swirl flow angle, although these two flows are different in that the inlet profiles are considerably more sharply peaked for the ϕ = 70 degree case. Figures 35 and 36 show zero u and w velocity near the axis at the inlet, but actually the probe was insensitive to the very low velocities there. This is consistent with the flow

visualization result discussed in Chapter V that the central bubble extends upstream of the inlet.

The measurements shown in Figure 35(a) provide no evidence regarding the existence of a corner zone. This is expected because flow visualization reveals that the region only extends to x/D = 0.4. However, there is clear evidence of a rather large central zone whose length is similar to that shown in Figure 20(b). Although the axial velocity profiles are beginning to flatten in the downstream direction, they retain a zero velocity value on the axis, which is consistent with soap bubble flow patterns as seen in Figure 20(b). The early erratic behavior shown by the swirl velocity profile in Figure 35(b) quickly transforms, exhibiting a solid-body-rotation core with a rather flat profile outside this region.

Figure 36 also reveals the discrepancy regarding inlet velocity profiles. The large central recirculation region causes the downstream flow to be accelerated near the top wall. The early erratic behavior found in the swirl velocity profile at x/D = 0.5 quickly develops into a shape similar to that seen in Figure 35(b). The precessing vortex core motion discussed in Chapter V results in poor measurement repeatability which promotes the irregular behavior within this core region.

Figures 37, 38, and 39 exhibit velocities for the same sequence of flowfields with α = 45 degrees. The inlet profiles were not measured in this geometry because the presence of the expansion block interferes. Effects of ϕ on velocities, similar to those found for the sudden expansion cases, are found in the flowfield sequence for this test section geometry. The major difference is that the sloping wall encourages the

inlet flow to accelerate near the top wall. Also, it tends to shorten or obliterate the corner recirculation region.

6.2 General Velocity Predictions

All results are obtained via a nonuniform grid system due to the resulting enhancement of solution accuracy. Nineteen cells are employed in the r-direction, and they are clustered near the shear layer region and along the wall and centerline. The cells are gradually expanding in the streamwise direction, and from 21 to 33 are employed as required to produce the desired α. The inlet profiles of axial velocity u and swirl velocity w are idealized as "flat" (i.e., constant-valued) with 100 percent efficient swirl vanes. Also, it is assumed that $v = 0$. The exit is always located well downstream of the central zone where the flow is considered parallel with zero radial velocity. Further details are briefly discussed in Chapter III. For comparison with other results, it should be noted that ϕ and swirl number S are related by $S = 2/3 \tan \phi$, so that vane angles 45, 60, and 70 degrees, for example, correspond to S values of 0.67, 1.15, and 1.83, respectively (12).

Predicted time-mean axial and swirl velocity profiles for the sidewall expansion angle $\alpha = 90$ degrees are shown in Figures 40, 41, and 42 for swirl vane angle $\phi = 0$, 45, and 70 degrees, respectively. The nonswirling case in Figure 40 exhibits close agreement with measurements of Chaturvedi (15) as shown elsewhere (5). Note the scale of nondimensional u/u_o shown at the inlet profile; this applies to all subsequent general predictions. Further, the centerline velocity exhibits little change in the streamwise direction.

Figure 41(a) reveals that with $\phi = 45$ degrees, the mean axial velocity profiles are dramatically changed. A maximum velocity value occurs in an annular fashion near $r/D = 0.35$, although a more flattened shape quickly develops before $x/D = 1.0$. It should also be noted that the boundary layer on the outer sidewall is relatively thin and is not easily seen on the figures using the chosen scale. Note that the scale for w/u_o shown at the inlet in Figure 41(b) is different from that of u/u_o. Both of these scales are used in all subsequent figures through section 6.3. All of the swirl velocity profiles exhibit solid-body-rotation behavior near the centerline, even near the inlet where a flat profile is a specified inlet condition. The radial location of the station maximum for w tends to increase with x/D in Figure 41(b). Swirl as well as axial velocity profiles appear to approach those corresponding to swirling flow in a pipe as x increases.

Figure 42(a) reveals that the strong swirl case provides a much larger central recirculation region at $x/D = 0.5$, which is caused by strong centrifugal effects. This promotes a very large foward velocity near the wall and almost eliminates the corner region, although experiments show it is unaffected. The radial extent of the central recirculation zone and the velocity near the wall quickly diminish downstream as swirl strength is dissipated. The swirl velocity profile in Figure 42(b) are similar to those of Figure 41(b), except much stronger magnitudes result from the increased vane angle.

The same sequence for the $\alpha = 45$ degree geometry is found in Figures 43, 44, and 45. The inlet profiles are not shown here since they are the same as those of the corresponding cases in Figures 40, 41, and 42. The nonswirling flowfield shown in Figure 43 is essentially identical to the

nonswirling case with α = 90 degrees. For ϕ = 45 degrees, Figure 44 shows little effect of α upon comparison with Figure 41. The central region indicated in Figure 44(a) is slightly thinner at x/D = 0.5. The strong swirl flowfield illustrated in Figure 45(a) exhibits a smaller backflow region than for α = 90 degrees in Figure 42(a), although it displays larger upstream velocities. Also, the peak in the profile at x/D = 0.5 occurs in an annular fashion, whereas this is not seen in Figure 42(a). Swirl velocities in Figure 45(b) exhibit a slightly larger magnitude near the top wall than that in Figure 42(b), but are otherwise very similar.

6.3 The Specific Test Case

Due to the discrepancy regarding axial and swirl inlet velocity profiles, the importance of which was discovered near the end of this investigation, another prediction of the α = 90 and ϕ = 45 degree flowfield is presented. The measured velocities are specified as the inlet boundary condition, and the results are seen in Figure 46 along with the measurements.

This prediction shows that the large peak of inlet axial velocity for x/D = 0.5 is located at r/D = 0.25 rather than 0.40 as measured. Also, a much smaller central zone is predicted than for the general predictions. However, no effect of this discrepancy is seen beyond x/D = 1.5. The measured inlet swirl velocity peak broadens very quickly by x/D = 0.5. Also, a solid-body-rotation core is exhibited there, which is somewhat similar to the previous predictions shown in Figure 41. Comparison with measurements shows considerably larger velocity magnitudes at x/D = 0.5, but lower values downstream.

This discrepancy near the inlet might result from backflow at the inlet boundary which could not be measured because of transient effects or the lack of probe sensitivity for small velocities.

6.4 Reliability of Predictions and Measurements

6.4.1 Predictions

The finite difference mesh size employed for the flowfield predictions resulted from a compromise between the irreconcilable alternatives of computing cost and flowfield resolution. Several grid systems were utilized to determine the effect of grid density on the solution of the present flowfields. The chosen grid is discussed in Chapter III and an example is shown in Figure 5. An increase of 60 percent in the number of computational cells produces a change of only 0.3 and 1.1 percent for top wall and centerline dimensionless axial velocities, respectively.

Another important aspect of solution accuracy concerns the convergence criterion. Rather than use the well established fractional change criterion, which is a necessary but not sufficient condition for convergence, a residual source criterion is employed. This residual is defined by equations like

$$R_P^{\phi} = a_P^{\phi}\phi_P - \sum_j a_j^{\phi}\phi_j - S_U^{\phi} \tag{6.1}$$

which has been obtained from Equation (3.1) and which measures the departure from exactness (except for the use of current coefficients and source) for the variable ϕ at the point P. When each of these quantities becomes smaller than a certain fraction of a reference value, the finite difference equations are considered to be solved.

Although inaccuracies resulting from mesh resolution and degree of convergence are insignificant, the predictions suffer from inherent inadequacies in the turbulence model. This is tolerated presently because these models for complicated swirling flows are not yet available (49). The k-ε model developed for nonswirling flows has been extended to include swirl shear stresses; however, an isotropic viscosity remains while swirling flows in combustor geometries can exhibit anisotropic behavior (26). However, the test case consisting of the measurements of Vu and Gouldin (29) exhibits very encouraging results as discussed in section 6.5.

6.4.2 Measurements

It is difficult to estimate the accuracy of the flow visualization results. The soap bubbles probably trace the flow very accurately because they are neutrally-buoyant and approximately only 0.5 to 1.0 mm in diameter. The tufts observed in the rx-plane of the test section do not respond well to the local flow direction in a low velocity region due to the small drag forces acting on them. They are considered very reliable in higher velocity regions, however. The smoke particles have much greater density than air and consequently they are affected by gravity in low velocity areas and by centrifugal forces in strongly swirling regions.

Little information is available concerning the effect of turbulence on pressure probes in swirling flows (12). However, it is presumed that the five-hole pitot probe is accurate within approximately 5 percent for most of the measurements. This value may increase to 10 percent as the velocity magnitude falls below approximately 2.0 m/s because the probe

is not very sensitive to such low dynamic pressures. In addition, the calibration is no longer independent of probe Reynolds number. The pressure transducer is estimated to have a measurement uncertainty of approximately 0.25 percent for a typical velocity magnitude of 5 m/s and 0.75 percent at 2 m/s.

An experiment to determine the extent to which the five-hole probe disturbs the flow was conducted. A dummy probe of approximately the same size and shape was inserted through the lower wall of the test section, exactly opposite to the five-hole probe entering through the upper wall. Axial and swirl velocity profiles with and without the dummy probe, which is traversed exactly like the measuring probe, are shown in Figures 47 and 48 for $x/D = 1.0$ and 2.5, respectively, with $\alpha = 90$ and $\phi = 45$ degrees. Clearly the presence of the dummy probe has virtually no effect. Further, since the dummy probe has a negligible influence, these figures show evidence of good measurement repeatability.

Before beginning velocity surveys, an initial experiment was performed to investigate the asymptotic invariance of Reynolds number Re_d. This was needed to ensure that dimensionless measurements will be applicable to combustors which operate at higher Re_d values than those desired for the test facility. Measurement traverses were repeated at the same conditions for increasing Re_d for each of the flowfields at $x/D = 2.5$. This axial station was chosen because a probe location slightly downstream of a recirculation zone was considered most sensitive to Re_d; and the central rather than corner zone was selected since most of the combustion and flame stability occur there. A sample of the resulting axial and swirl velocity profiles is found in Figures 49(a) and 49(b), respectively. Note that there is little change for $68{,}000 \leq Re_d \leq 92{,}000$.

Hence all measurements of the moderate $\phi = 45$ degree flowfields are performed at $Re_d = 78{,}000$. Similarly, all data for $\phi = 0$ and $\phi = 70$ degrees are obtained at $Re_d = 105{,}000$ and 78,000, respectively.

Figure 50 shows axial and swirl velocity profiles at $x/D = 1.0$ with $\alpha = 90$ and $\phi = 45$ degrees. The measurements above and below the axis were obtained from probe entry through the upper and lower wall, respectively. Although the upper and lower profiles reveal a similar shape, they exhibit different magnitudes. This shows clear evidence of a slight asymmetry in the flowfield.

Averaging the mass flow rate calculated from each radial traverse in Figure 50 results in a value within 2 percent of that measured at the test section inlet. Calculation of mass flow rate from each traverse individually yields a discrepancy of approximately 14 percent of the measured value. This asymmetry is indicative of the lack of agreement which may be expected if mass flow rate is calculated from the upper traverse only.

6.5 Prediction of Coannular Swirling Pipe Flow

6.5.1 The Flowfields Considered

Due to the rather poor agreement resulting from the special test case near the inlet of the test section, another validity test of the prediction code was undertaken. This case, experimentally investigated by Vu and Gouldin (29), has no expansion and the inlet velocity profiles do not exhibit backflow. Therefore, it is considered less difficult to predict.

This test consists of both counterswirling and coswirling flows from a coannular jet discharging into a straight pipe. A schematic

diagram of the flow assembly is illustrated in Figure 51. The assembly consists of two major segments: an inner flow passage and an outer flow channel. The inner passage consists of a circular tube with inner and outer diameters of 3.72 cm and 3.8 cm, respectively. A swirl vane assembly containing 12 equally spaced vanes with a swirl vane angle of 68.5 degrees is located 11.9 cm upstream of the discharge end of the tube.

The outer flow channel is a radial inflow passage with 24 adjustable swirl vanes near its inlet. The outer flow turns from the radial to the axial direction whereupon it exits in an annular fashion into a 14.6 cm diameter pipe where the mixing of the two streams occurs.

6.5.2 Counterswirling Case

The inner and outer flows have swirl numbers of 0.49 and -0.51, respectively. A nonuniform fine mesh of size 30 x 24 (NI = 30, NJ = 24) is arranged to cover a pipe region of length 0.17 m and radius 0.0727 m. Inlet profiles of axial and swirl velocities are taken from the measured values at the location x = 0.002 m (x/D = 0.01375), as indicated in Figure 52. Inlet k and ε (= $k^{3/2}/\ell$) are specified via

$$k = 0.03\ u^2 \tag{6.2a}$$

$$\ell = 0.005\ D/2 \tag{6.2b}$$

where D = 0.1454 m. The exit flow is parallel, with zero axial gradients for all variables and v = 0.

After a preliminary calculation of 22 iterations and a further 189 iterations, final convergence is obtained. The criterion is that the maximum normalized residual source sum for each of the variables mass, u, v, w, and p is less than 0.004. Radial profile computations of axial

and swirl velocities u and w are shown in Figure 53 at the axial station x/D = 0.137 (x = 0.02 m), and in Figure 54 at the station x/D = 0.274 (x = 0.04 m). These figures show velocities normalized with respect to a fixed quantity u_o, taken as 21.6 m/s as an estimate of the outer flow spatial average axial velocity, and the experimental data, quoted by Srinivasan and Mongia (49), have been appropriately transferred to these figures for comparison. The two axial stations chosen lie in a central zone and show dramatically the differences.

Notice that, whereas the agreement between swirl velocity profiles is very satisfactory at both locations, the agreement between axial velocity profiles is not. In the present work the central zone is predicted, but it is not as large or with such large negative velocities as found in the experiment (29). Finally, Figure 55 exhibits the centerline axial velocity development as a function of downstream location. The velocity predictions at the nearest gridline to the axis are taken as representative of axis values (r/D = 0) since $\partial u/\partial r$ is zero there. The central recirculation zone is rather well predicted in the present study, although the axial velocity magnitudes are all underpredicted.

6.5.3 Coswirling Case

The flowfield for this experiment concerns inner and outer flow swirl numbers of 0.58 and 0.54, respectively. Inlet profiles of axial u and swirl w velocities taken from the measured values at the location x = 0.002 m (x/D = 0.01375), as indicated in Figure 56. Other boundary conditions are as taken previously. Radial profile computations of axial and swirl velocities are shown in Figure 57 at the axial station x/D = 0.0688 (x = 0.01 m), and in Figure 58 at the axial station x/D = 0.2063

($x = 0.03$ m). These may be compared directly with experimental evidence given in the corresponding figures. Velocities are normalized as in the previous counterswirl case. The present predictions are very encouraging when compared to the experimental data. Finally, Figure 59 illustrates the centerline axial velocity development as a function of downstream distance. Again, velocity predictions are taken from the nearest gridline to the axis. Notice that predictions of the present study compare quite well with the experimental data, especially for $x/D \leq 0.5$.

CHAPTER VII

CLOSURE

7.1 Conclusions

The present research is concerned with a specific sub-problem of the complete three-dimensional problem and is restricted to axisymmetric geometries under low speed and nonreacting conditions. This is an area in which there is a need for more fundamental research, particularly regarding recirculation zones where most of the burning occurs in reacting flows.

Many factors affect the existence, size, and shape of both the corner recirculation zone and the central toroidal recirculation zone. A major outcome of the current study is the experimental and computational characterization of these for six basic flowfields. Parameter variations which define these flow conditions are side-wall angle α = 90 and 45 degrees with swirl vane angle ϕ = 0, 45, and 70 degrees. The size and shape of the recirculation bubbles for each flowfield is illustrated as an artistic impression deduced from a collection of flow visualization photographs of tufts, smoke, or neutrally-buoyant soap bubbles responding to the flow.

Photographed results show that increasing ϕ from 0 to 45 degrees produces a shortened corner region and the appearance of a central bubble typically extending downstream to approximately x/D = 1.7. Also, a precessing vortex core is observed which stretches from the end of the

central region to the test section exit. A further increase in ϕ to 70 degrees enlarges the central zone and vortex core with negligible effect on the corner region in those flowfields where it occurs.

The effect of α on the nonswirling flows is negligible; however, a decrease from 90 to 45 degrees apparently eliminates the corner bubble in each swirling flow. This decrease in α also causes the inlet flow to impinge more severely on the top wall, where larger axial velocities occur.

A more detailed experiment consists of the measurement of time-mean velocity components in the axial, radial, and azimuthal directions using a five-hole pitot probe. These measurements generally agree with the flow visualization results and provide a more complete understanding of each flowfield. Also, they constitute a data base allowing validity testing of flowfield predictions. Further, inlet velocity measurements reveal that the estimated inlet velocity profiles employed in the present swirling flowfield predictions are unrealistic. This arises from blade inefficiency, the presence of a hub, and the fact that the swirl vane exit station in the test facility is actually located 4 cm upstream of the test section inlet. This allows the central recirculation zone to begin upstream of the inlet where $x/D = 0$.

The flowfield prediction computer program is employed in a parametric study to computationally determine trends of interest to combustor designers. The predicted effects of α and ϕ on swirling flows are almost the same as those determined experimentally, even though the inlet velocity estimates employed consist of flat profiles with 100 percent efficient swirl vanes located at the inlet with no recirculation. Further predictions using measured inlet velocities as boundary conditions were

obtained as a special test case to allow appropriate comparison with measurements for the $\alpha = 90$ and $\phi = 45$ degree flowfield. Poor agreement results at $x/D = 0.5$, although it is excellent for $x/D \geq 1.5$. This discrepancy may be due to the lack of realism inherent in the k-ε turbulence model (extended to include swirl shear stresses), inasmuch as the empirical constants pertain to nonswirling flows. Another possibility may be an inaccurate specification of velocity and turbulence distributions at the inlet to the test section.

7.2 Recommendations for Further Work

Fundamental research should be continued in several areas. First, time-mean velocity measurements should be obtained at additional axial stations, especially in the upstream region, to provide more details and allow more extensive prediction validity tests. Second, movies of the flow visualization experiments should be obtained and analyzed to characterize the flow instabilities and temporal behavior of the recirculation zones and the trailing vortex core. Third, further details of the flowfields are needed to allow a more complete fundamental understanding. This should consist of turbulence quantity measurements, including all of the Reynolds stresses. This would allow the deduction of more sophisticated turbulence models relating turbulent shear stresses with time-mean velocity gradients.

REFERENCES

(1) Anon. The Jet Engine. 3rd ed. Pub. Ref. T.S.D. 1302. Derby, England: Rolls Royce Limited, 1969.

(2) Gerstein, M. (ed.). "Fundamentals of Gas Turbine Combustion." NASA-CP-2087, 1979. Workshop held at NASA Lewis Research Center, Cleveland, Ohio, Feb. 6-7, 1979.

(3) DOD (AFOSR and ONR) Colloquium. Gas Turbine Combustor Modeling. Meeting held at Purdue University, W. Lafayette, Ind., Sept. 5-6, 1979.

(4) Lilley, D. G. "Flowfield Modeling in Practical Combustors: A Review." Journal of Energy, Vol. 3 (July-Aug., 1979), pp. 193-210.

(5) Rhode, D. L., D. G. Lilley, and D. K. McLaughlin. "On the Prediction of Swirling Flowfields Found in Axisymmetric Combustor Geometries." Proceedings, ASME Symposium on Fluid Mechanics of Combustion Systems. Boulder, Colo., June 22-24, 1981, pp. 257-266.

(6) Murthy, S. N. B. Summary Report: DOD Colloquium on Gas Turbine Combustor Modeling. Project SQUID, Technical Report PU-R1-79. School of Mechanical Engineering, Purdue University (for ONR), Nov., 1979.

(7) Lefebvre, A. H. (ed.). Gas Turbine Combustor Design Problems. New York: Hemisphere-McGraw-Hill, 1980.

(8) Rhode, D. L. "Prediction of Combustor Flowfields." Proceedings, 11th Southwestern Graduate Research Conference in Applied Mechanics, Stillwater, Okla., Apr. 11-12, 1980.

(9) Lilley, D. G., D. L. Rhode, and J. W. Samples. "Prediction of Swirling Reacting Flow in Ramjet Combustors." AIAA Paper No. 81-1485. Colorado Springs, Colo., July 25-27, 1981.

(10) Lilley, D. G. "Prospects for Computer Modeling in Ramjet Combustors." AIAA Paper No. 80-1189. Hartford, Conn., June 30-July 2, 1980.

(11) Lilley, D. G., and D. L. Rhode. STARPIC: A Computer Code for Swirling Turbulent Axisymmetric Recirculating Flows in Practical Isothermal Combustor Geometries. NASA CR-3442, 1981.

(12) Gupta, A. K., D. G. Lilley, and N. Syred. Swirl Flows. Tunbridge Wells, England: Abacus Press, 1981.

(13) Beer, J. M., and N. A. Chigier. Combustion Aerodynamics. London: Applied Science; and New York: Halsted-Wiley, 1972.

(14) Lilley, D. G. "Swirl Flows in Combustion: A Review." AIAA Journal, Vol. 15, No. 8 (Aug., 1977), pp. 1063-1078.

(15) Chaturvedi, M. C. "Flow Characteristics of Axisymmetric Expansions." Proceedings, Journal of the Hydraulics Division, ASCE, Vol. 89, No. HY3 (1963), pp. 61-92.

(16) Krall, K. M., and E. M. Sparrow. "Turbulent Heat Transfer in the Separated, Reattached, and Redevelopment Regions of a Circular Tube." Journal of Heat Transfer (Feb., 1966), pp. 131-136.

(17) Phaneuf, J. T., and D. W. Netzer. Flow Characteristics in Solid Fuel Ramjets. Report No. NPS-57Nt74081. Prepared for the Naval Weapons Center by the Naval Postgraduate School, July, 1974.

(18) Back, L. H., and E. J. Roschke. "Shear Layer Flow Regimes and Wave Instabilities and Reattachment Lengths Downstream of an Abrupt Circular Channel Expansion." Journal of Applied Mechanics (Sept., 1972), pp. 677-681.

(19) Roschke, E. J., and L. H. Back. "The Influence of Upstream Conditions on Flow Reattachment Lengths Downstream of an Abrupt Circular Channel Expansion." Journal of Biomechanics, Vol. 9 (1976), pp. 481-483.

(20) Ha Minh, H., and P. Chassaing. "Perturbations of Turbulent Pipe Flow." Proceedings, Symposium on Turbulent Shear Flows. Pennsylvania State University, April, 1977, pp. 13.9-13.17.

(21) Moon, L. F., and G. Rudinger. "Velocity Distribution in an Abruptly Expanding Circular Duct." Journal of Fluids Engineering (March, 1977), pp. 226-230.

(22) Johnson, B. V., and J. C. Bennett. "Velocity and Concentration Characteristics and Their Cross Correlation for Coaxial Jets in a Confined Sudden Expansion; Part II: Predictions." Proceedings, ASME Symposium on Fluid Mechanics of Combustion Systems. Boulder, Colo., June 22-23, 1981, pp. 145-160.

(23) Hiett, G. F., and G. E. Powell. "Three-Dimensional Probe for Investigation of Flow Patterns." The Engineer (Jan., 1962), pp. 165-170.

(24) Mathur, M. L., and N. R. L. MacCallum. "Swirling Air Jets Issuing From Vane Swirlers. Part 1: Free Jets; Part 2: Enclosed Jets." Journal of the Inst. of Fuel, Vol. 40 (May, 1967), pp. 214-224, and (June, 1967), pp. 238-245.

(25) Owen, F. K. "Laser Velocimeter Measurements of a Confined Turbulent Diffusion Flame Burner." AIAA Paper No. 76-33. Washington, D.C., Jan. 26-28, 1976.

(26) Baker, R. J., P. Hutchinson, E. E. Khalil, and J. H. Whitelaw. "Measurements of Three Velocity Components in a Model Furnace With and Without Combustion." Proceedings, 15th Symposium on Combustion, The Combustion Institute, Pittsburgh, Penn., 1975, pp. 553-559.

(27) Beltagui, S. A., and N. R. L. MacCallum. "Aerodynamics of Vane-Swirled Flames in Furnaces." Journal of the Inst. of Fuel, Vol. 49 (Dec., 1979), pp. 183-193.

(28) Beltagui, S. A., and N. R. L. MacCallum. "The Modeling of Vane-Swirled Flames in Furnaces." Journal of the Inst. of Fuel, Vol. 49 (Dec., 1979), pp. 193-200.

(29) Vu, B. T., and F. C. Gouldin. "Flow Measurements in a Model Swirl Combustor." AIAA Paper No. 80-0076. Pasadena, Calif., Jan. 14-16, 1980.

(30) Syred, N., J. M. Beer, and N. A. Chigier. "Turbulence Measurements in Swirling Recirculating Flows." Proceedings, Salford Symposium on Internal Flows. London, England: Inst. of Mechanical Engineering, 1971, pp. B27-B36.

(31) Lipstein, N. J. "Low Velocity Sudden Expansion Pipe Flow." Paper presented at ASHRAE 69th Annual Meeting, Miami Beach, Fla., June 25-27, 1962.

(32) Zemanick, P. P., and R. S. Dougall. "Local Heat Transfer Downstream of an Abrupt Circular Channel Expansion." Journal of Heat Transfer (Feb., 1970), pp. 53-60.

(33) Pratte, B. D., and J. R. Keffer. "The Swirling Turbulent Jet." Journal of Basic Engineering, Vol. 94 (Dec., 1972), pp. 739-748.

(34) Syred, N., and K. R. Dahman. "Effect of High Levels of Confinement Upon the Aerodynamics of Swirl Burners." Journal of Energy, Vol. 2 (Jan.-Feb., 1978), pp. 8-15.

(35) Macagno, E. O., and T. Hung. "Computational and Experimental Study of a Captive Annular Eddy." Journal of Fluid Mechanics, Vol. 28 (1967), pp. 43-64.

(36) Runchal, A. K., and D. B. Spalding. Steady Turbulent Flow and Heat Transfer Downstream of a Sudden Enlargement in a Pipe of Circular Cross Section. Report EF/TN/A/39. Dept. of Mech. Engr., Imperial College, London, England, June, 1974.

(37) Launder, B. E., A. Morse, W. Rodi, and D. B. Spalding. "The Prediction of Free Shear Flows--A Comparison of the Performance of Six Turbulence Models." Proceedings, NASA Conference on Free Shear Flows. NASA Langley Research Center, Hampton, Va., 1972.

(38) Launder, B. E., and D. B. Spalding. "The Numerical Computation of Turbulent Flows." Computational Methods in Applied Mechanics and Engineering, Vol. 3 (Mar., 1974), pp. 269-289.

(39) Peck, R. E., and G. S. Samuelson. "Eddy Viscosity Modeling in the Prediction of Turbulent Backmix Combustion Performance." 16th International Symposium on Combustion. The Combustion Institute, Pittsburgh, Pa., 1977, pp. 1675-1687.

(40) Wuerer, J. B., and G. S. Samuelson. "Predictive Modeling of Backmixed Combustor Flows: Mass and Momentum Transport." AIAA Paper No. 79-0215. New Orleans, La., January 15-17, 1979.

(41) Roberts, L. W. "Turbulent Swirling Flows with Recirculation." (Ph.D. thesis, Imperial College, London, England, 1972.)

(42) Khalil, E. E., D. B. Spalding, and J. H. Whitelaw. "The Calculation of Local Flow Properties in Two-Dimensional Furnaces." Int. Journal of Heat Transfer, Vol. 18 (1975), pp. 775-791.

(43) Hutchinson, P., E. E. Khalil, J. H. Whitelaw, and G. Wigley. "The Calculation of Furnace-Flow Properties and Their Experimental Verification." Journal of Heat Transfer (May, 1976), pp. 276-283.

(44) Lilley, D. G. "Primitive Pressure-Velocity Code for the Computation of Strongly Swirling Flows." AIAA Journal, Vol. 14, No. 6 (June, 1976), pp. 749-756.

(45) Serag-Eldin, M. A., and D. B. Spalding. "Computations of Three-Dimensional Gas Turbine Combustion Chamber Flows." Transactions ASME, Journal of Engineering for Power, Vol. 101 (July, 1979), pp. 326-336.

(46) Novick, A. S., G. A. Miles, and D. G. Lilley. "Modeling Parameter Influences in Gas Turbine Combustor Design." Journal of Energy, Vol. 3, No. 5 (Sept.-Oct., 1979), pp. 257-262.

(47) Novick, A. S., G. A. Miles, and D. G. Lilley. "Numerical Simulation of Combustor Flow Fields." Journal of Energy, Vol. 3, No. 2 (Mar.-Apr., 1979), pp. 95-105.

(48) Habib, M. A., and J. H. Whitelaw. "Velocity Characteristics of Confined Coaxial Jets With and Without Swirl." ASME Paper 79-WA/FE-21. New York, NY, Dec. 2-7, 1979.

(49) Srinivasan, R., and H. C. Mongia. Numerical Computations of Swirling Recirculating Flows. NASA CR-156196. Sept., 1980.

(50) Syed, S. A., and G. J. Sturgess. "Validation Studies of Turbulence and Combustion Models for Aircraft Gas Turbine Combustors." ASME Symposium on Momentum and Heat Transfer Processes in Recirculating Flows. HTD--Vol. 13. Chicago, Ill, Nov., 1980, pp. 71-89.

(51) Syed, S. A., and G. J. Sturgess. "Velocity and Concentration Characteristics and Their Cross Correlation for Co-Axial Jets in a Confined Sudden Expansion. Part II: Predictions." Proceedings, ASME Symposium on Fluid Mechanics of Combustion Systems. Boulder, Colo., June 22-23, 1981, pp. 161-167.

(52) Sturgess, G. J., S. A. Syed, and D. Sepulveda. "Application of Numerical Modeling to Gas Turbine Combustor Development Problems." Proceedings, ASME Symposium on Fluid Mechanics of Combustion Systems. Boulder, Colo., June 22-23, 1981, pp. 241-250.

(53) Morel, T. (ed.). Prediction of Turbulent Reacting Flows in Practical Systems. Session presented at ASME Fluids Engineering Conference, Boulder, Colo., June 22-23, 1981. (See papers by C. K. Westbrook, F. L. Dryer, W. P. Jones, J. H. Whitelaw, and P. T. Harsha.)

(54) Mongia, H. C., and R. S. Reynolds. Combustor Design Criteria Validation Vol. III--User's Manual. Report USARTL-TR-78-55C, U.S. Army Res. and Tech. Lab., Ft. Eustis, Va., Feb., 1979. (See also Vols. I and II.)

(55) Swithenbank, J., A. Turan, and P. G. Felton. "Three-Dimensional Two-Phase Mathematical Modeling of Gas Turbine Combustors." Paper in Gas Turbine Combustor Design Problems. A. H. Lefebvre, Ed. New York: Hemisphere-McGraw-Hill, 1980, p. 249.

(56) Roache, P. J. Computational Fluid Dynamics. Albuquerque: Hermosa, 1972.

(57) Chow, C-Y. An Introduction to Computational Fluid Mechanics. New York: John Wiley, 1979.

(58) Patankar, S. V. Numerical Heat Transfer and Fluid Flow. New York: Hemisphere-McGraw-Hill, 1980.

(59) McDonald, H. "Combustion Modeling in Two and Three Dimensions--Some Numerical Considerations." Prog. in Energy and Combustion Science, Vol. 5 (1979), pp. 97-122.

(60) Gosman, A. D., and W. M. Pun. Calculation of Recirculating Flows. Report No. HTS/74/12. Dept. of Mechanical Engineering, Imperial College, London, England, 1974.

(61) El Banhawy, Y., and J. H. Whitelaw. "Calculation of the Flow Properties of a Confined Kerosene-Spray Flame." AIAA Journal, Vol. 18, No. 2 (Dec., 1980), pp. 1503-1510.

(62) Launder, B. E., and D. B. Spalding. Mathematical Models of Turbulence. London, England: Academic Press, 1972.

(63) Launder, B. E., and D. B. Spalding. "The Numerical Computation of Turbulent Flows." Computational Methods in Applied Mechanics and Engineering, Vol. 3 (Mar., 1974), pp. 269-289.

(64) Gosman, A. D., W. M. Pun, A. K. Runchal, D. B. Spalding, and M. W. Wolfshtein. Heat and Mass Transfer in Recirculating Flows. London, England: Academic Press, 1969.

(65) Gosman, A. D., and F. J. K. Ideriah. TEACH-2E: A General Computer Program for Two-Dimensional Turbulent, Recirculating Flows. Report, Dept. of Mechanical Engineering, Imperial College, London, England, June, 1976.

(66) Morel, T. "Comprehensive Design of Axisymmetric Wind Tunnel Contractions." ASME Paper 75-FE-17. Minneapolis, Minn., May 5-7, 1975.

(67) Eskilson, E., L. Jackson, C. Jones, T. Lester, and M. Morein. "An Effort Towards Wind Tunnel Design and Modification to Allow Simulation of the Flowfield in a Gas Turbine Combustor." Senior Research Project Report. School of Mechanical and Aerospace Engineering, Oklahoma State University, May, 1980.

(68) Swedeen, R., and Z. Arashmidos. "Student Activity on a Swirling Jet Apparatus." Senior Research Project Report. School of Mechanical and Aerospace Engineering, Oklahoma State University, Aug., 1980.

(69) Lock, C. N. H. Photographs of Streamers Illustrating the Flow Around an Airscrew in the "Vortex Ring State." ARC Reports and Memorandum No. 1167. Apr., 1928.

(70) Redon, M. H., and M. F. Vinsonneau. "Étude de l'Écoulement de l'Air Autour d'une Maquette, L'Aéronautique." Bulletin L'Aérotechnique, Vol. 18, No. 204 (May, 1936), pp. 60-66.

(71) Kampé de Fériet, J. "Some Recent Research on Turbulence." Proceedings, 5th International Congress for Applied Mechanics, Cambridge, Mass., Sept. 12-16, 1938, pp. 352-355; New York: John Wiley & Sons, 1939.

(72) Owen, F. S., R. W. Hale, B. V. Johnson, and A. Travers. Experimental Investigation of Characteristics of Confined Jet-Driven Vortex Flows. Report R-2494-2. United Aircraft Research Laboratories, Nov., 1961.

(73) Hale, R. W. et al. Development of an Integrated System for Flow Visualization in Air Using Neutrally-Buoyant Bubbles. Report SAI-RR 7107. Sage Action, Inc. for ONR, Dec., 1971.

(74) Cornish, J. J. "A Device for the Direct Measurements of Unsteady Air Flows and Some Characteristics of Boundary Layer Transition." Aerophysics Research Note 24. Mississippi State University, 1964, p. 1.

(75) Sanders, C. J., and J. F. Thompson. An Evaluation of the Smoke-Wire Technique of Measuring Velocities in Air. Aerophysics Research Report 70. Mississippi State University, Oct., 1966.

(76) Yamada, H. "Instantaneous Measurements of Air Flows by Smoke-Wire Technique." Transactions of Japan Mechanical Engineers, Vol. 39 (1973), p. 726.

(77) Corke, T., D. Koga, R. Drubka, and H. Nagib. "A New Technique for Introducing Controlled Sheets of Smoke Streaklines in Wind Tunnels." Proceedings, International Congress on Instrumentation in Aerospace Simulation Facilities. IEEE Publ. 77 CH 1251-8 AES, 1974, p. 74.

(78) Nagib, H. M. "Visualization of Turbulent and Complex Flows Using Controlled Sheets of Smoke Streaklines." Proceedings, International Symposium on Flow Visualization. Tokyo, Oct., 1977, pp. 181-186 (also supplement 29-1 to 29-7).

(79) Cornell, D. Smoke Generation for Flow Visualization. Aerophysics Research Report 54. Mississippi State University, Nov., 1964.

(80) Abdul-Karim, S., D. Gaddis, and P. Paden. "Smoke-Wire Flow Visualization." Senior Research Project Report. School of Mechanical and Aerospace Engineering, Oklahoma State University, Mar., 1981.

(81) Bird, J. D. "Visualization of Flow Fields by Use of a Tuft Grid Technique." Journal of Aeronautical Science, Vol. 19 (1952), pp. 481-485.

(82) Gersten, K. "Untersuchungen über den Abwind hinter Deltaflügeln bei inkompressibler Strömung." Jahrb. Wiss. Ges. Luft-Raumfahrt (1955), pp. 151-161.

(83) McMahon, H. M., D. D. Hester, and J. G. Palfery. "Vortex Shedding From a Turbulent Jet in a Cross-Wind." Journal of Fluid Mechanics, Vol. 48 (1971), pp. 73-80.

(84) Breyer, D. W., and R. C. Pankhurst. Pressure-Probe Methods for Determining Wind Speed and Flow Direction. London, England: Her Majesty's Stationary Office, 1971.

(85) Janes, C. E. Instruments and Methods for Measuring the Flow of Water Around Ships and Ship Models. David Taylor Model Basin Report No. 487, Mar., 1948.

(86) Meyer, H. "Onderzoek Betreffend de Meet-methode Met de Pitot-Buis van Dr. Ing. J. J. Borren." (Investigation on the Method of Measurement With Pitot Tube, designed by Dr. J. J. Borren.) De Ingenieur (July 7, 1928), p. 173.

(87) Gutsche, F. "Das Zylinderstaurohr." (The Cylindrical Pitot Tube.) Schiffbau, Shiffart, and Hafenbau, Vol. 32 (Jan., 1931), pp. 13-19.

(88) Pien, P. C. The Five-Hole Spherical Pitot Tube. David Taylor Model Basin Report No. 1229, May, 1958.

(89) Lee, J. C., and J. B. Ash. "A Three-Dimensional Spherical Pitot Probe." Transactions, ASME (Apr., 1956), pp. 603-608.

(90) Hale, M. R., and D. H. Norrie. "The Analysis and Calibration of the Five-Hole Spherical Pitot." ASME Paper 67-WA/FE-24. Pittsburgh, Penn., Nov. 12-17, 1967.

(91) Syred, N., and J. M. Beer. "Combustion in Swirling Flows: A Review." Combustion and Flame, Vol. 23 (1974), pp. 143-201.

APPENDIX A

TABLE I

SOURCE TERM IN THE GENERAL EQUATIONS

ϕ	S_ϕ
u	$-\frac{\partial p}{\partial x} + S^u$
v	$-\frac{\partial p}{\partial r} + \frac{\rho w^2}{r} - \frac{2\mu v}{r^2} + S^v$
w	$-\frac{\rho v w}{r} - \frac{w}{r^2}\frac{\partial}{\partial r}(r\mu) + S^w$
k	$G - C_D \rho \varepsilon$
ε	$(C_1 \varepsilon G - C_2 \rho \varepsilon^2)/k$

APPENDIX B - FIGURES

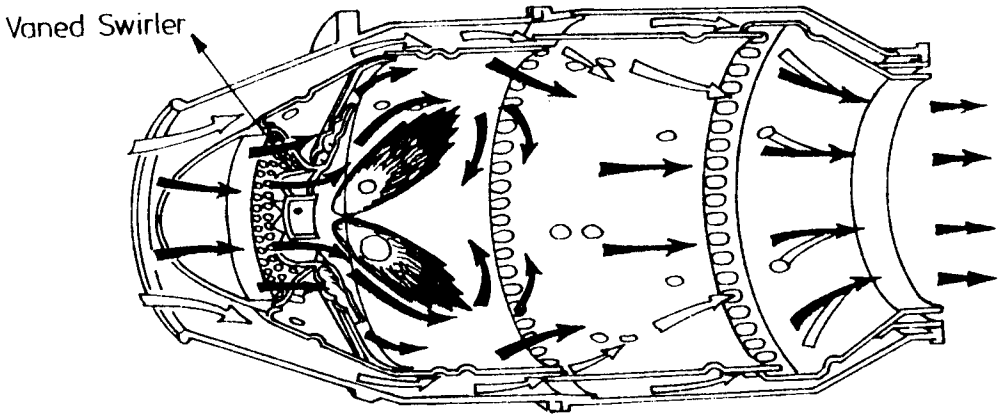

Figure 1. Typical Axisymmetric Combustion Chamber of a Gas Turbine Engine (1)

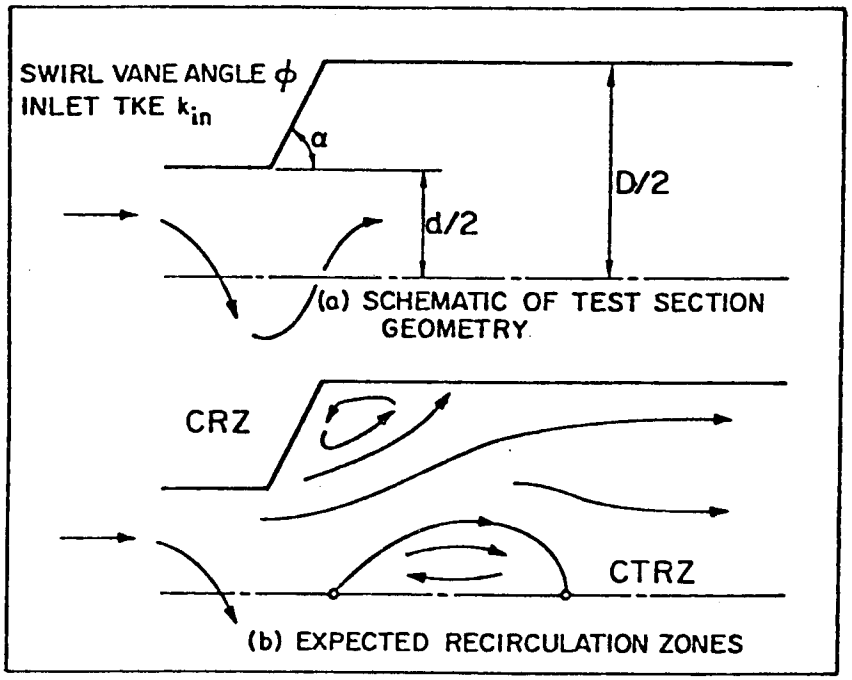

Figure 2. The Flowfield Being Investigated

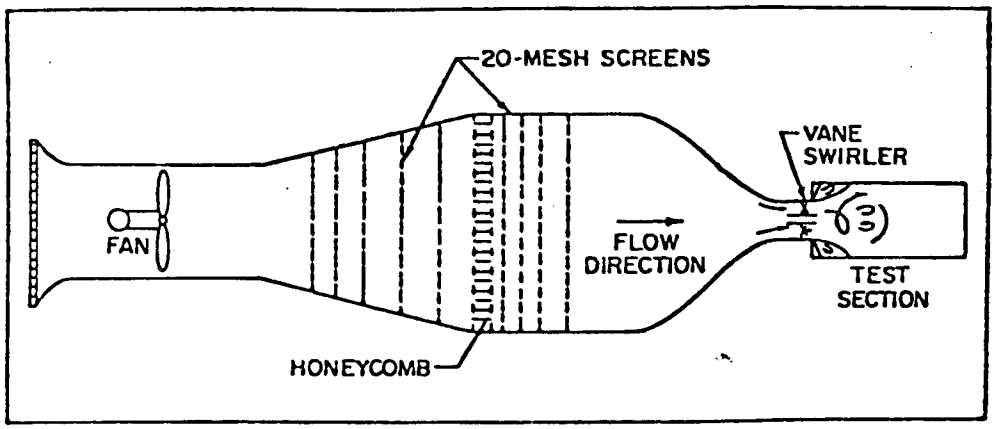

Figure 3. Schematic of Overall Flow Facility

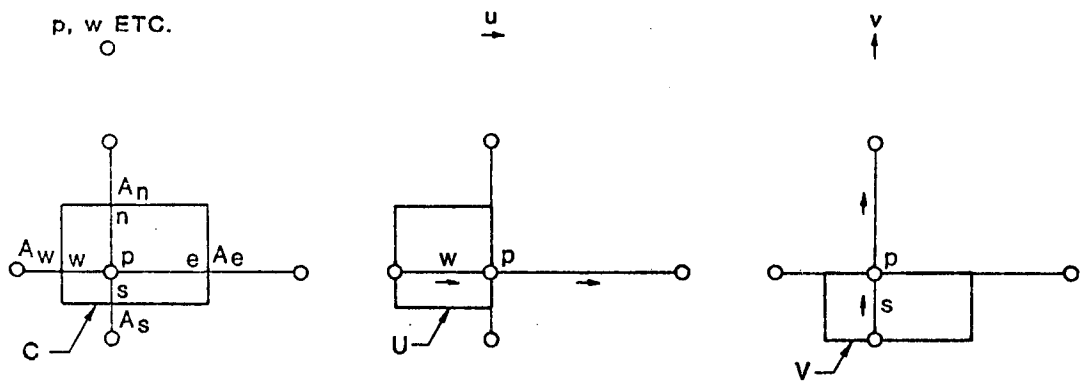

CONTROL VOLUMES C, U, V FACE
AREAS A_n, A_s, A_e AND A_w FOR C, SIMILAR FOR U AND V

Figure 4. The Three Control Volumes Associated With Points of the Three Grids

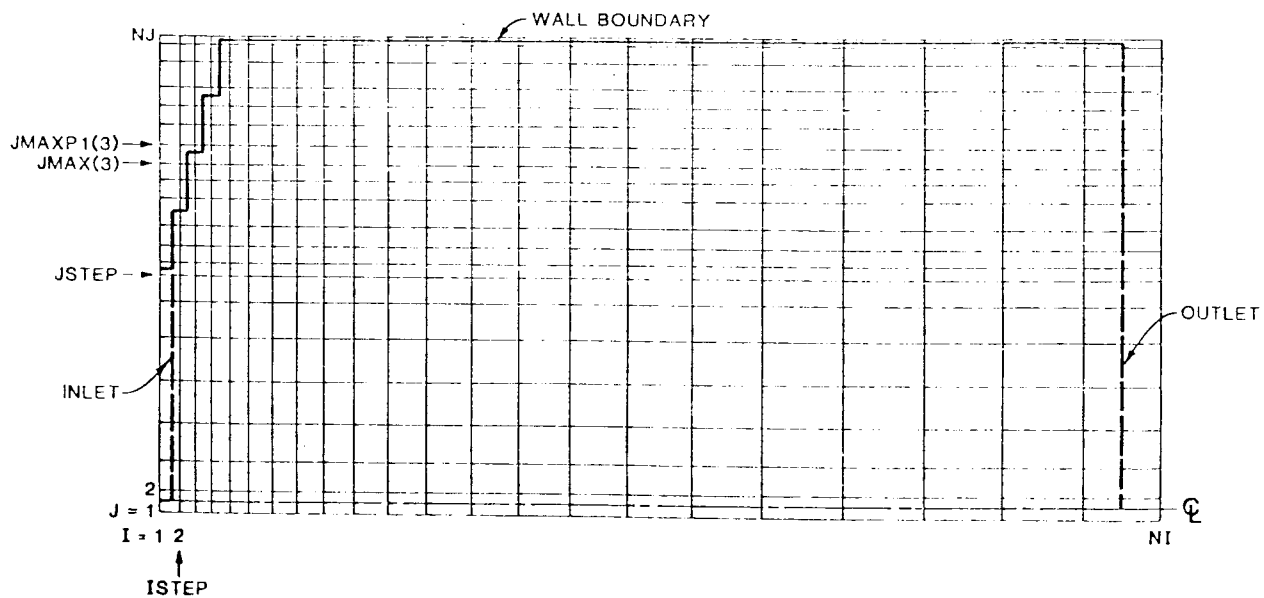

Figure 5. An Example of a Coarse Grid System Being Employed to Fit the Flow Domain

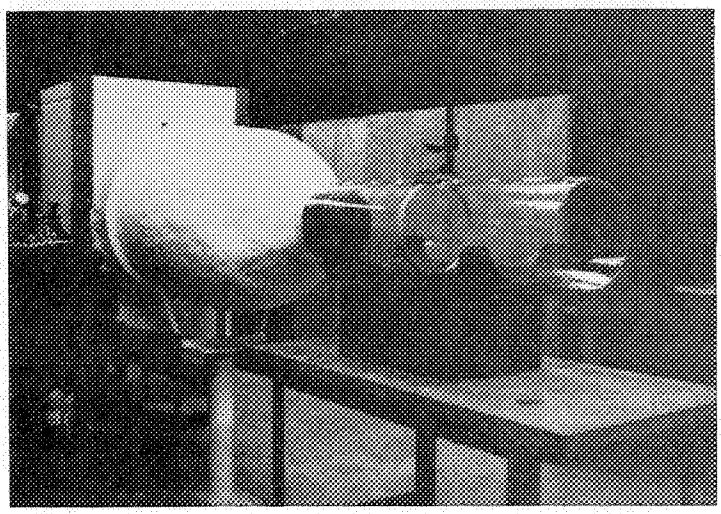

Figure 6. General View of the Test Facility

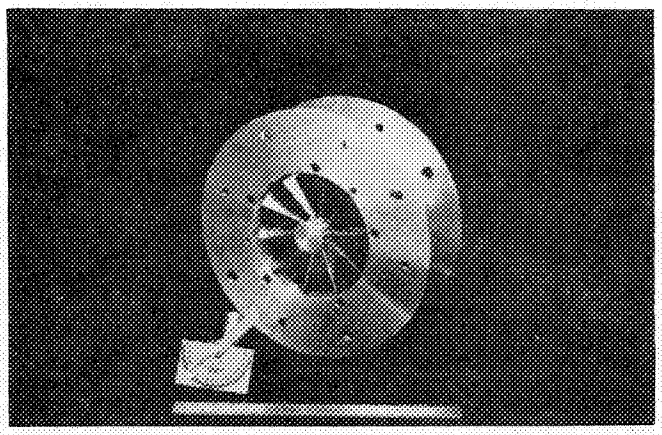

Figure 7. View of the Swirl Vane Assembly From Upstream

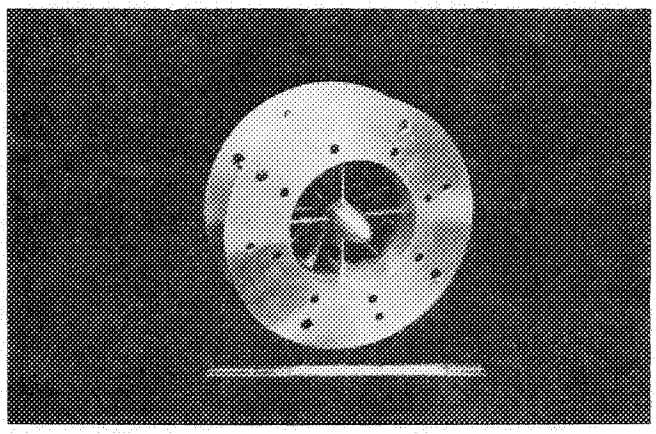

Figure 8. View of the Swirl Vane Assembly From Downstream With the Instrument for Measuring the Vane Angle

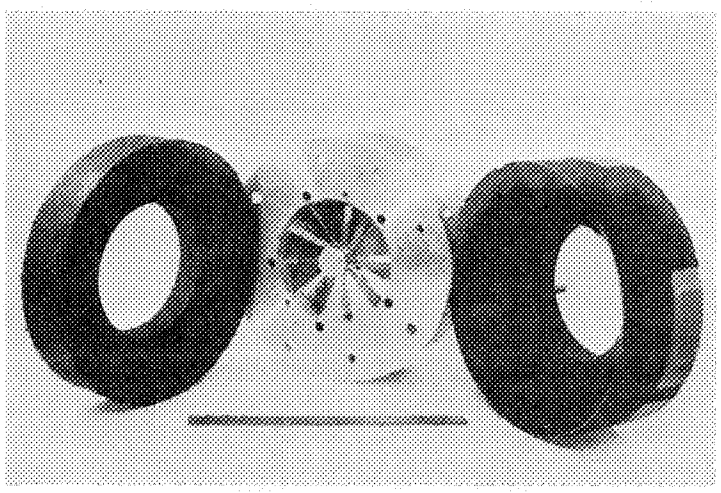

Figure 9. View of Swirler With 70° and 45° Expansion Blocks

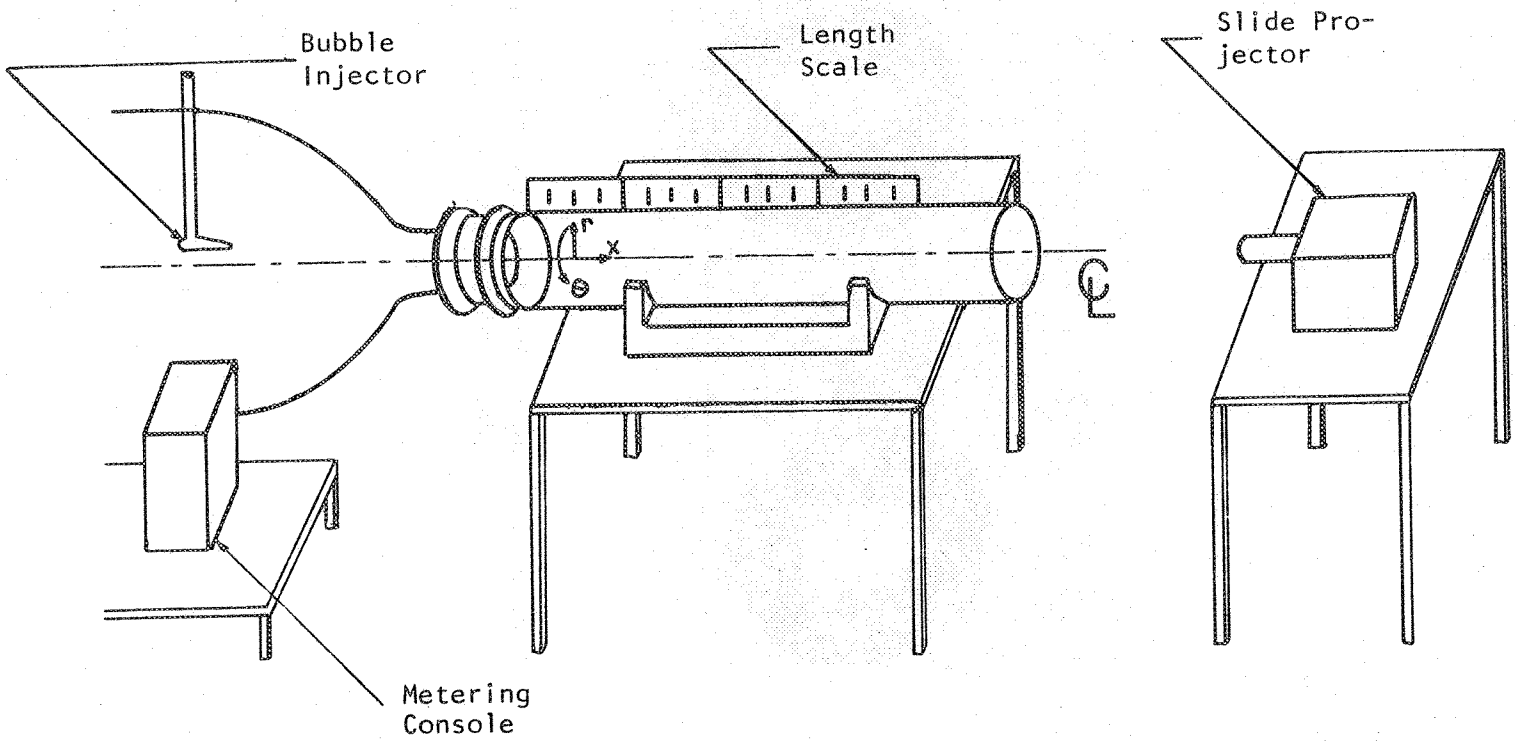

Figure 10. Apparatus for Neutrally-Buoyant Bubble Flow Visualization Experiment

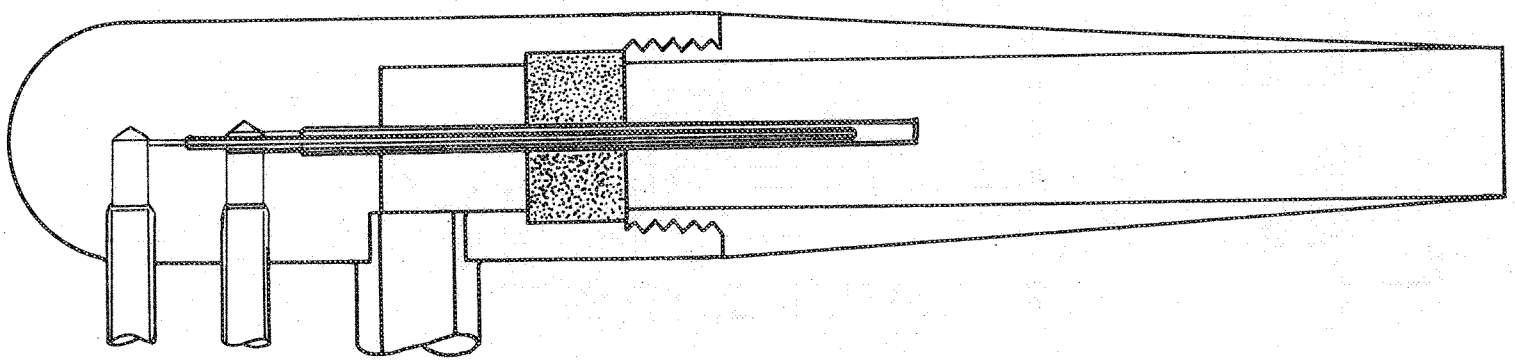

Figure 11. Neutrally-Buoyant Bubble Injector (73)

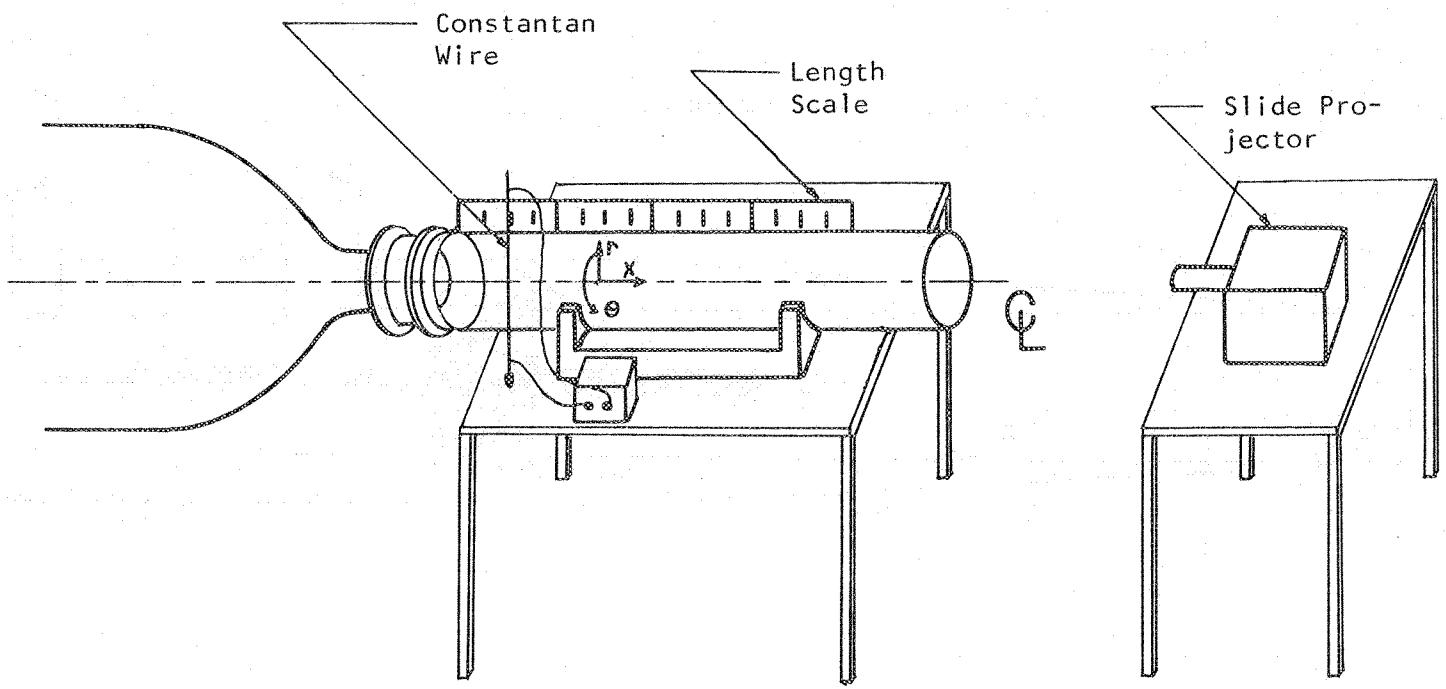

Figure 12. Apparatus for the Smoke-Wire Flow Visualization Experiment

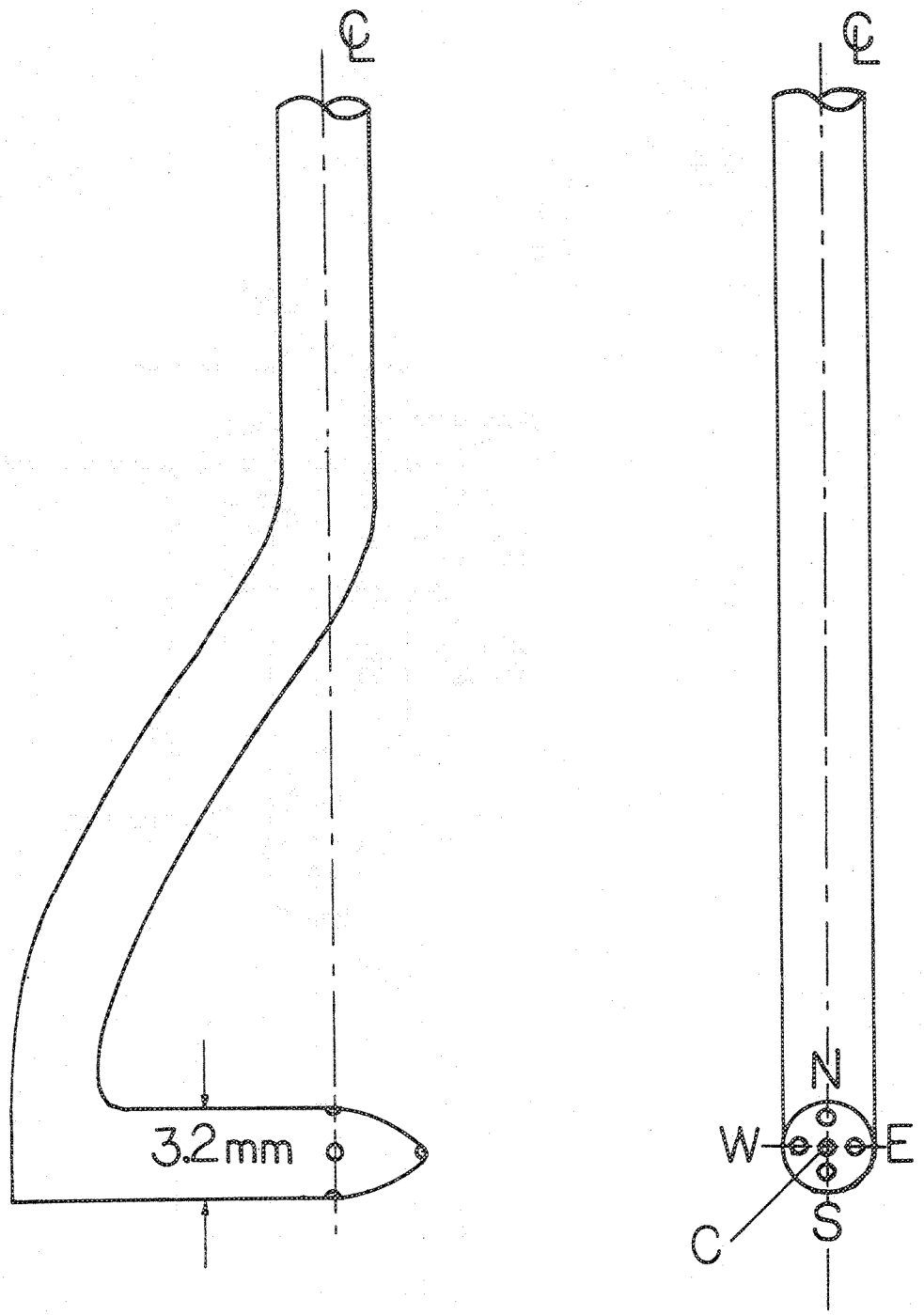

Figure 13. Five-Hole Pitot Probe

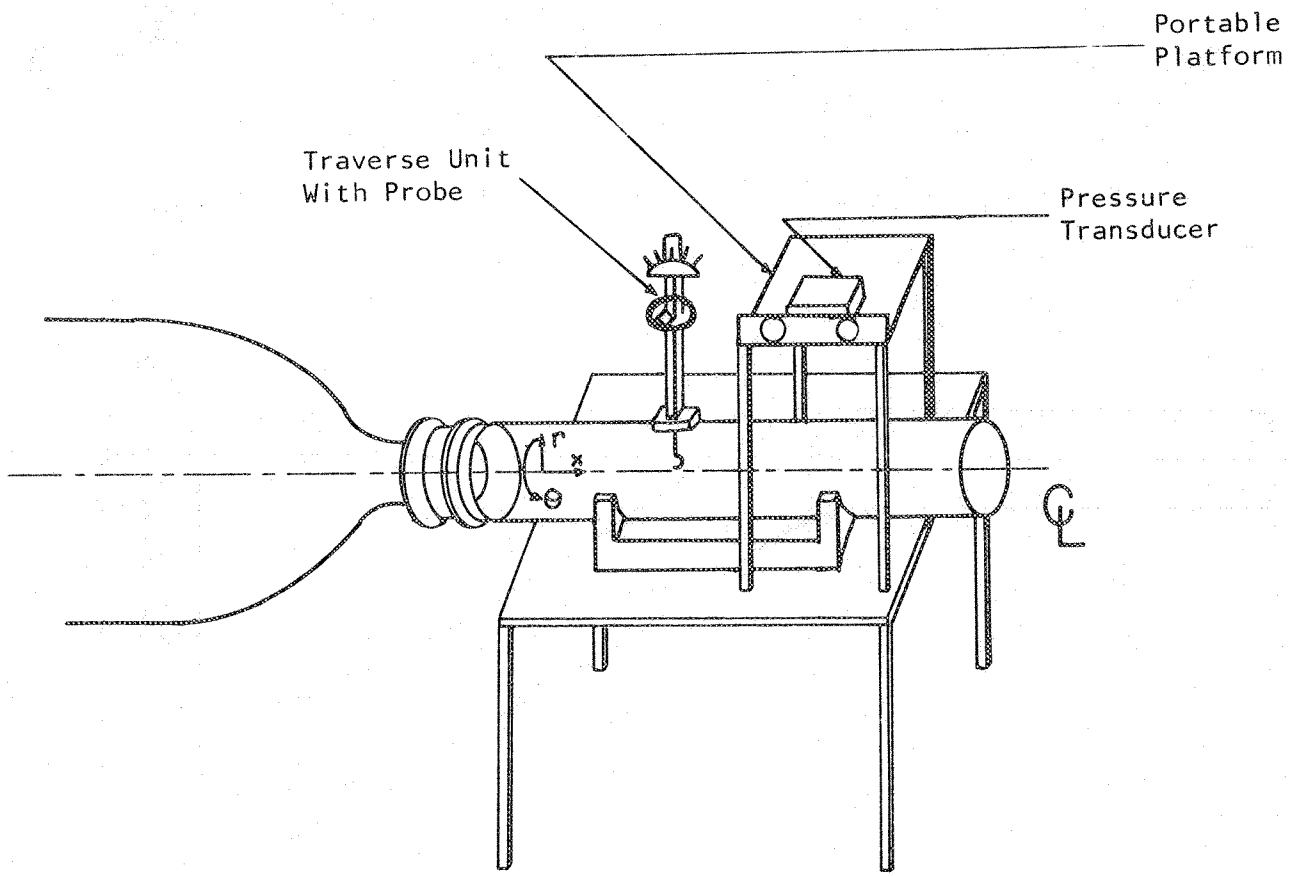

Figure 14. Apparatus for Mean Velocity Measurements Using a Five-Hole Pitot Probe

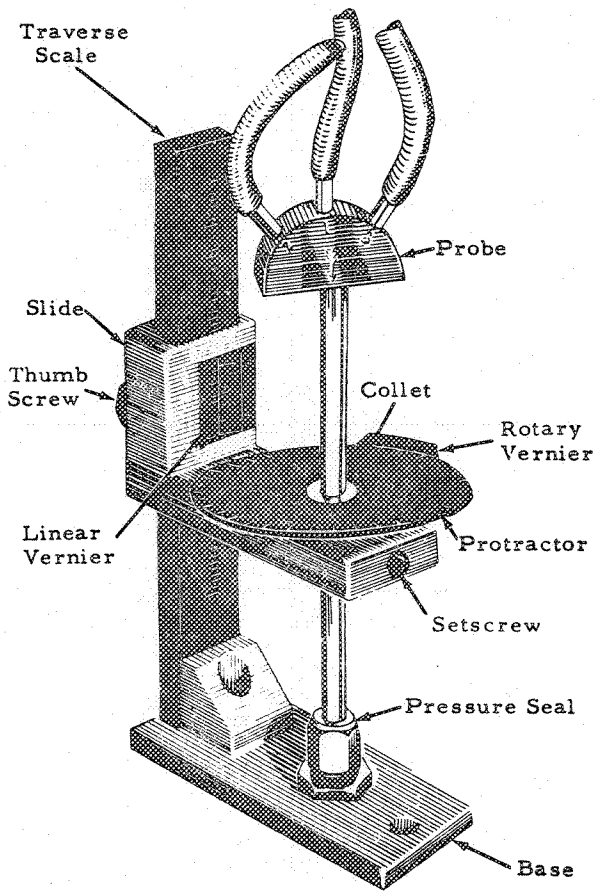

Figure 15. Manual Traverse Mechanism Used for Five-Hole Pitot Measurements

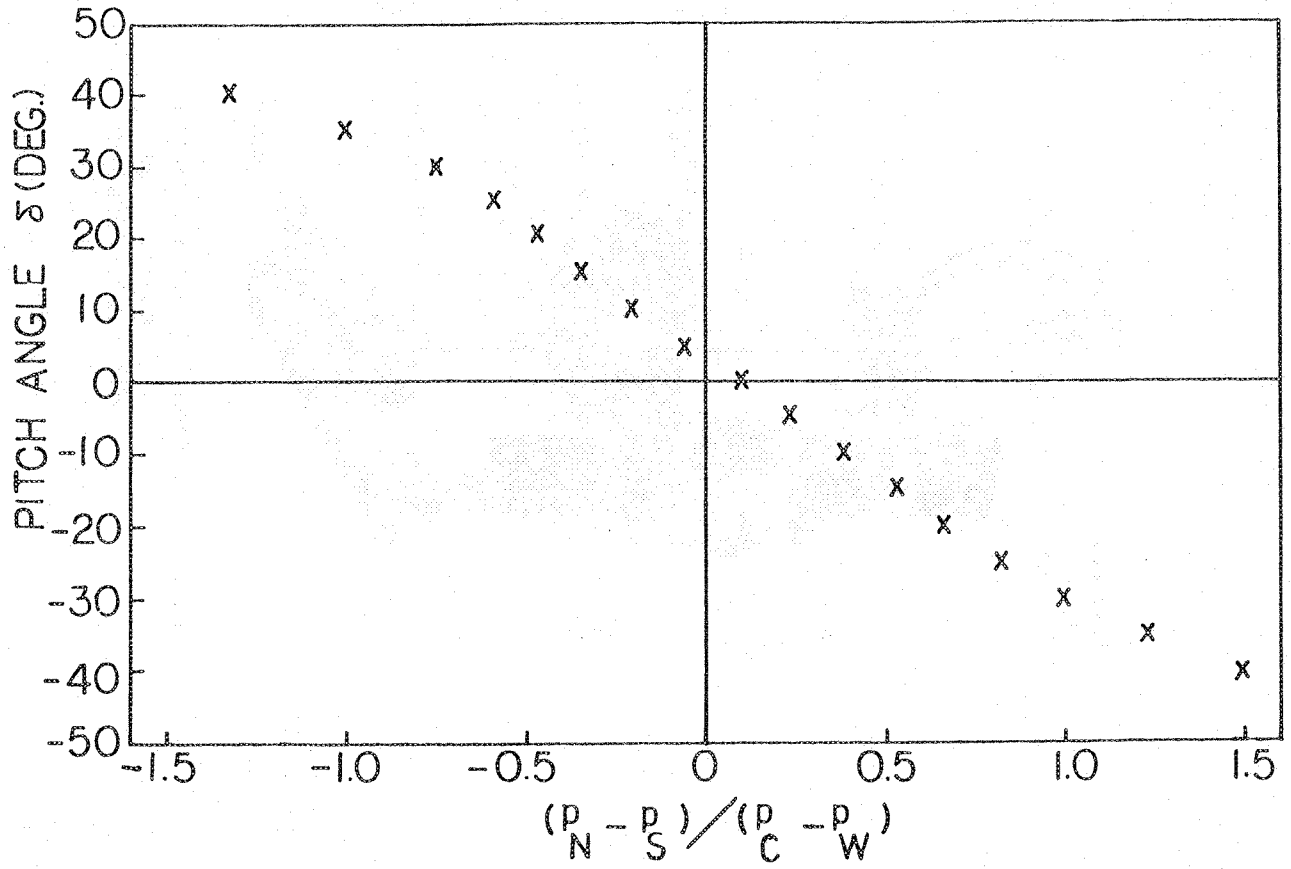

Figure 16. Pitch Angle Calibration Characteristic for Five-Hole Pitot Probe

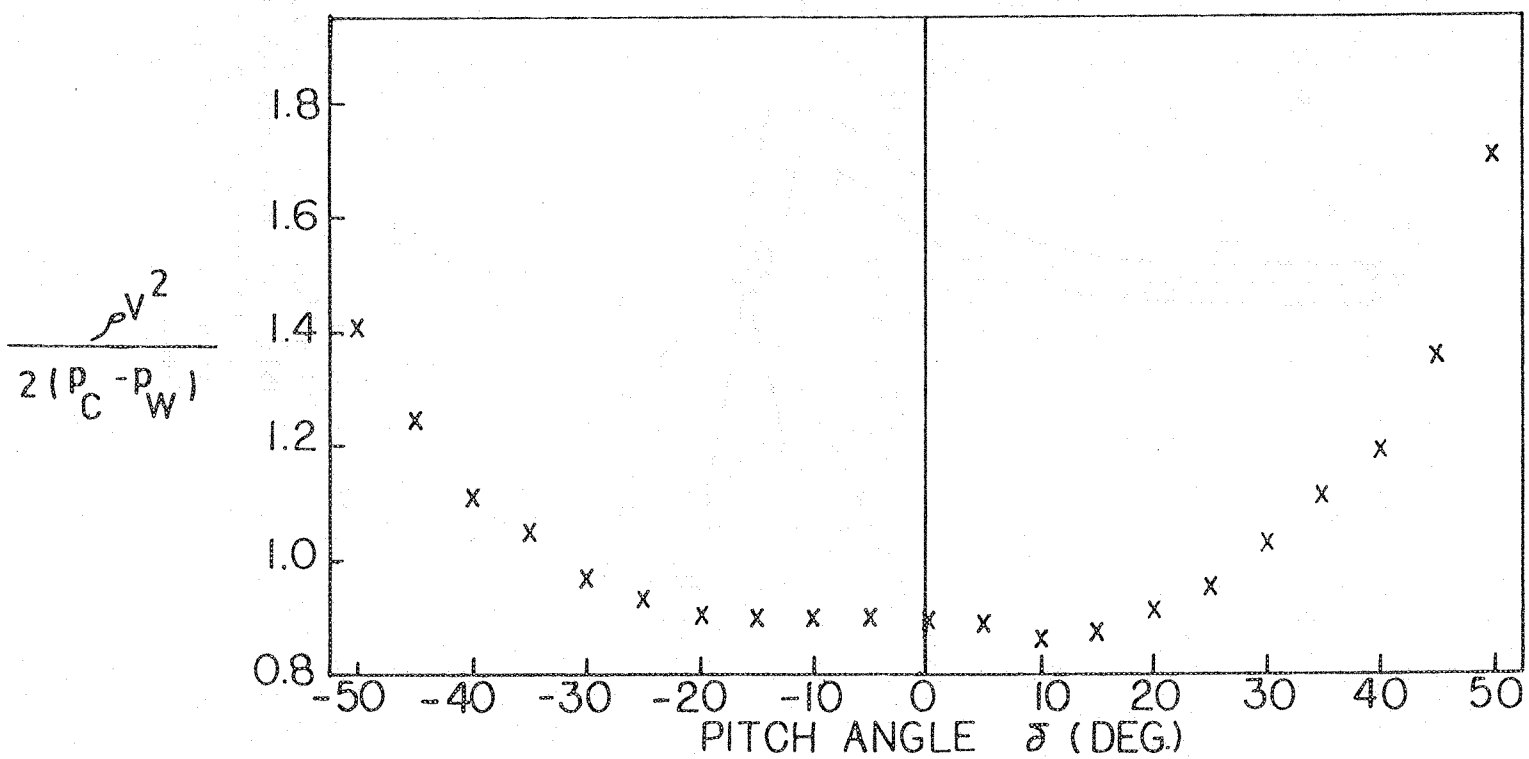

Figure 17. Velocity Coefficient Calibration Characteristic for the Five-Hole Pitot Probe

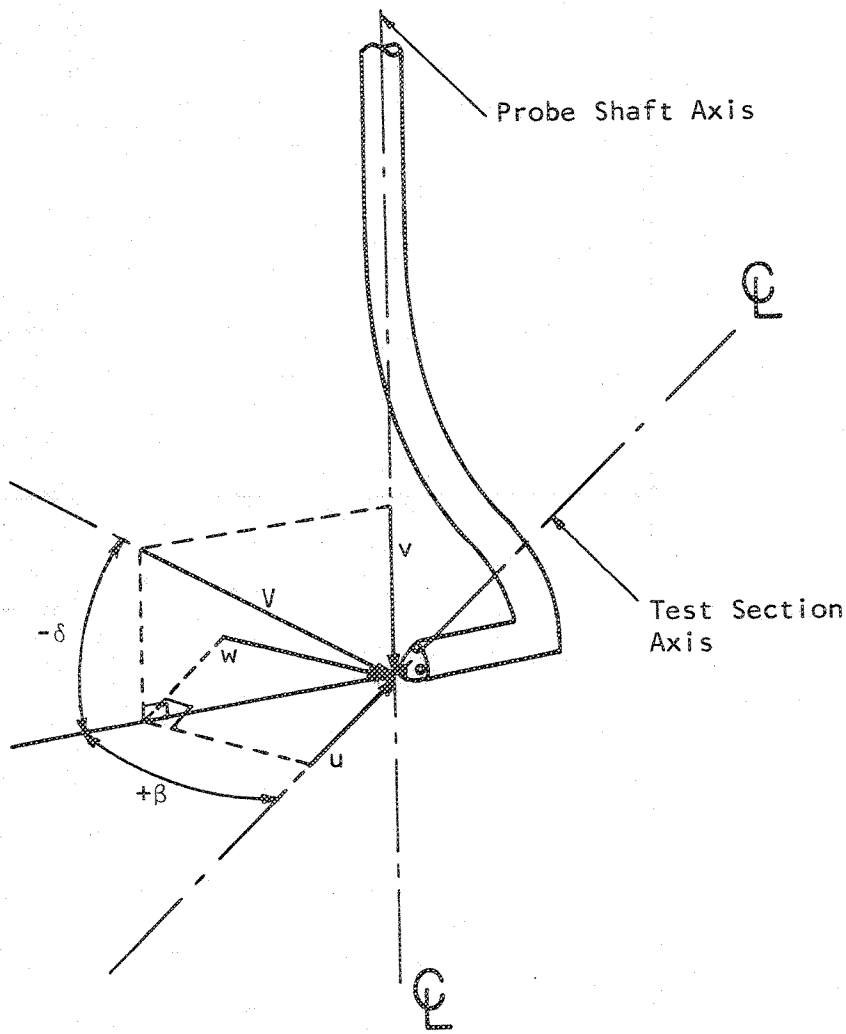

Figure 18. Velocity Components and Flow Direction Angles Associated With Five-Hole Pitot Measurements (Yaw Angle β in the Horizontal Plane and Pitch Angle δ in the Vertical Plane

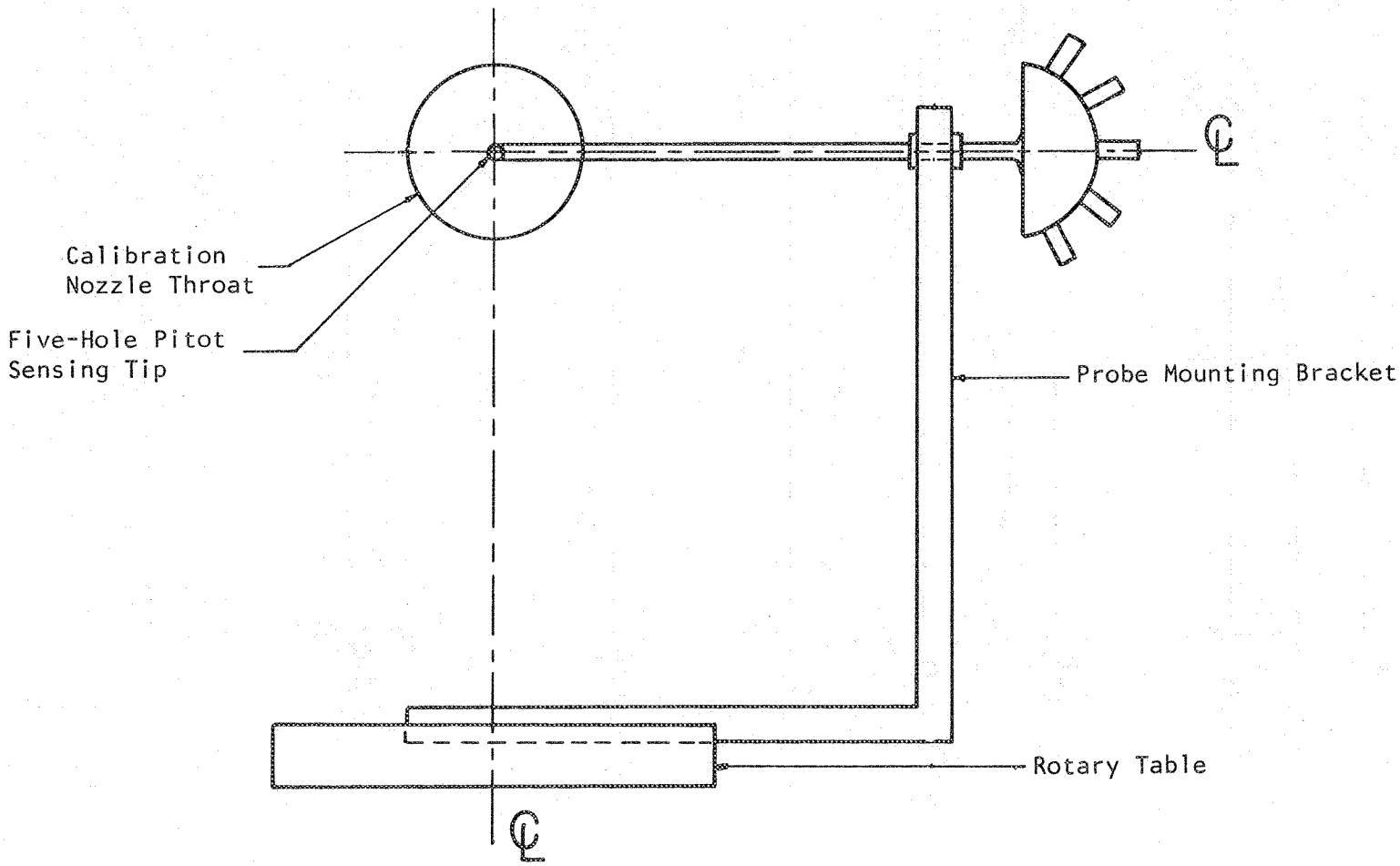

Figure 19. Calibration Apparatus With Five-Hole Pitot Probe

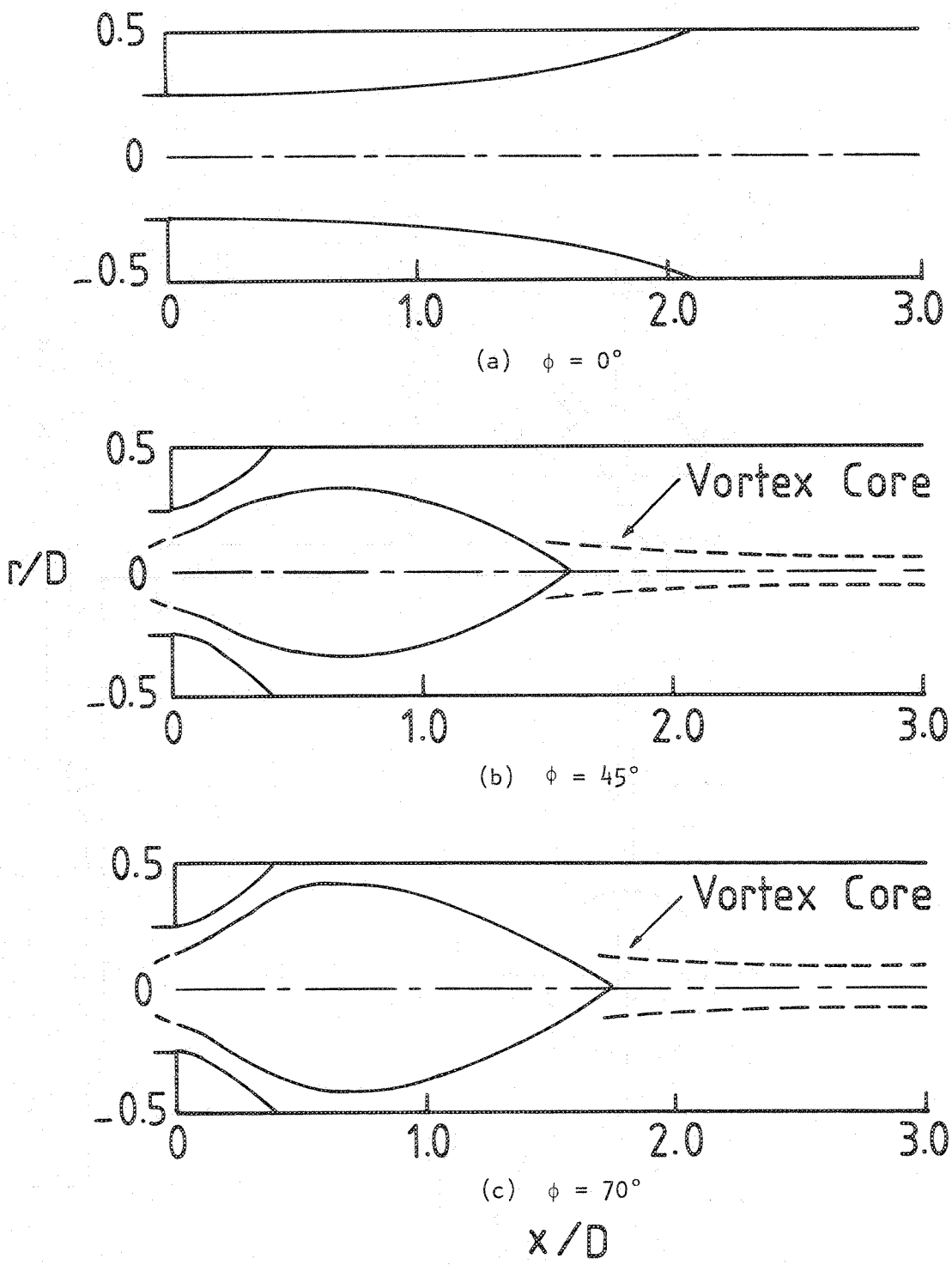

Figure 20. Artistic Impressions of Dividing Streamlines With Wall Expansion Angle $\alpha = 90°$ for Swirl Vane Angles: (a) $\phi = 0°$, (b) $\phi = 45°$, and (c) $\phi = 70°$

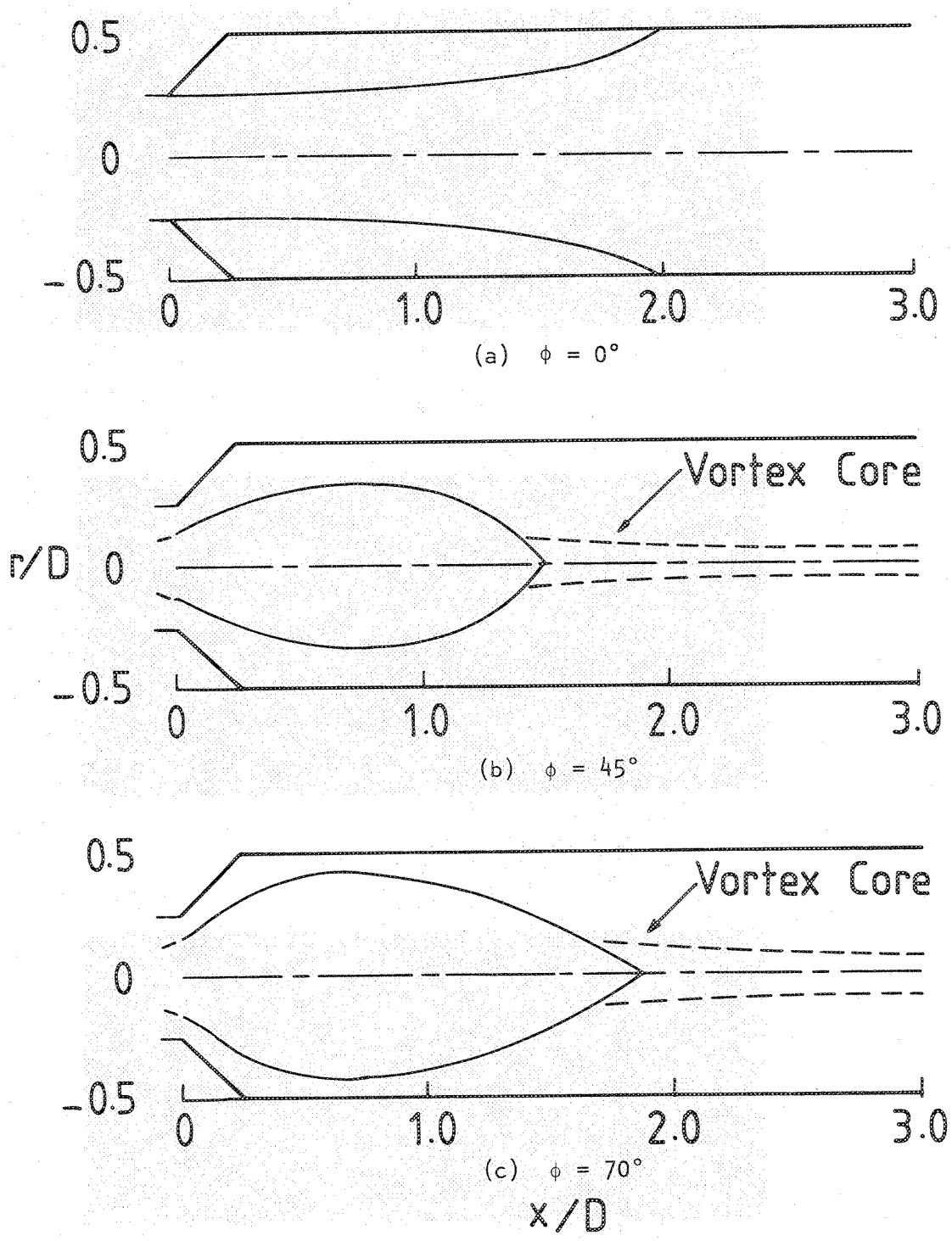

Figure 21. Artistic Impressions of Dividing Streamlines With Wall Expansion Angle α = 45° for Swirl Vane Angles: (a) ϕ = 0°, (b) ϕ = 45°, and (c) ϕ = 70°

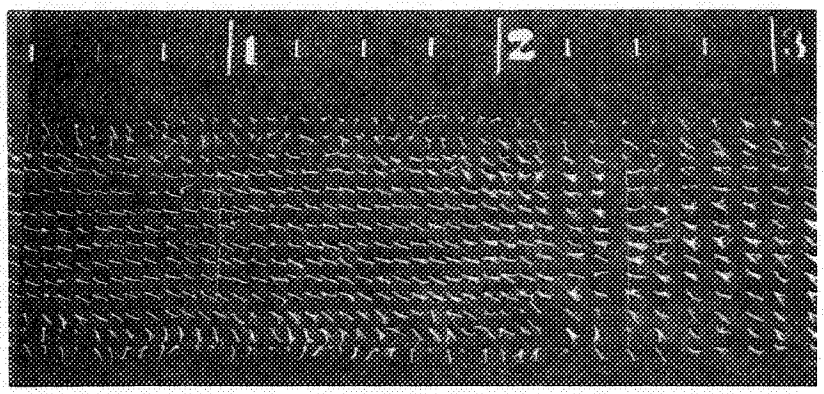

(a) $\phi = 0°$

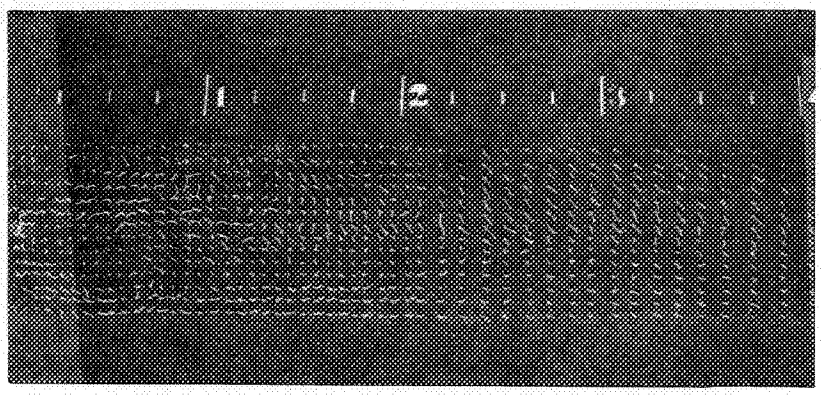

(b) $\phi = 45°$

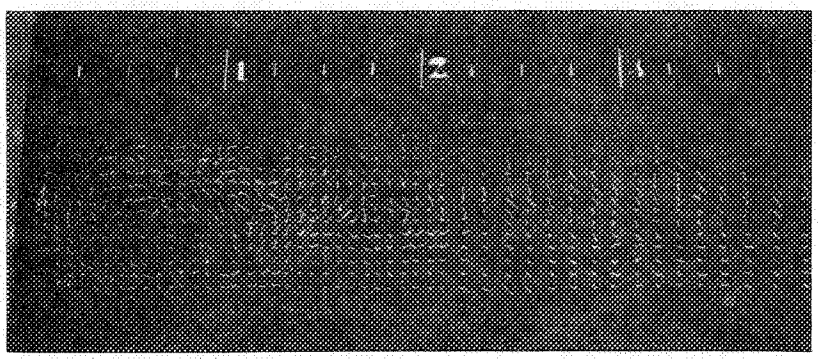

(c) $\phi = 70°$

Figure 22. Flow Visualization Photographs of Tufts in the rx-Plane With Wall Expansion Angle $\alpha = 90°$ for Swirl Vane Angles: (a) $\phi = 0°$, (b) $\phi = 45°$, and (c) $\phi = 70°$

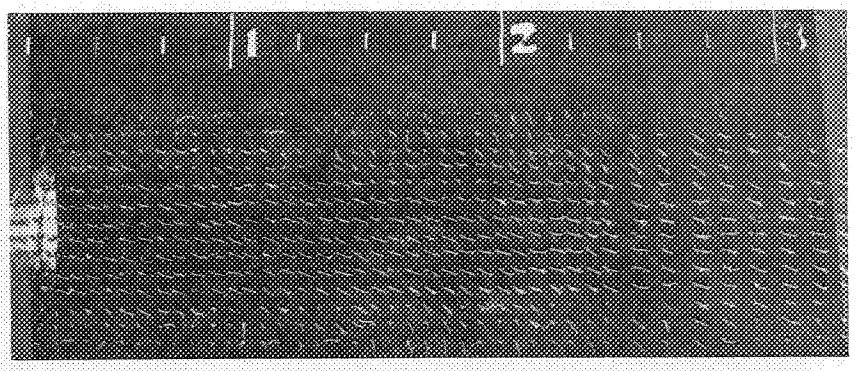

(a) $\phi = 0°$

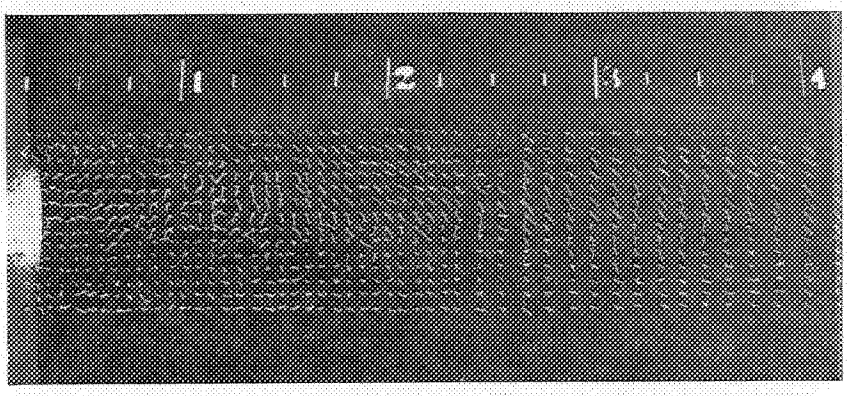

(b) $\phi = 45°$

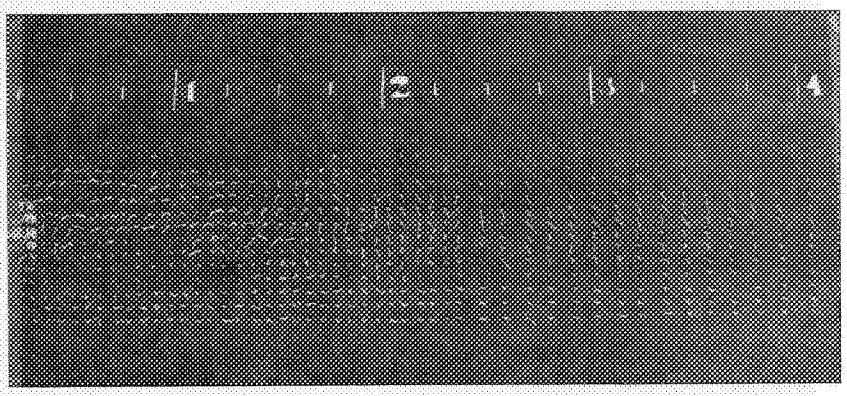

(c) $\phi = 70°$

Figure 23. Flow Visualization Photographs of Tufts in the rx-Plane With Wall Expansion Angle $\alpha = 45°$ for Swirl Vane Angles: (a) $\phi = 0°$, (b) $\phi = 45°$, and (c) $\phi = 70°$

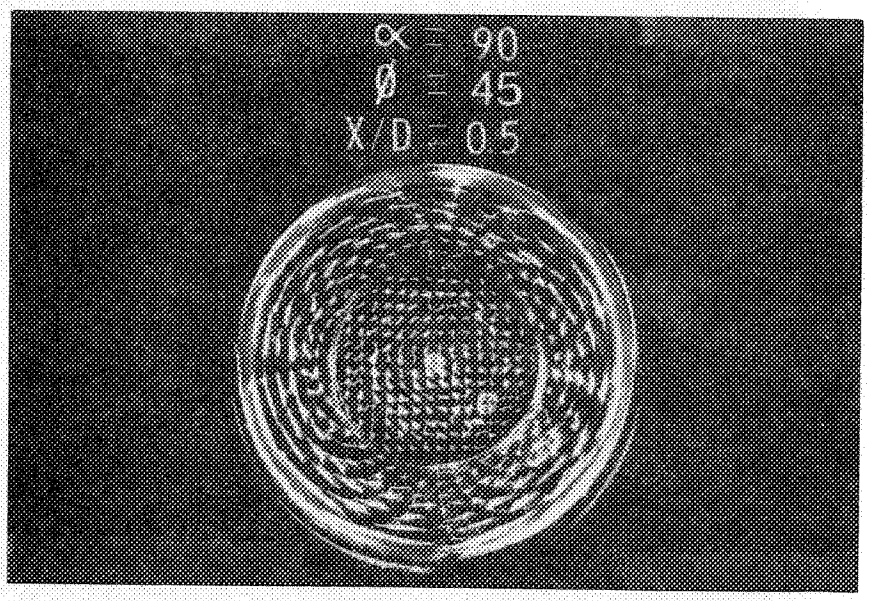

(a) x/D = 0.5

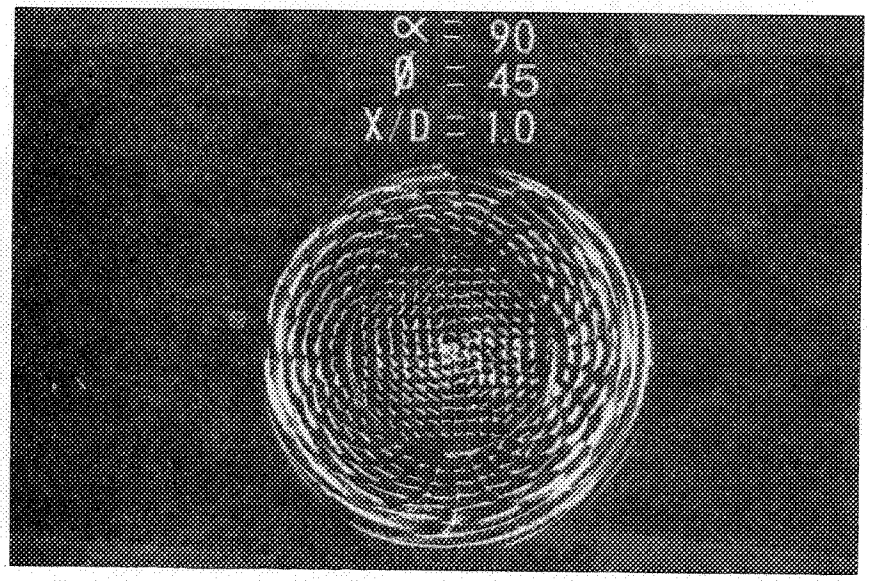

(b) x/D = 1.0

Figure 24. Flow Visualization Photographs of Smoke-Wire Streaklines With Wall Expansion Angle α = 90° for Swirl Vane Angles: (a) x/D = 0.5 and (b) x/D = 1.0

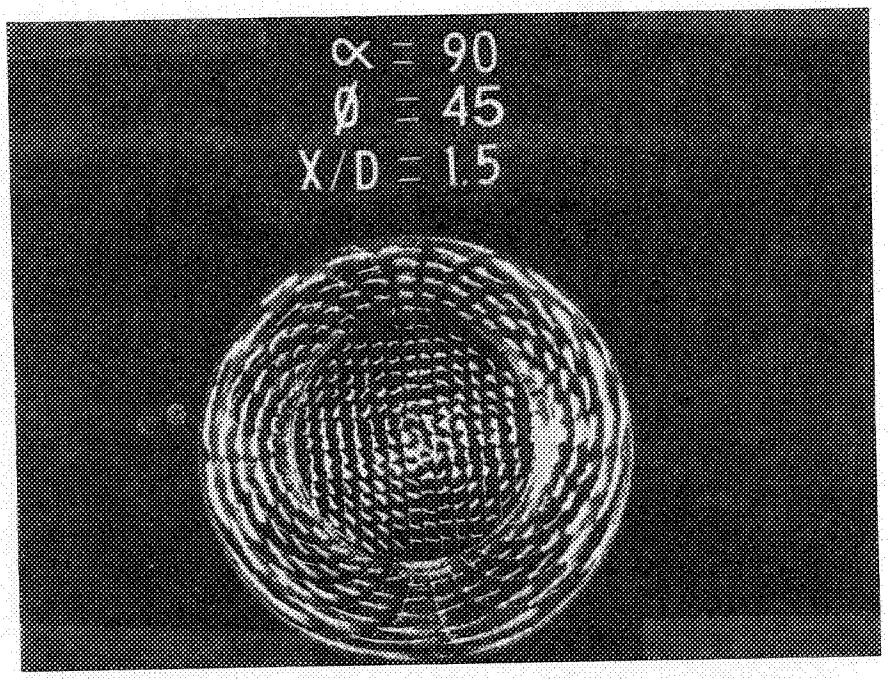

(a) x/D = 1.5

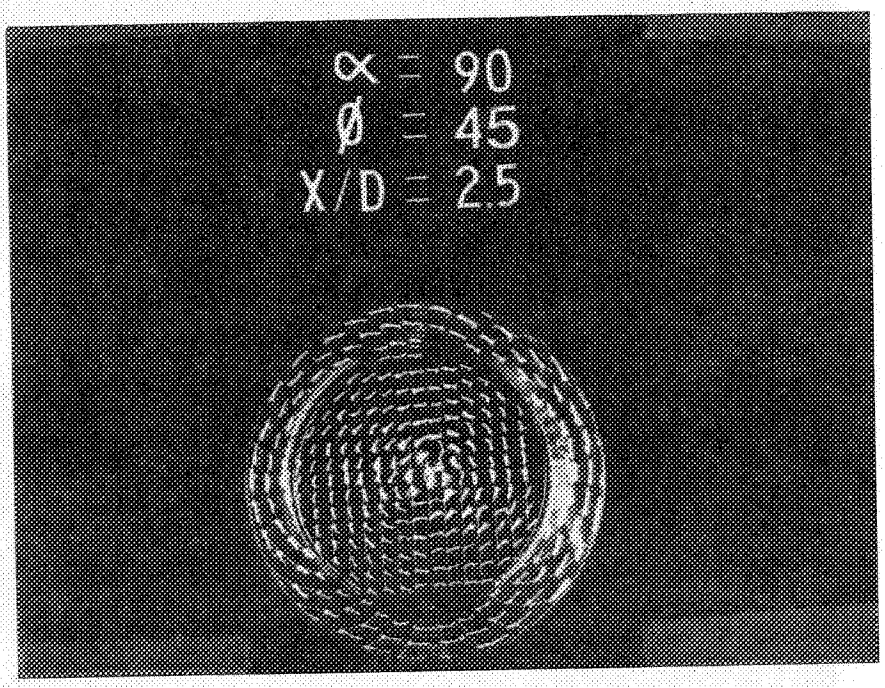

(b) x/D = 2.5

Figure 25. Flow Visualization Photographs of Tufts in the rθ-Plane With Wall Expansion Angle α = 90° and Swirl Vane Angle ϕ = 45° for Axial Stations: (a) x/D = 1.5 and (b) x/D = 2.5

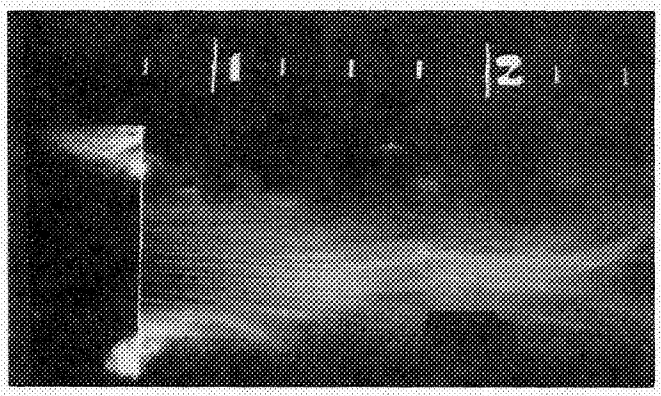

(a) $\phi = 0°$

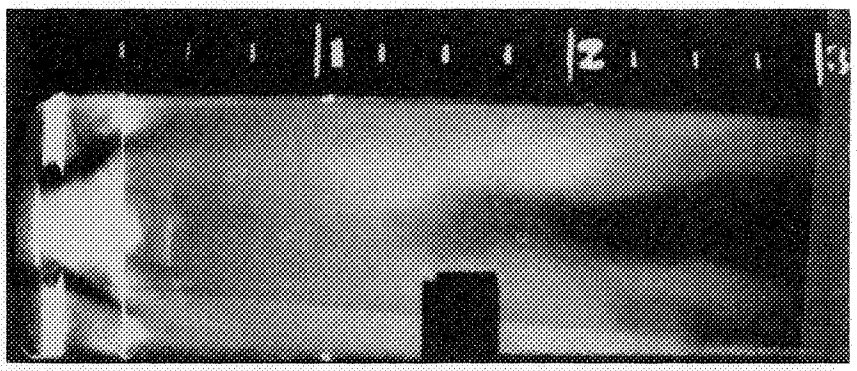

(b) $\phi = 45°$

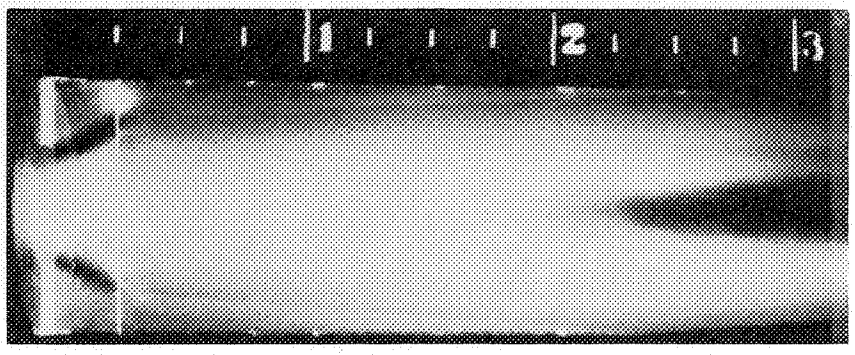

(c) $\phi = 70°$

Figure 26. Flow Visualization Photographs of Smoke-Wire Streaklines With Wall Expansion Angle $\alpha = 90°$ for Swirl Vane Angles: (a) $\phi = 0°$, (b) $\phi = 45°$, and (c) $\phi = 70°$

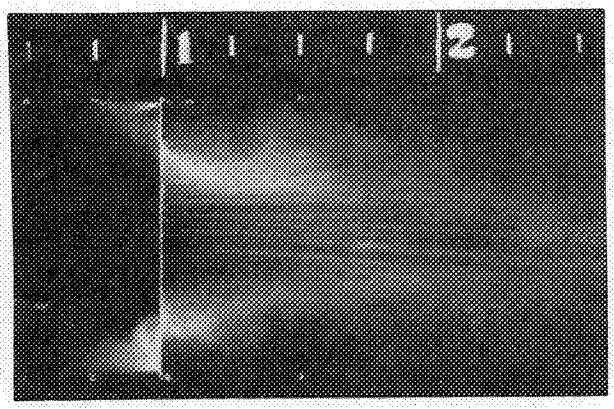

(a) $\phi = 0°$

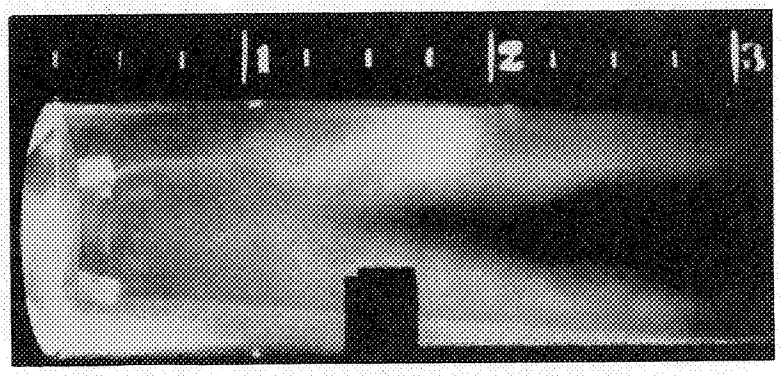

(b) $\phi = 45°$

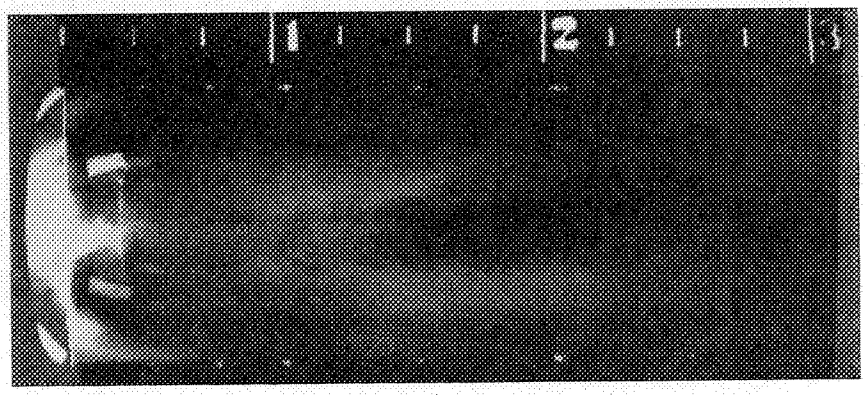

(c) $\phi = 70°$

Figure 27. Flow Visualization Photographs of Smoke-Wire Streaklines With Wall Expansion Angle $\alpha = 45°$ for Swirl Vane Angles: (a) $\phi = 0°$, (b) $\phi = 45°$, and (c) $\phi = 70°$

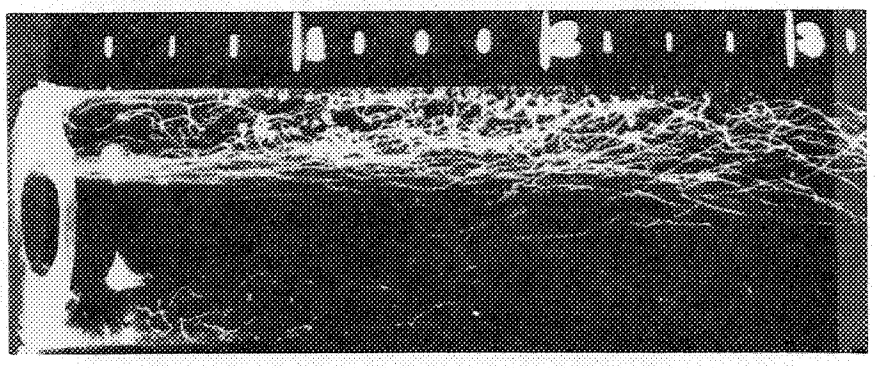

(a) $\phi = 0°$

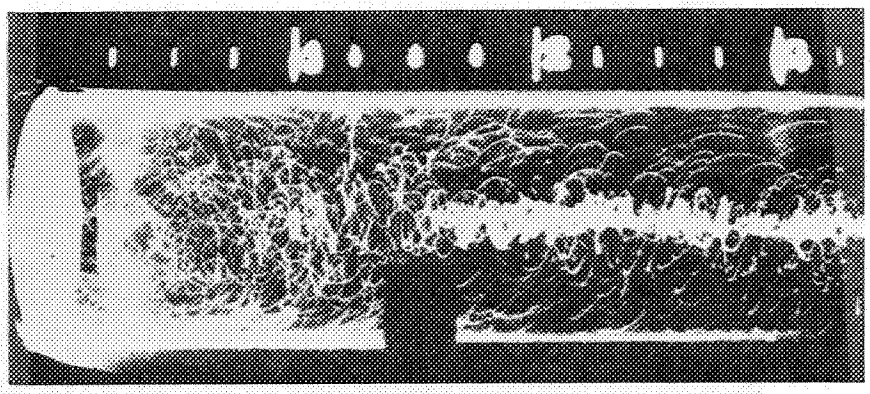

(b) $\phi = 45°$

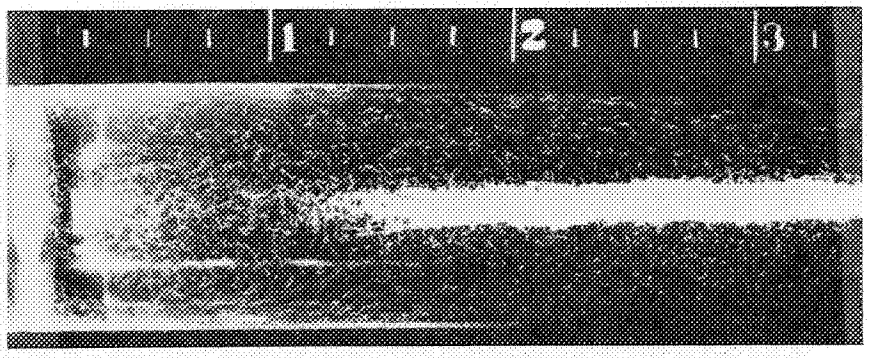

(c) $\phi = 70°$

Figure 28. Flow Visualization Photographs of Pathlines Indicated by Illuminated Neutrally-Buoyant Soap Bubbles for Wall Expansion Angle α = 90° and Swirl Vane Angles: (a) $\phi = 0°$, (b) $\phi = 45°$, and (c) $\phi = 70°$

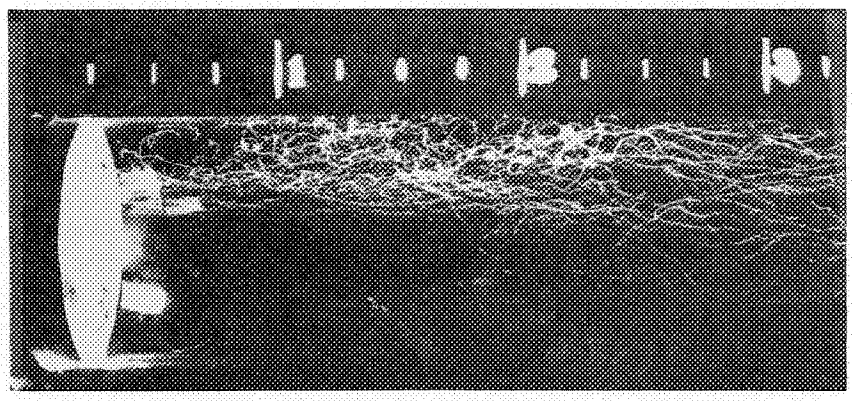

(a) $\phi = 0°$

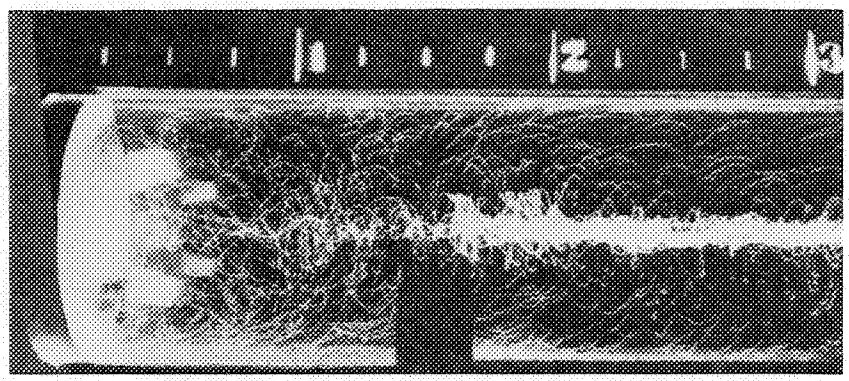

(b) $\phi = 45°$

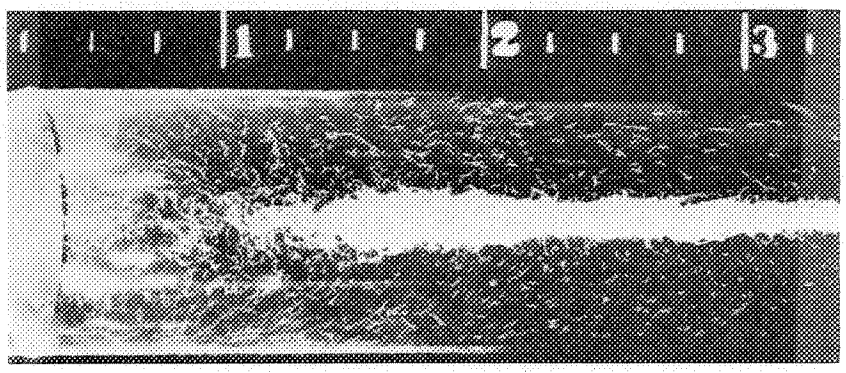

(c) $\phi = 70°$

Figure 29. Flow Visualization Photographs of Path-lines Indicated by Illuminated Neutrally-Buoyant Soap Bubbles for Wall Expansion Angle $\alpha = 45°$ and Swirl Vane Angles: (a) $\phi = 0°$, (b) $\phi = 45°$, and (c) $\phi = 70°$

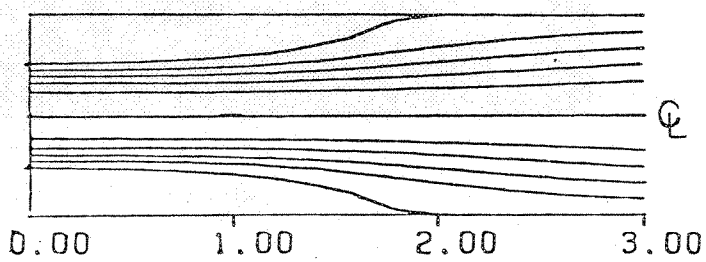

(a) $\phi = 0°$

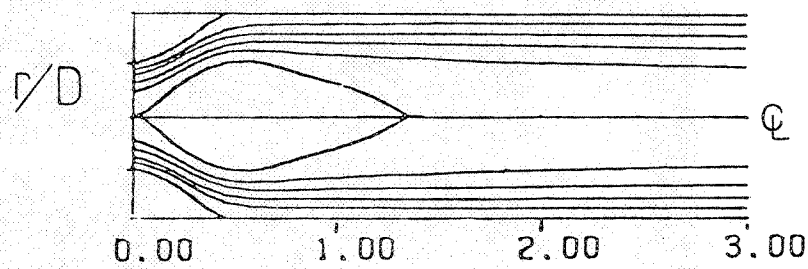

(b) $\phi = 45°$

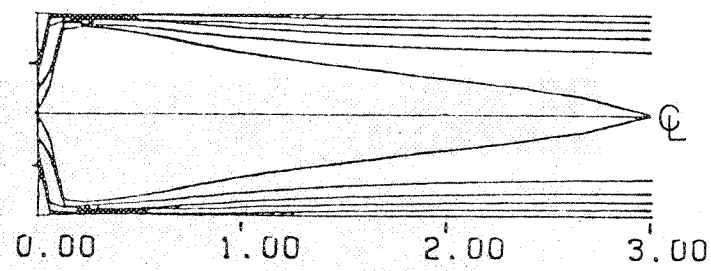

(c) $\phi = 70°$

Axial Position x/D

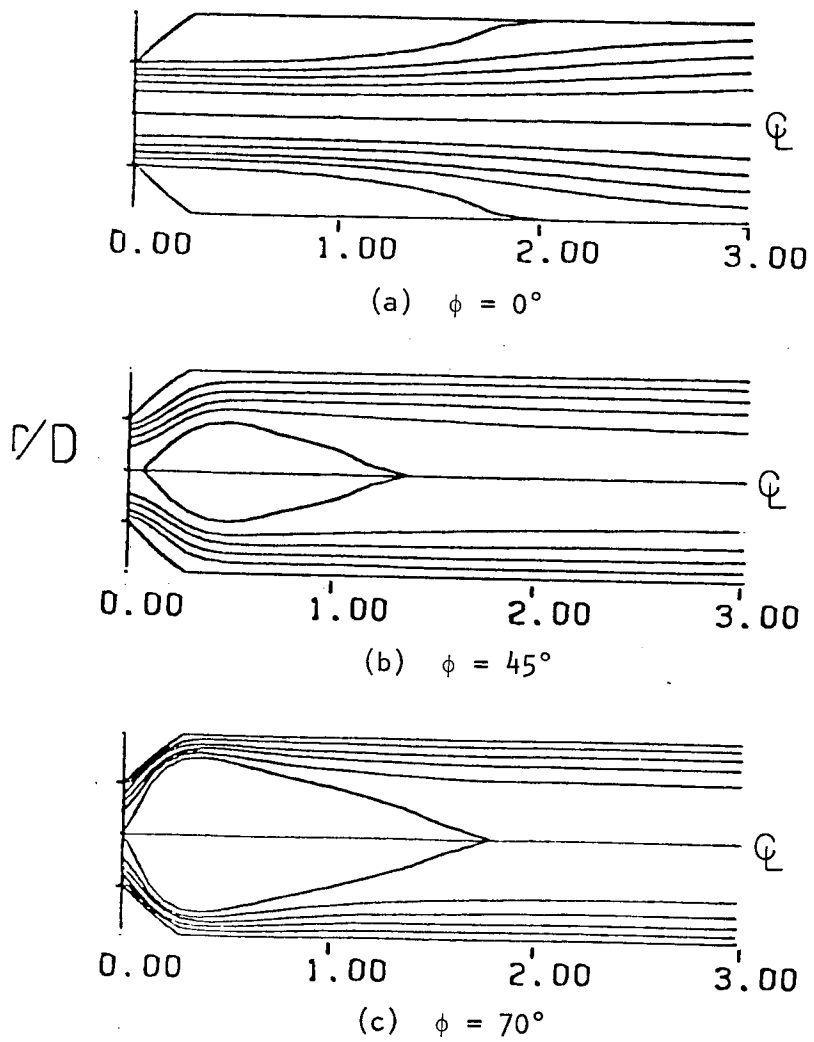
℄
0.00
1.00
2.00
3.00
(a) ϕ = 0°
r/D
℄
0.00
1.00
2.00
3.00
(b) ϕ = 45°
℄
0.00
1.00
2.00
3.00
(c) ϕ = 70°
Axial Position x/D

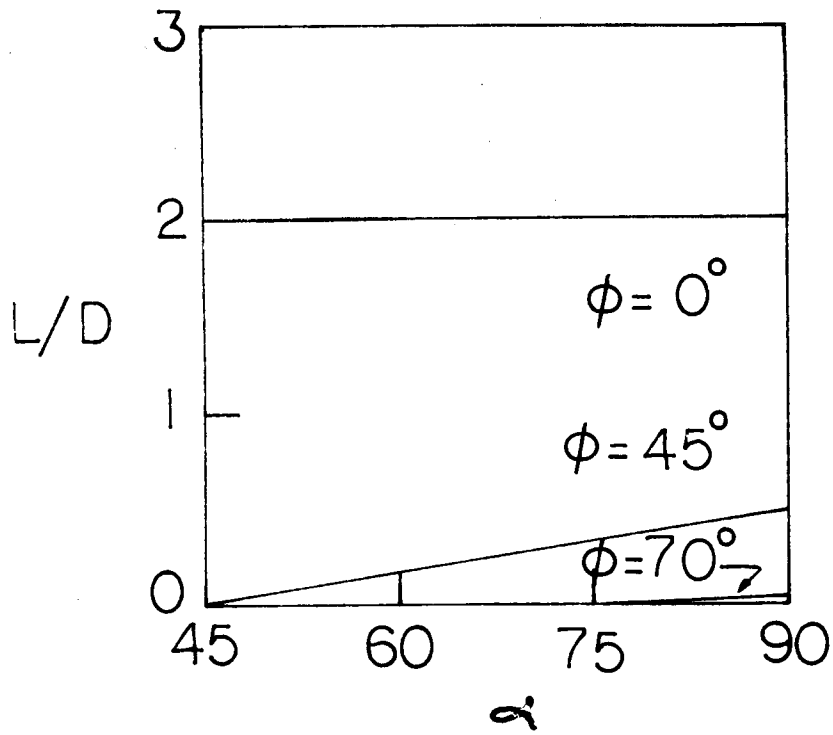

(a) Corner Recirculation Zone

Figure 32. Predicted Effect of Wall Expansion Angle α and Swirl Vane Angle ϕ on: (a) Corner Recirculation Zone Length and (b) Central Toroidal Recirculation Zone Length

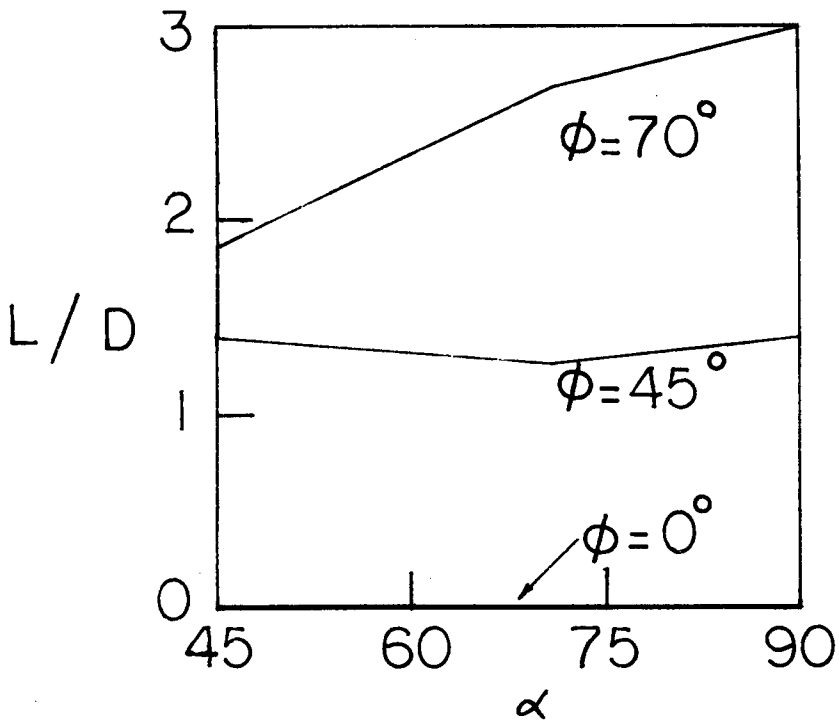

(b) Central Toroidal Recirculation Zone

Figure 32. (Continued)

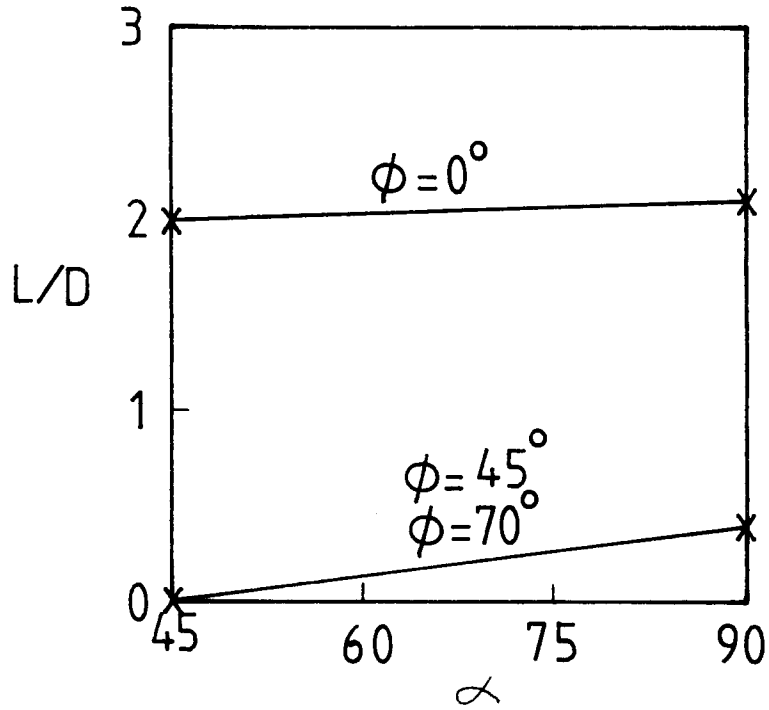

(a) Corner Recirculation Zone

Figure 33. Experimental Effect of Wall Expansion Angle α and Swirl Vane Angle ϕ on: (a) Corner Recirculation Zone Length and (b) Central Toroidal Recirculation Zone Length

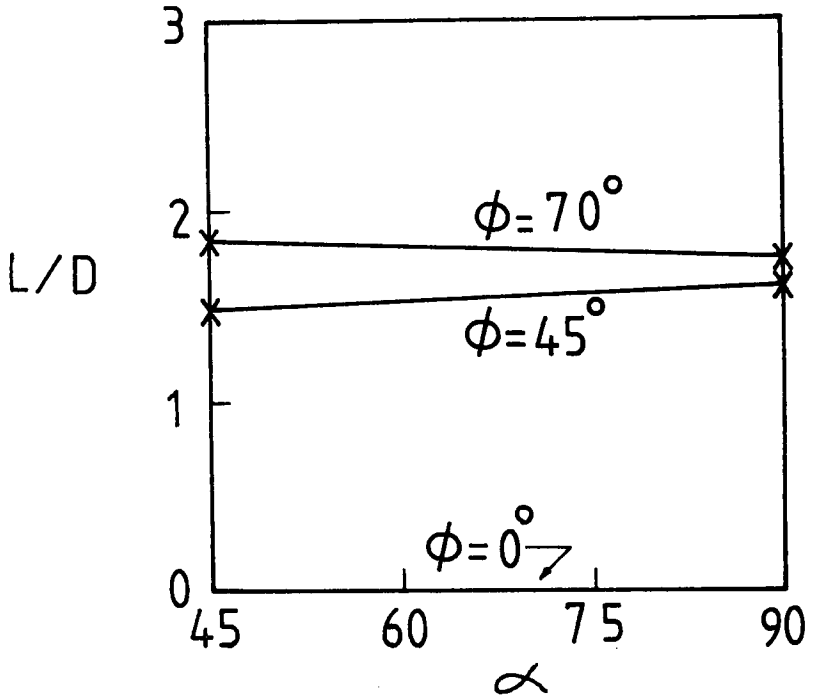

(b) Central Toroidal Recirculation Zone

Figure 33. (Continued)

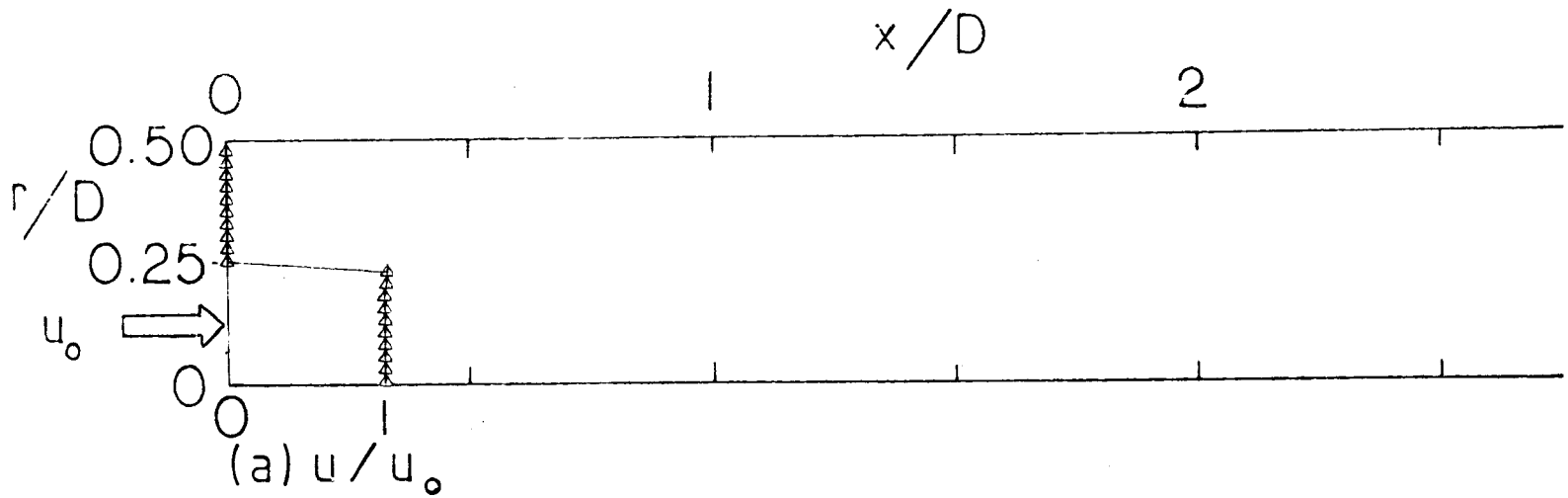

Figure 34. Measured Velocity Profiles for Wall Expansion Angle α = 90° and Swirl Vane Angle ϕ = 0°

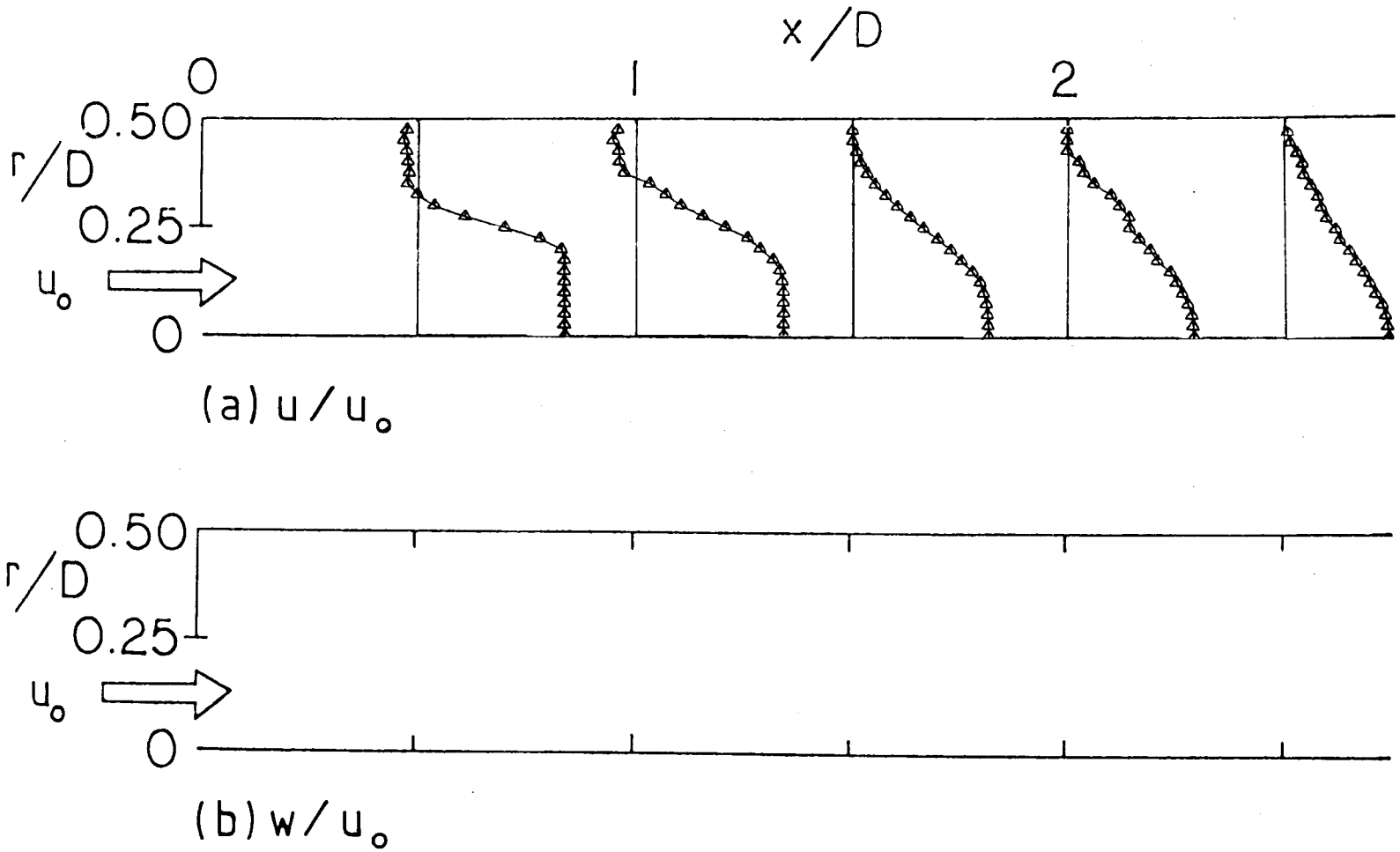

Figure 34. (Continued)

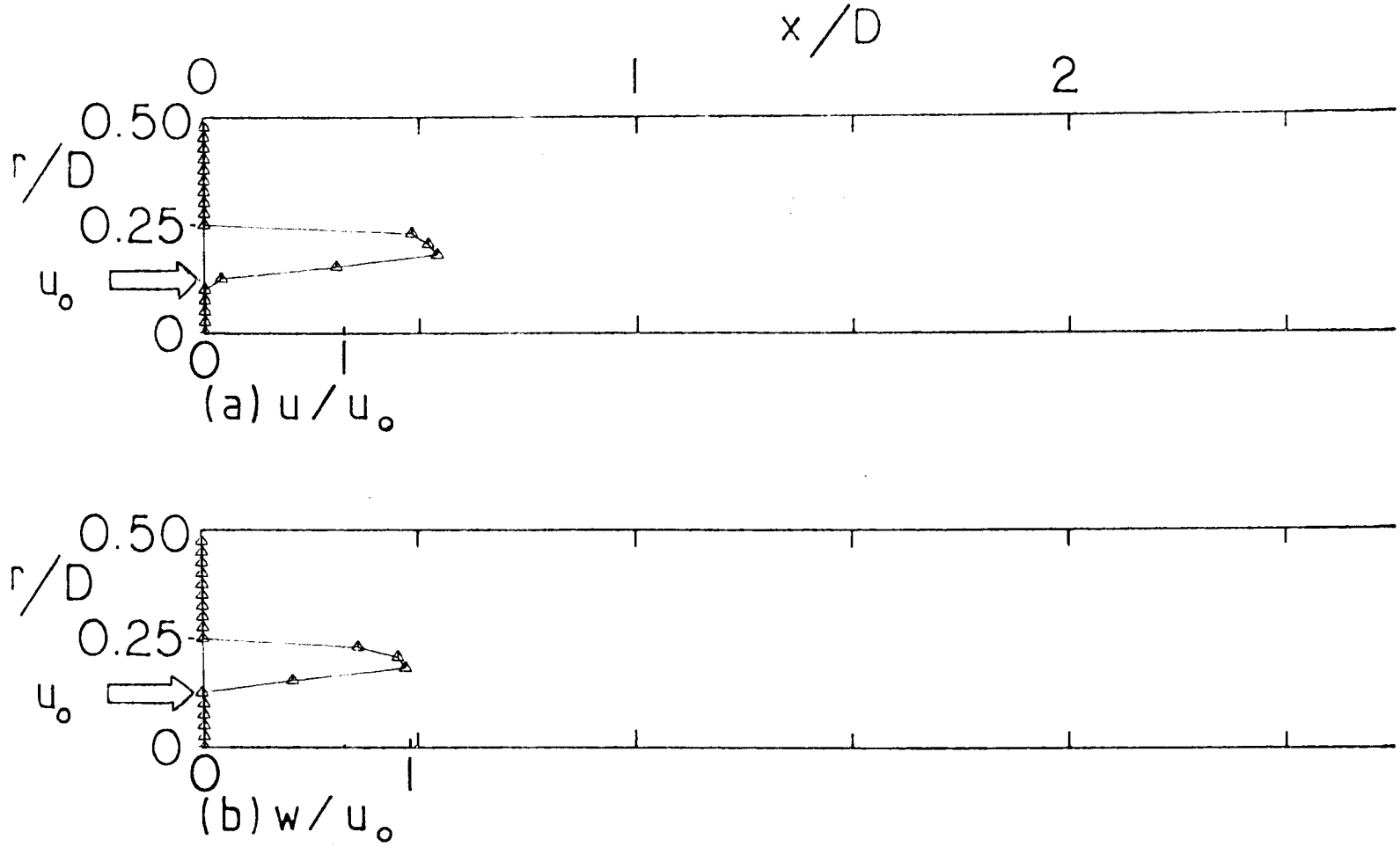

Figure 35. Measured Velocity Profiles for Wall Expansion Angle α = 90° and Swirl Vane Angle ϕ = 45°

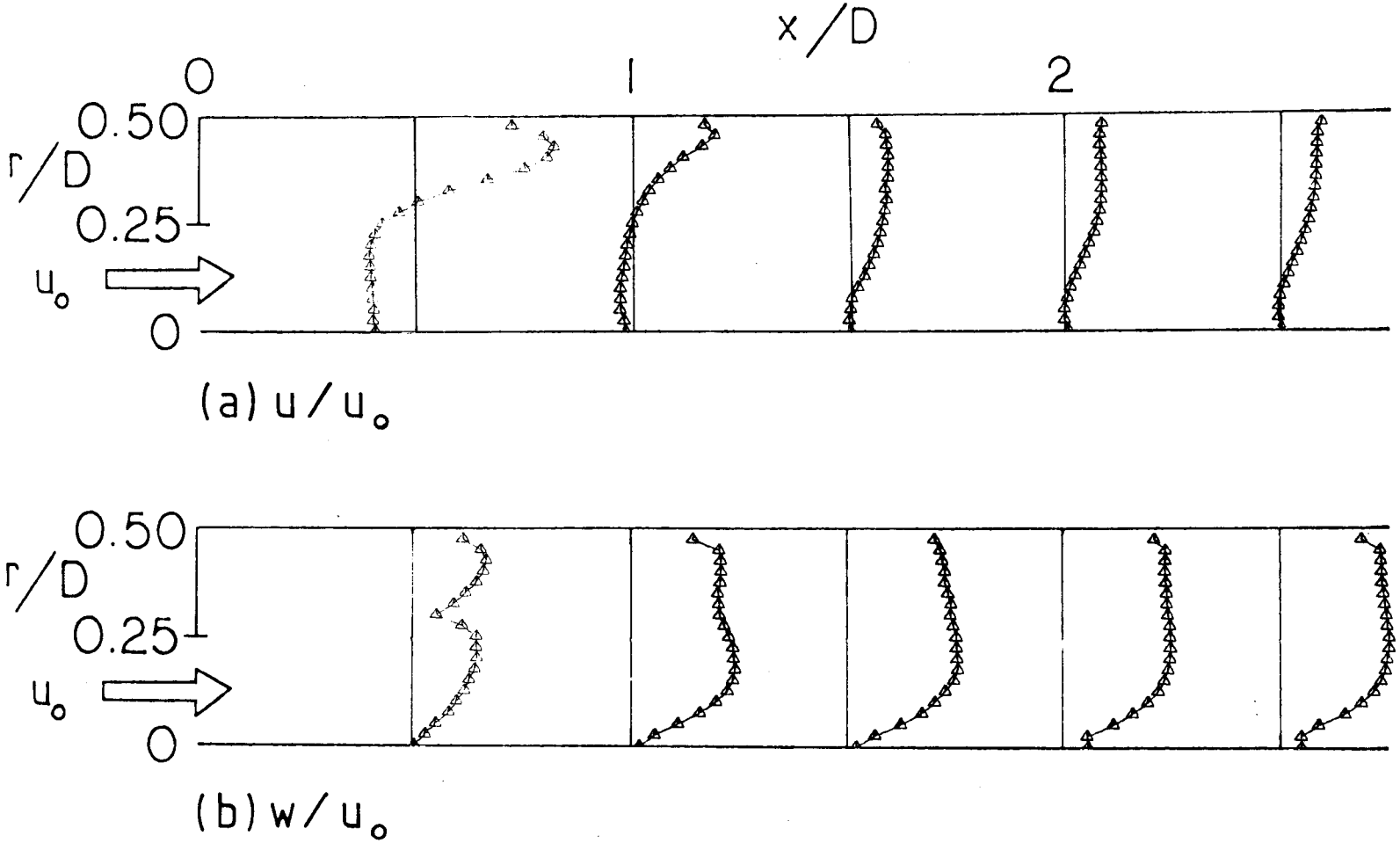

Figure 35. (Continued)

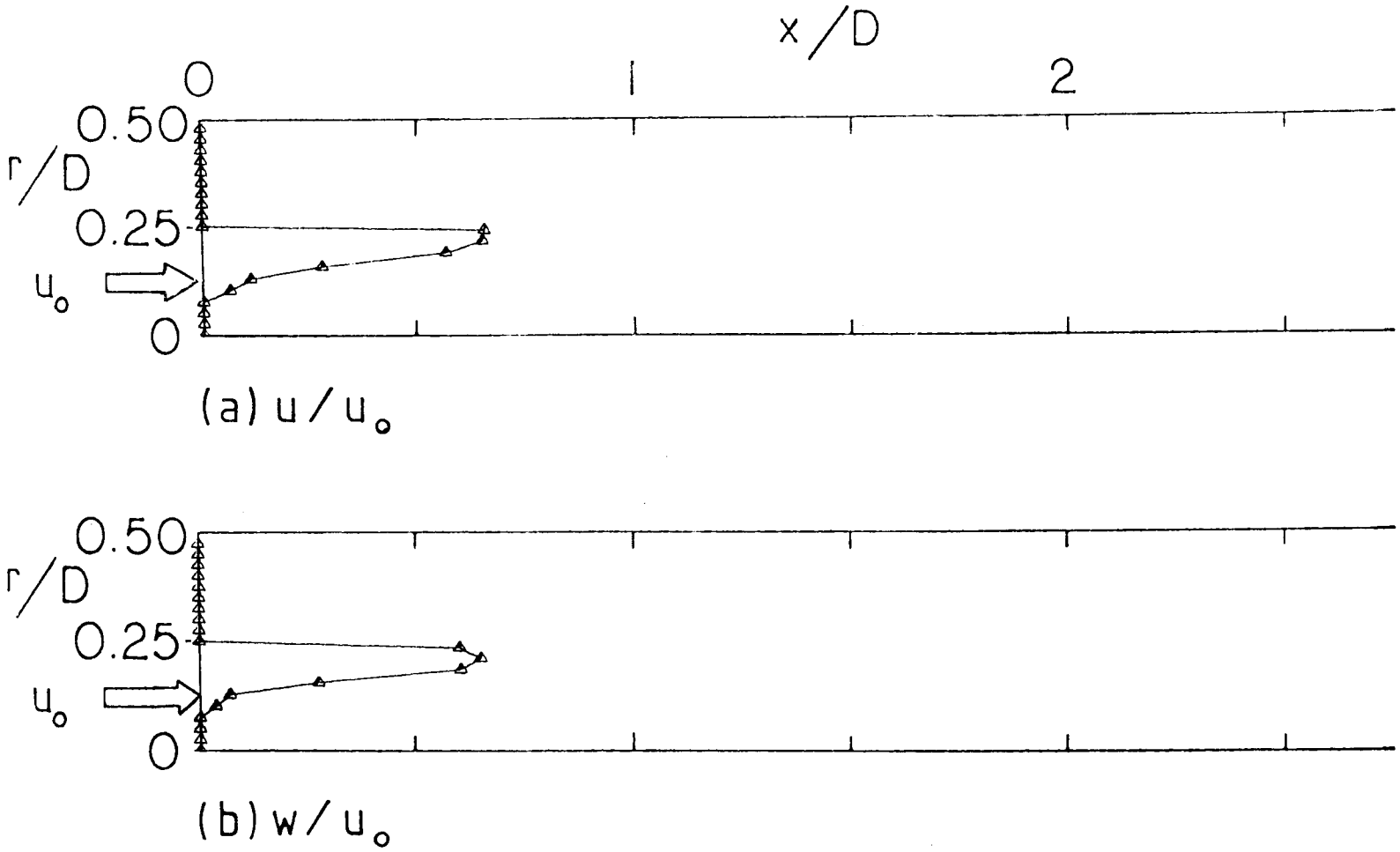

Figure 36. Measured Velocity Profiles for Wall Expansion Angle $\alpha = 90°$ and Swirl Vane Angle $\phi = 70°$

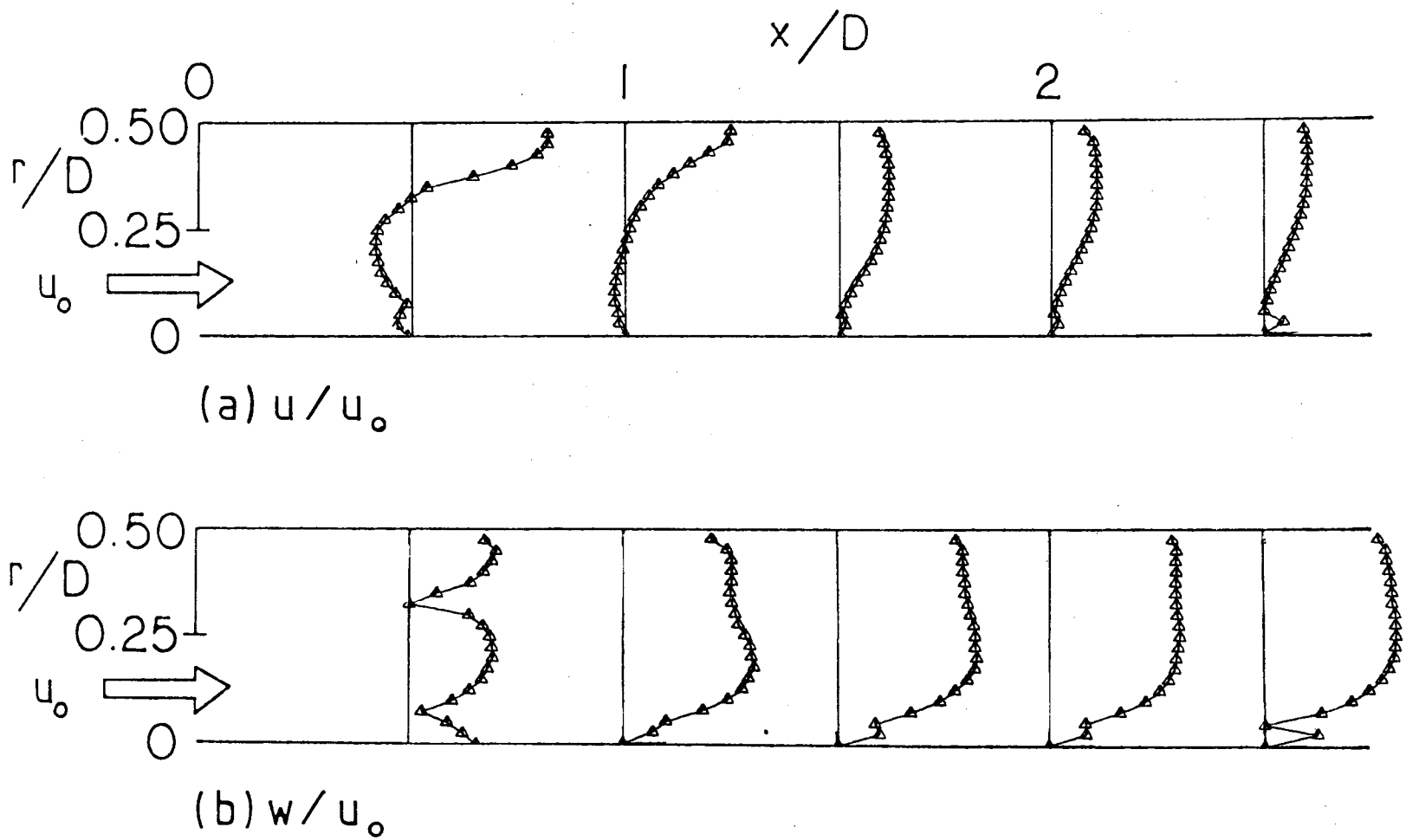

Figure 36. (Continued)

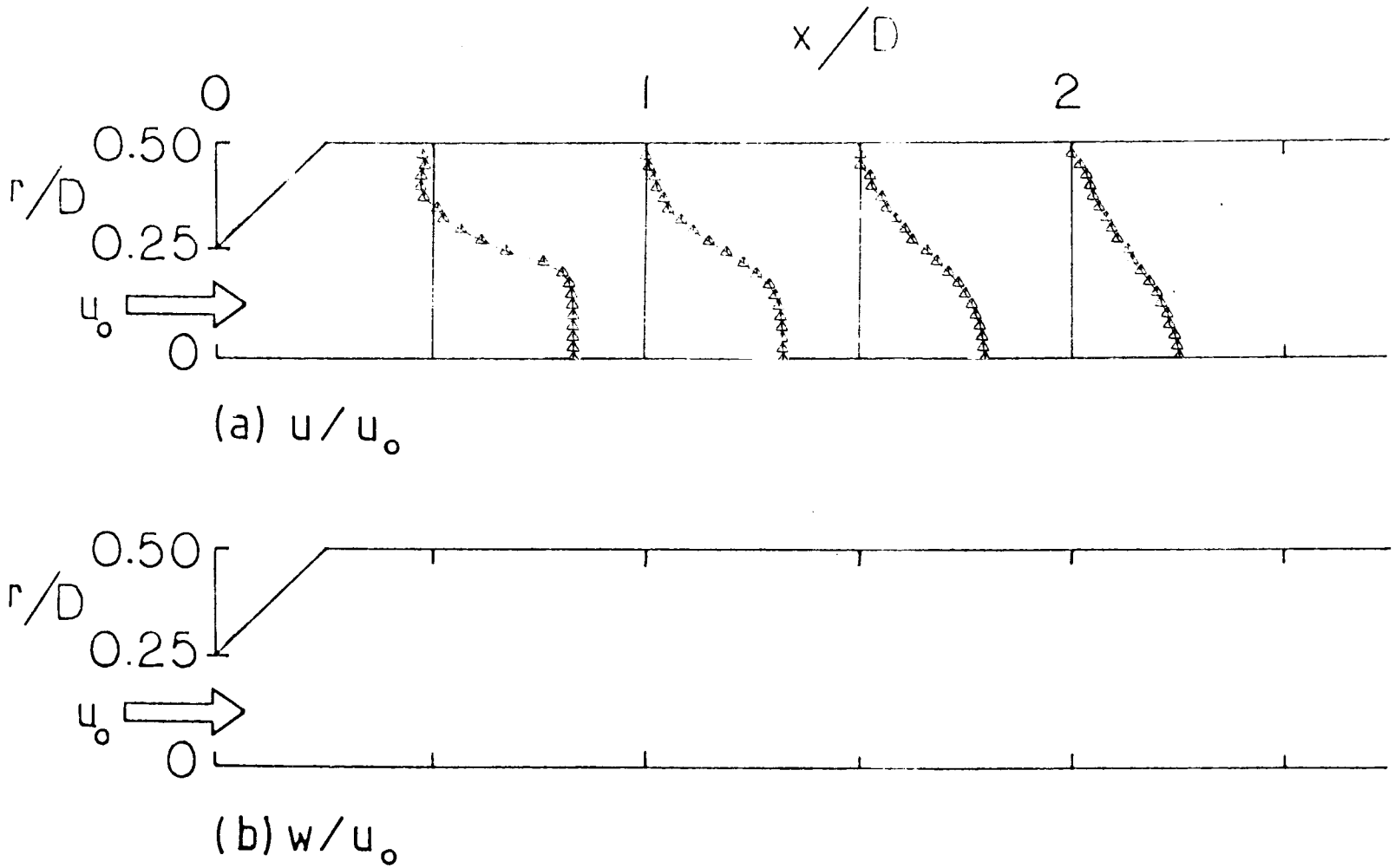

Figure 37. Measured Velocity Profiles for Wall Expansion Angle $\alpha = 45°$ and Swirl Vane Angle $\phi = 0°$

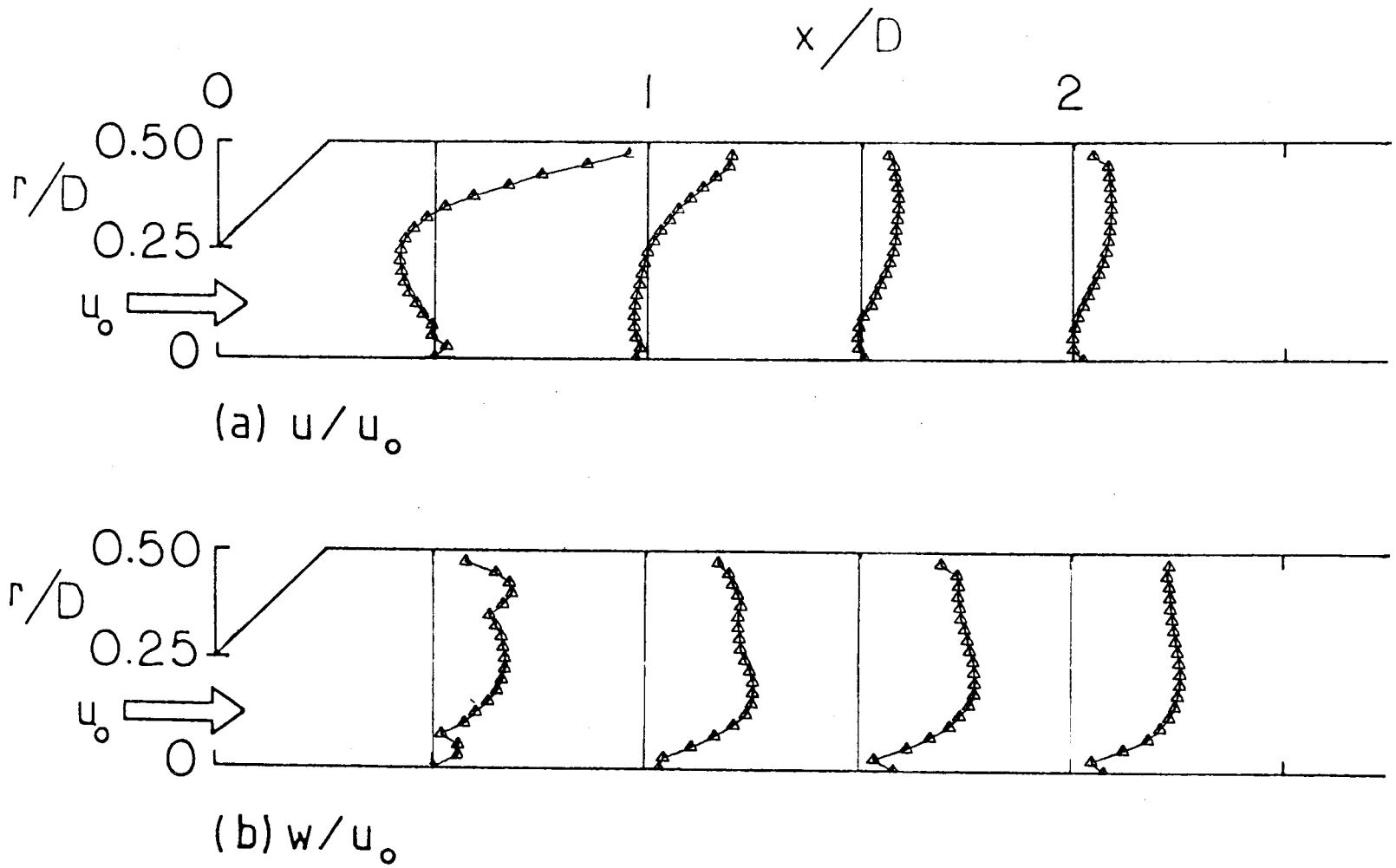

Figure 38. Measured Velocity Profiles for Wall Expansion Angle $\alpha = 45°$ and Swirl Vane Angle $\phi = 45°$

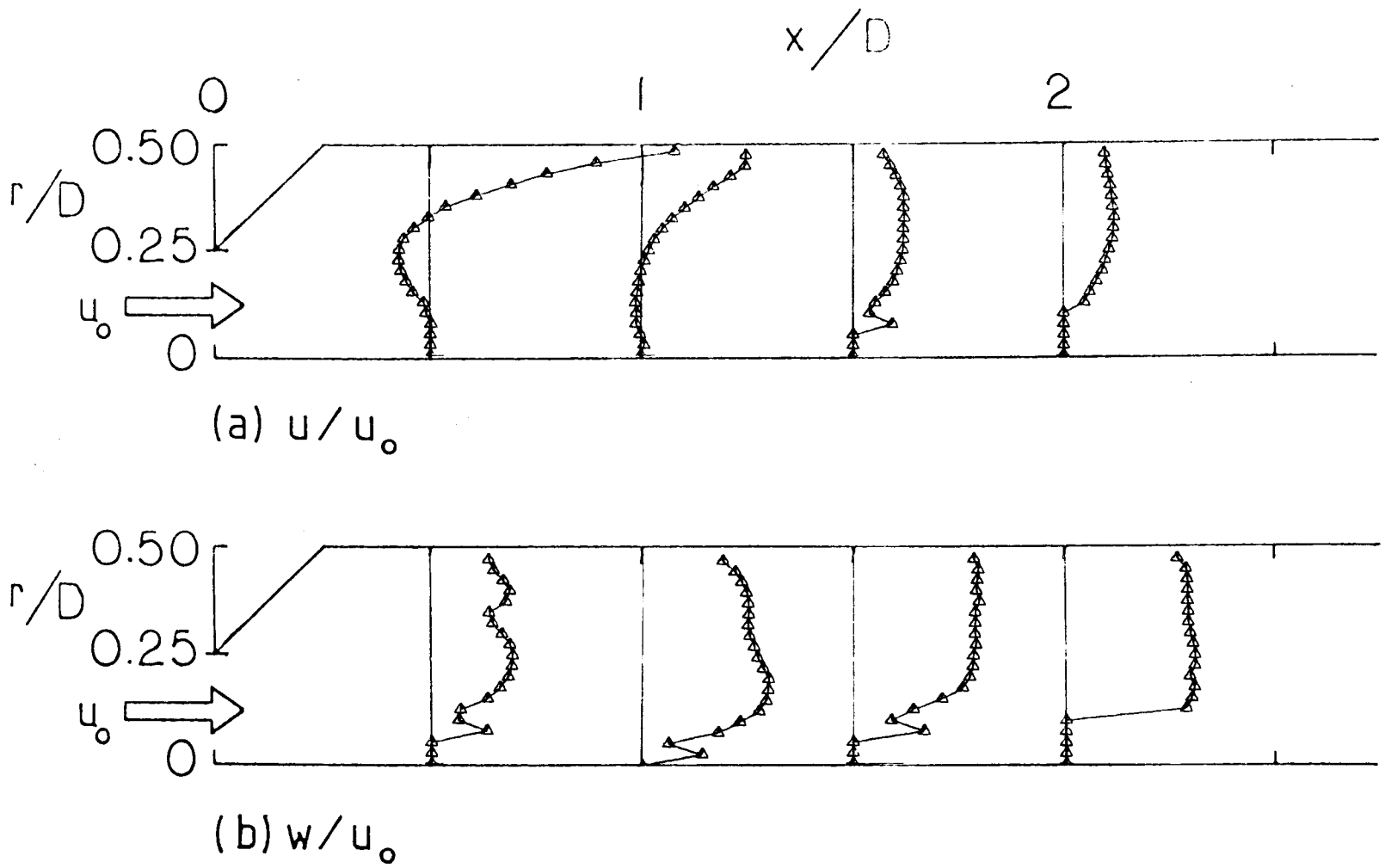

Figure 39. Measured Velocity Profiles for Wall Expansion Angle $\alpha = 45°$ and Swirl Vane Angle $\phi = 70°$

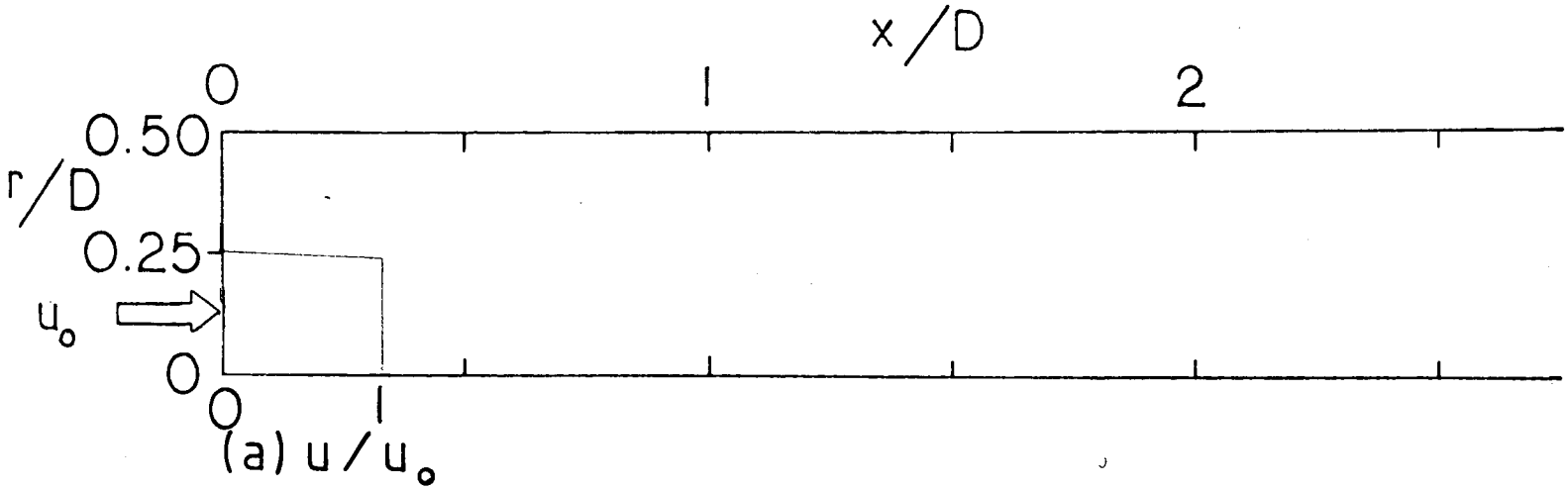

Figure 40. Predicted Velocity Profiles for Wall Expansion Angle $\alpha = 90°$ and Swirl Vane Angle $\phi = 0°$

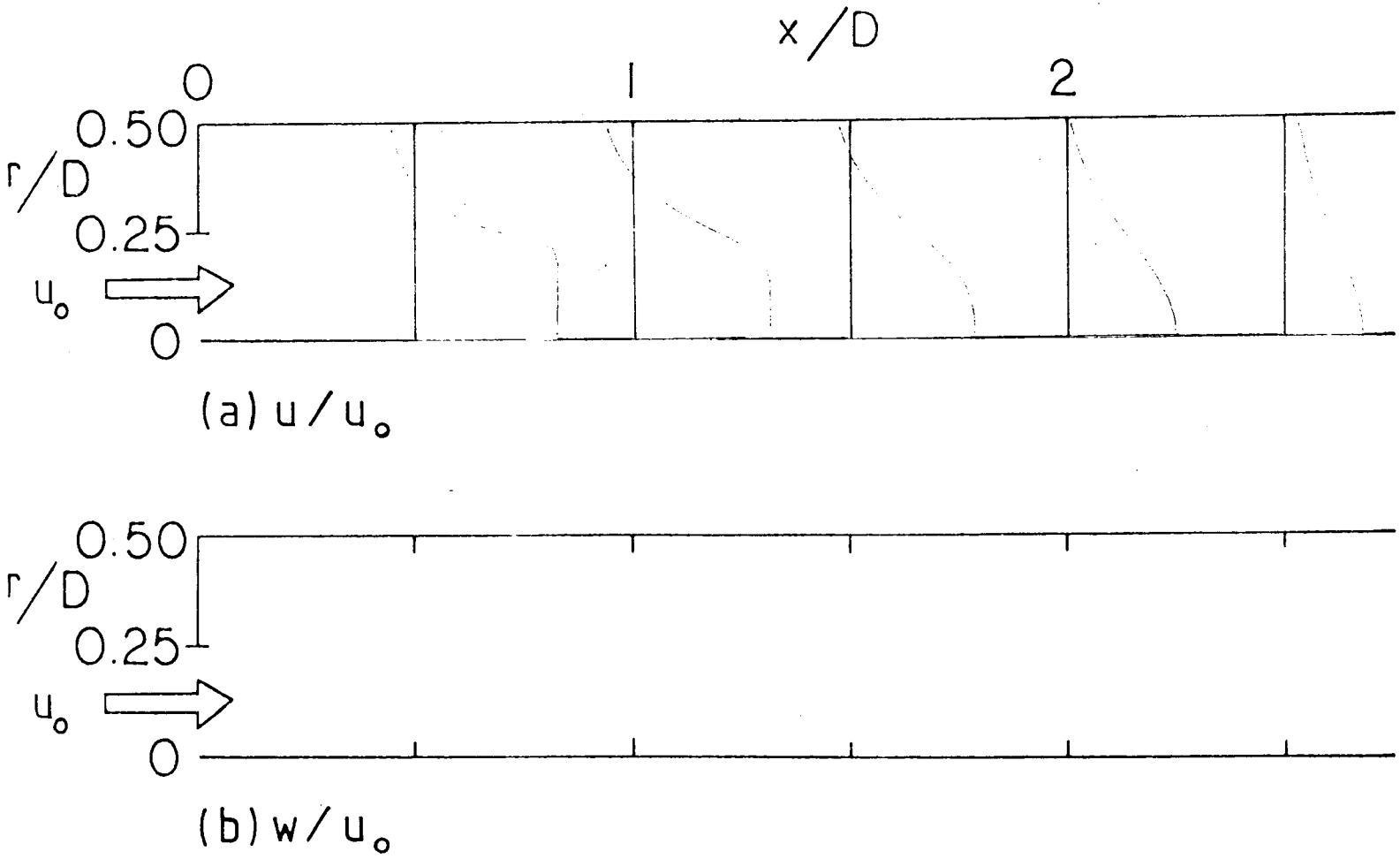

Figure 40. (Continued)

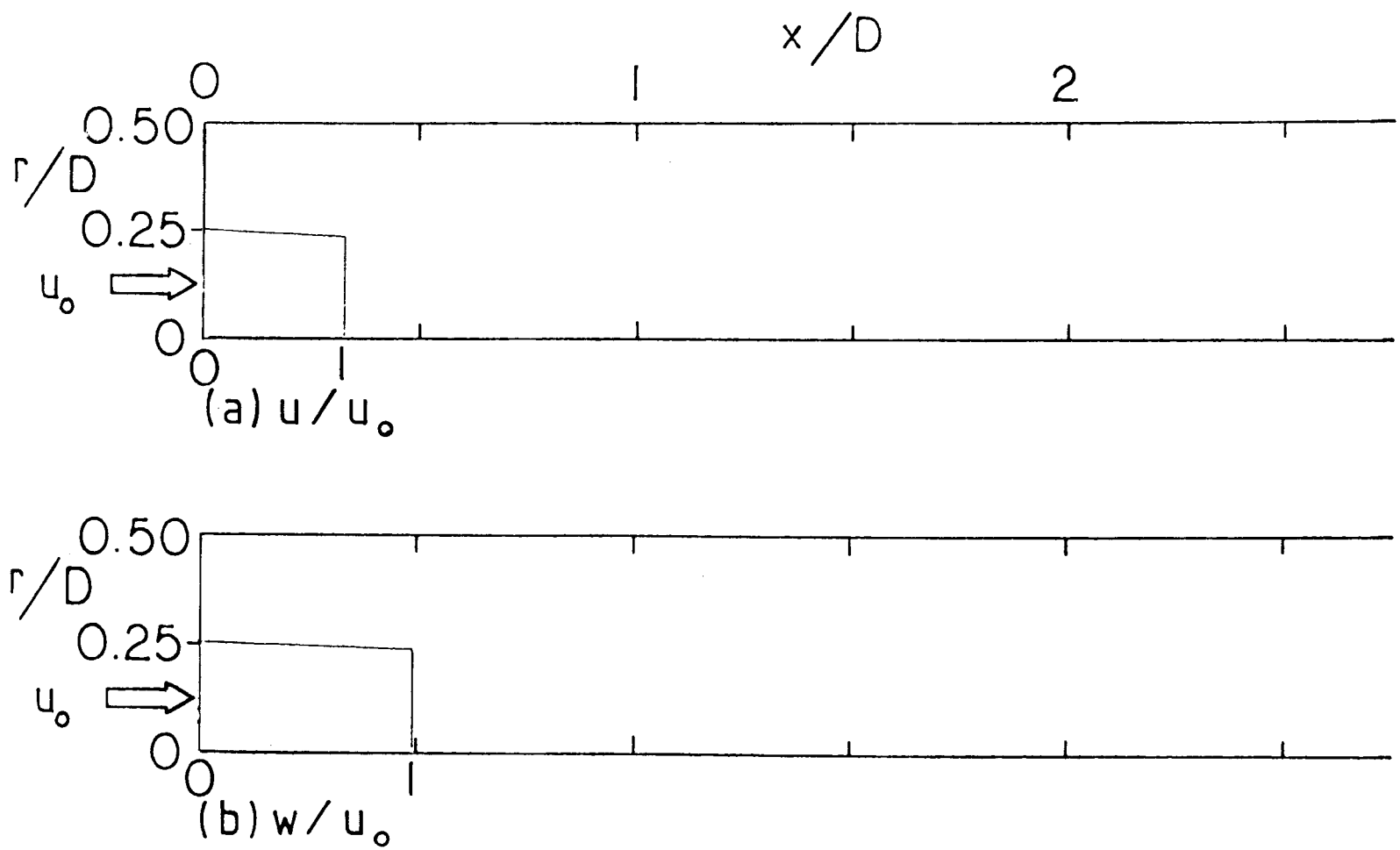

Figure 41. Predicted Velocity Profiles for Wall Expansion Angle $\alpha = 90°$ and Swirl Vane Angle $\phi = 45°$

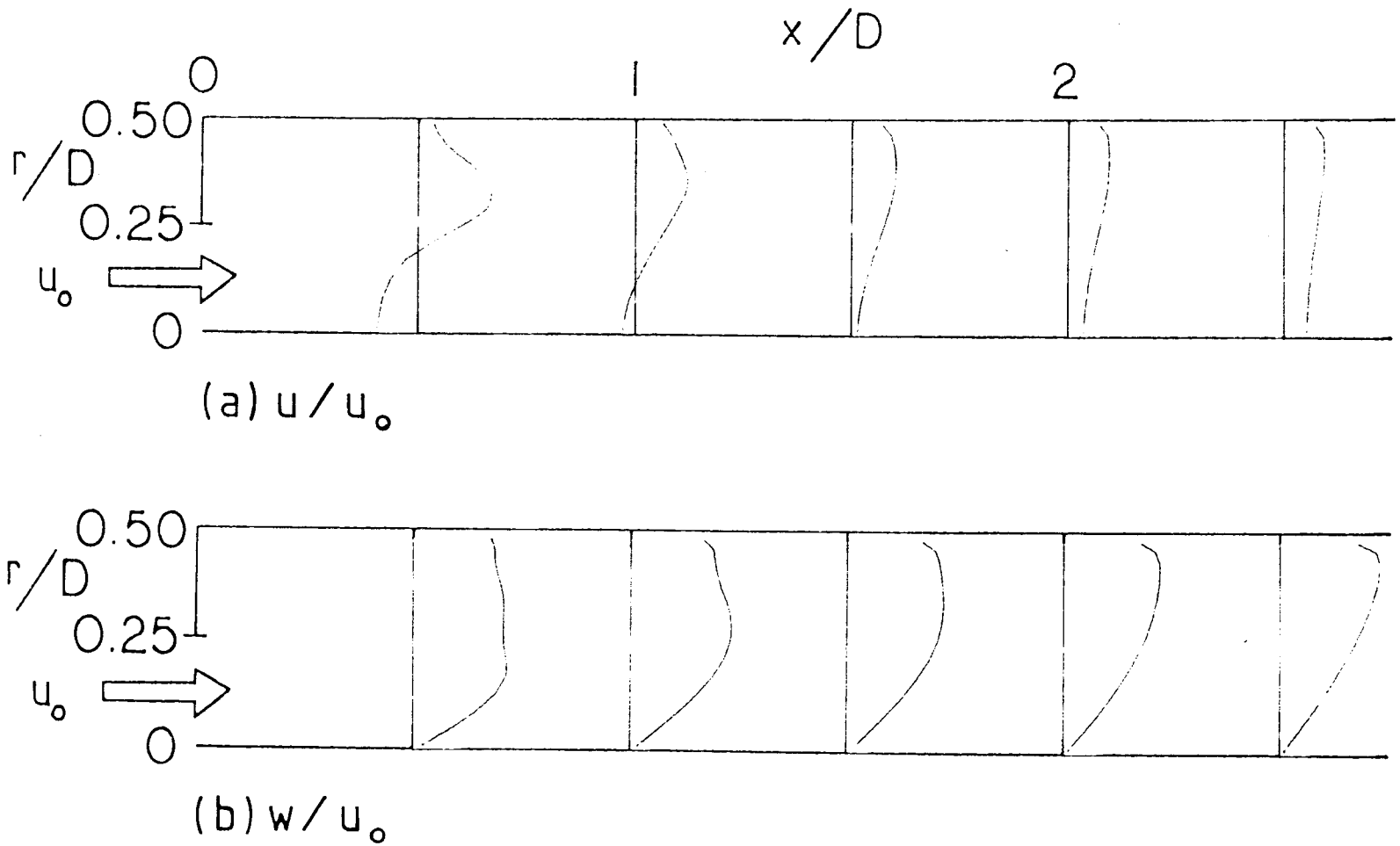

Figure 41. (Continued)

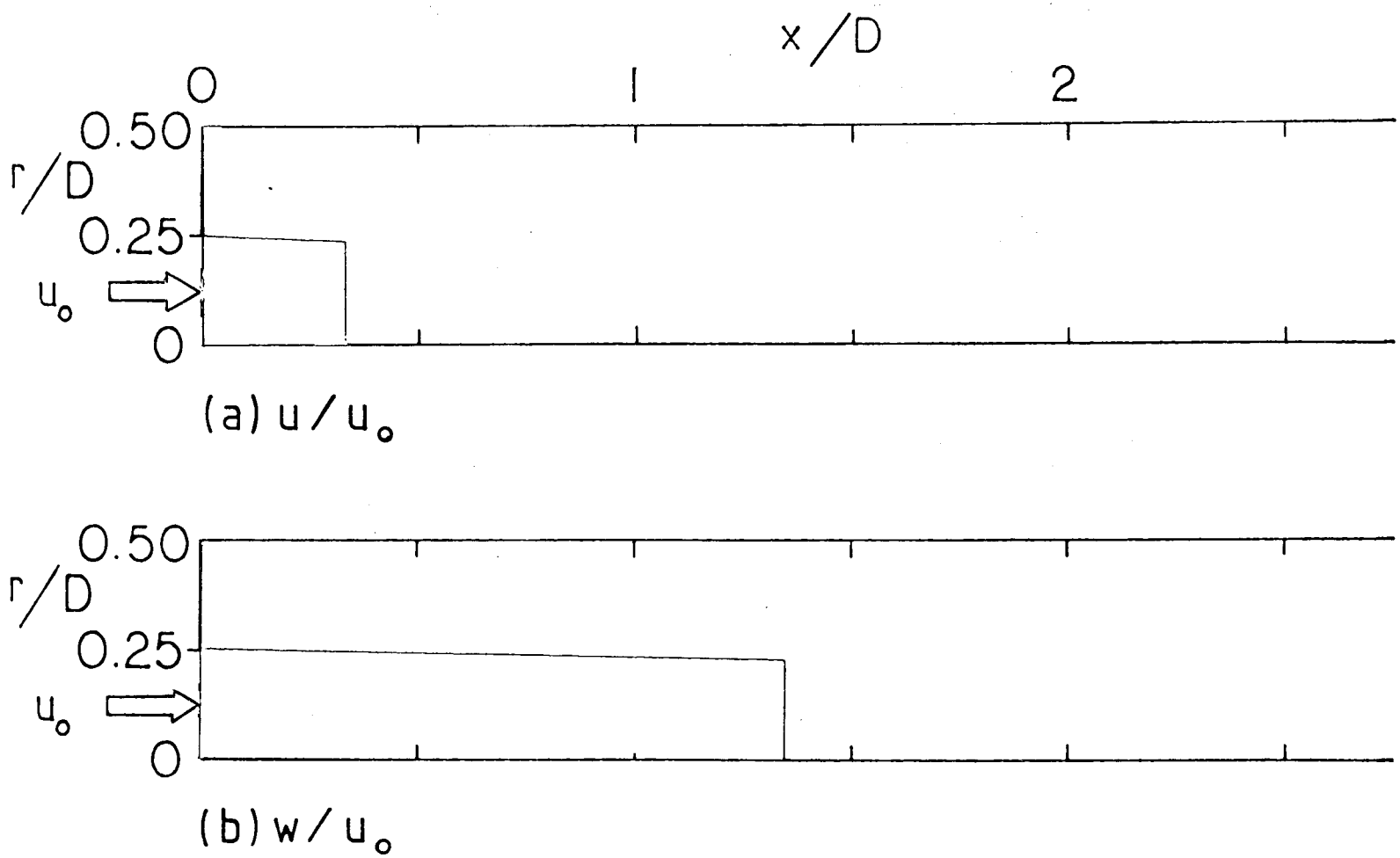

Figure 42. Predicted Velocity Profiles for Wall Expansion Angle $\alpha = 90°$ and Swirl Vane Angle $\phi = 70°$

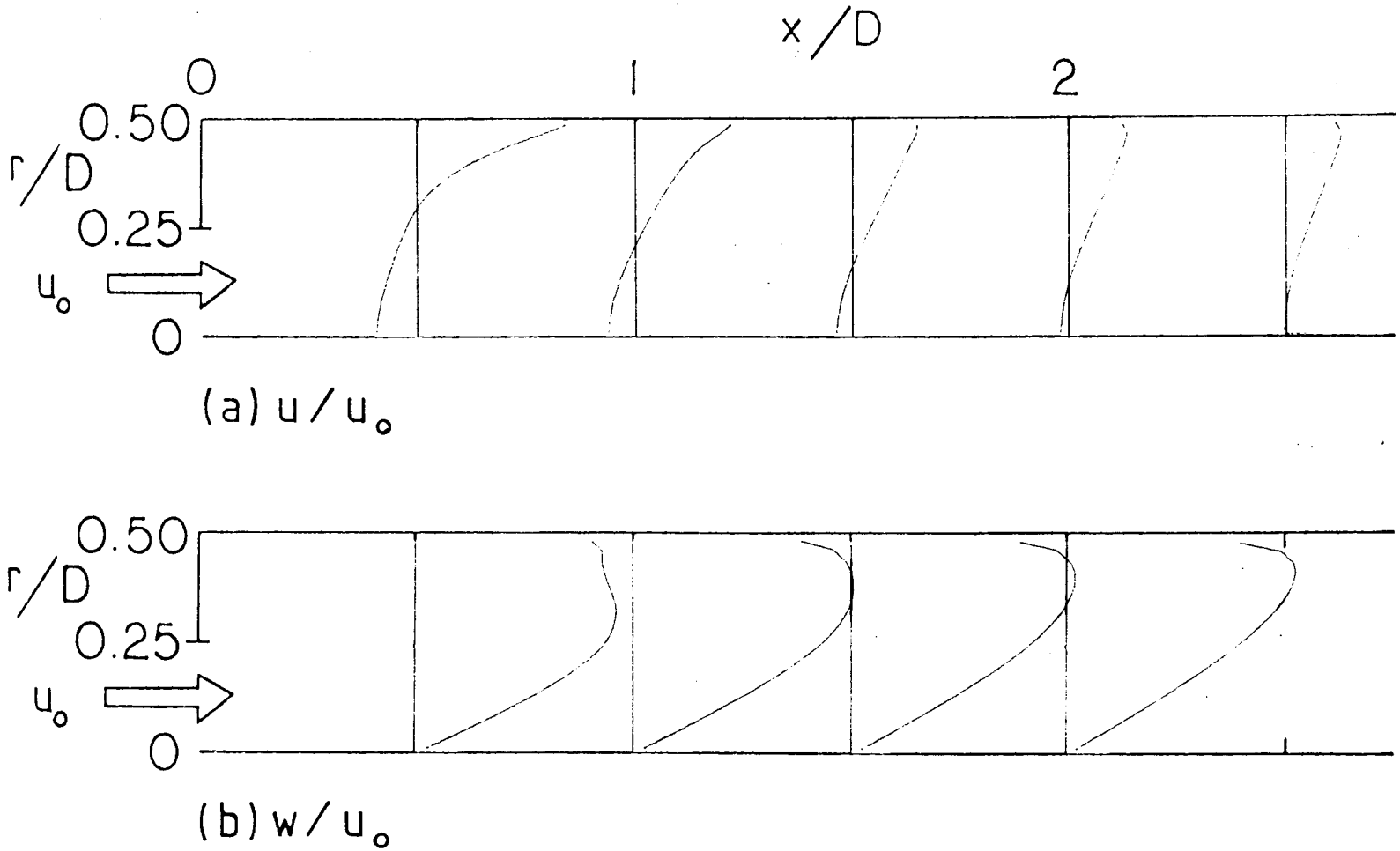

Figure 42. (Continued)

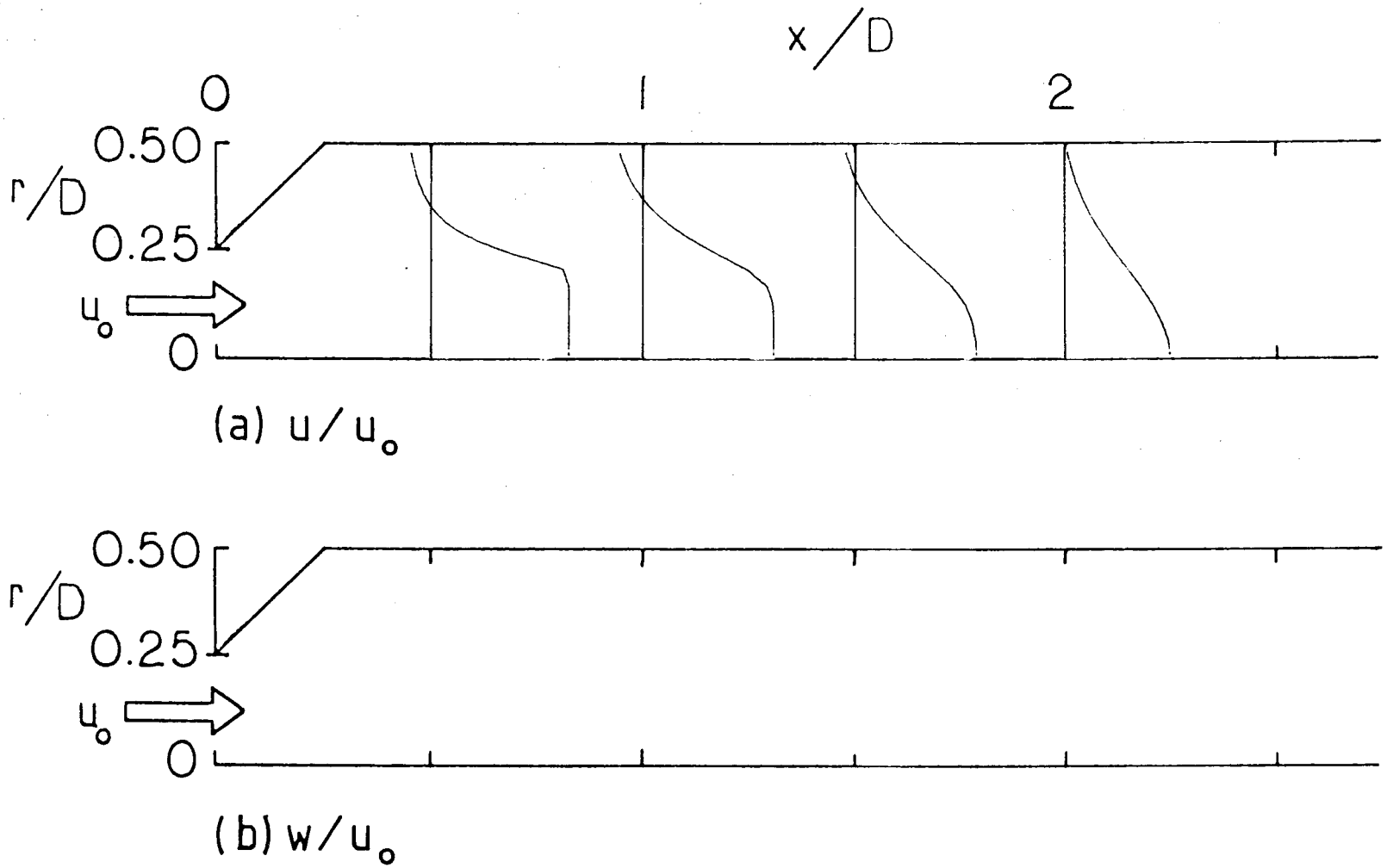

Figure 43. Predicted Velocity Profiles for Wall Expansion Angle $\alpha = 45°$ and Swirl Vane Angle $\phi = 0°$

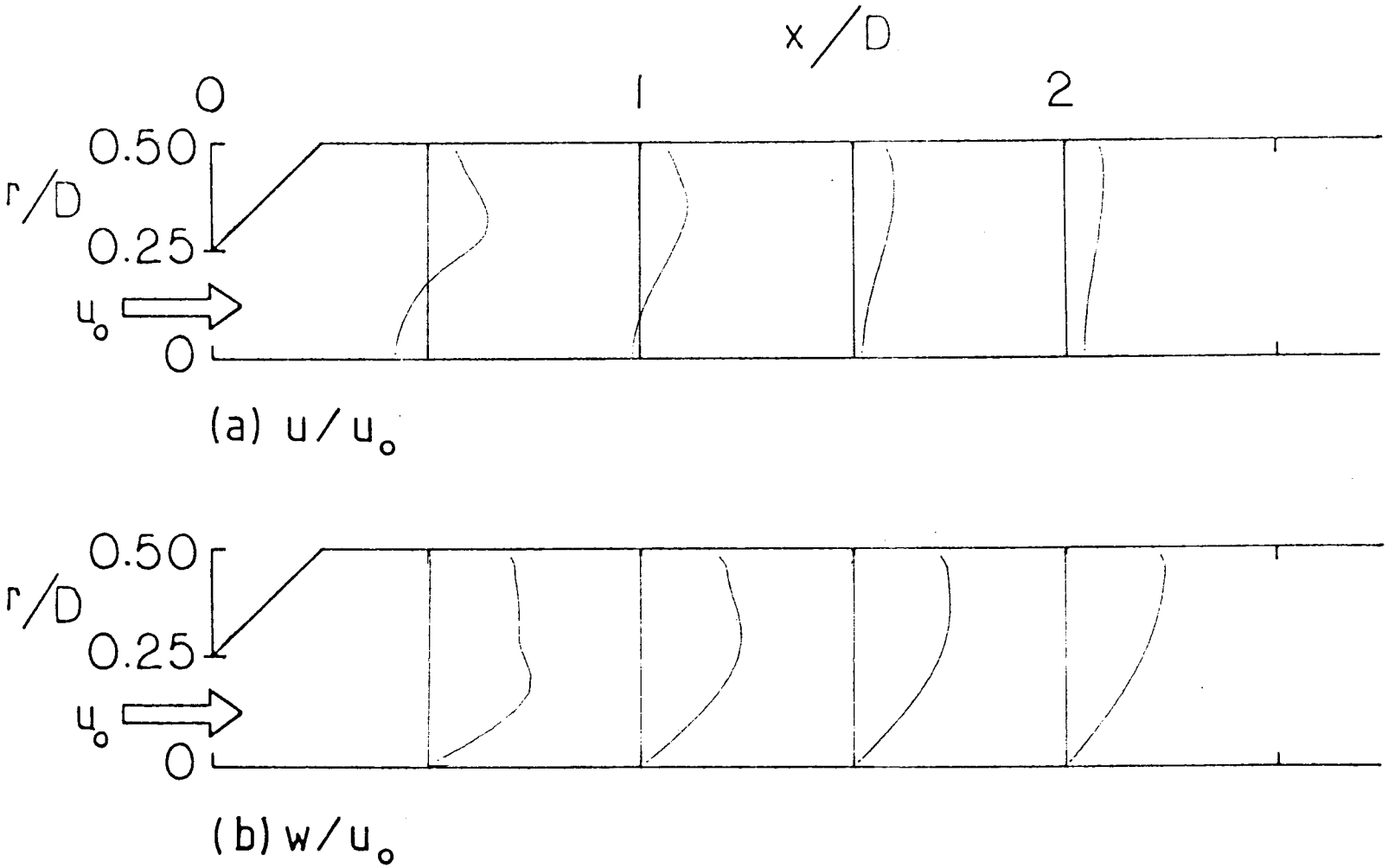

Figure 44. Predicted Velocity Profiles for Wall Expansion Angle $\alpha = 45°$ and Swirl Vane Angle $\phi = 45°$

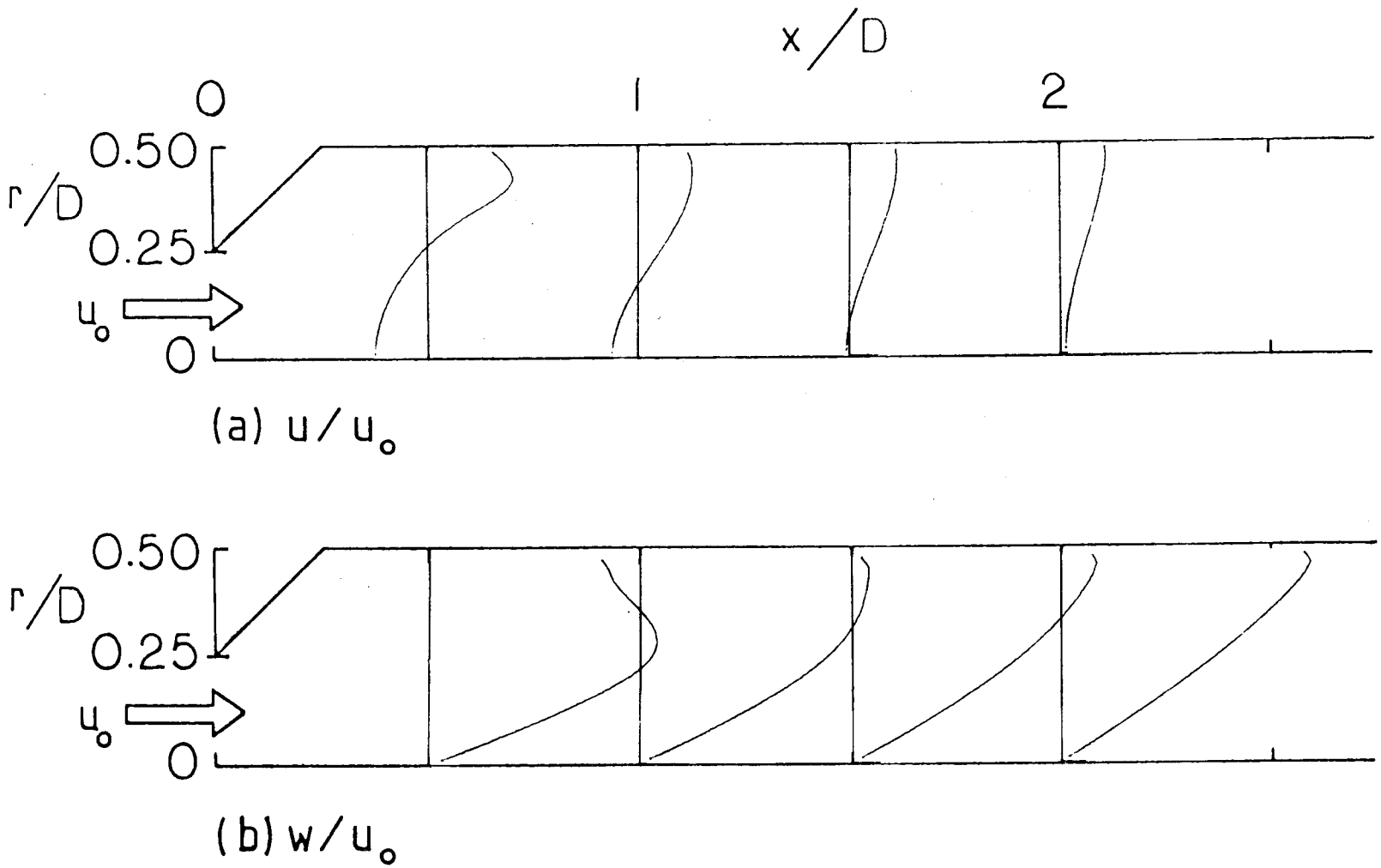

Figure 45. Predicted Velocity Profiles for Wall Expansion Angle $\alpha = 45°$ and Swirl Vane Angle $\phi = 70°$

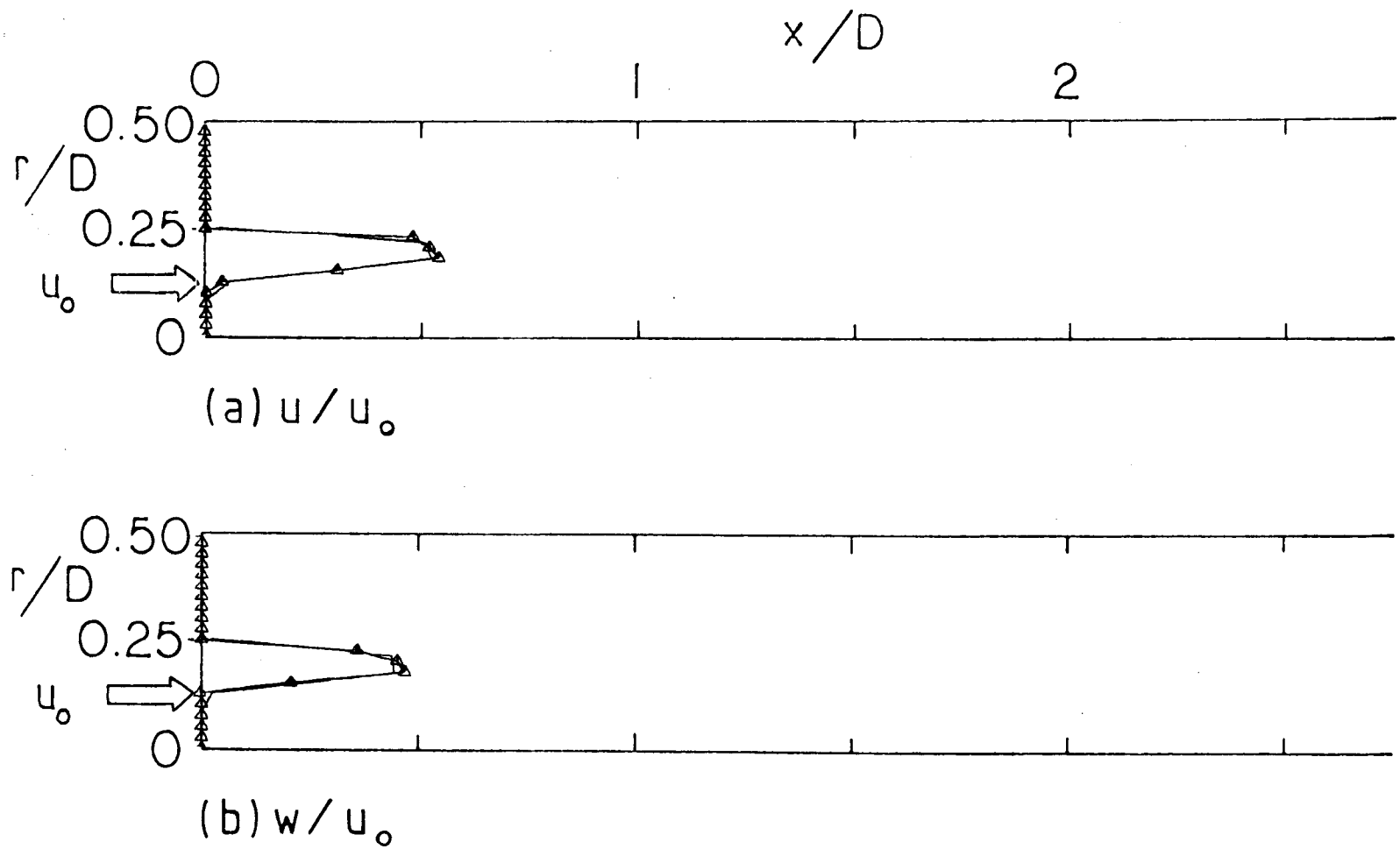

Figure 46. Predicted and Measured Velocity Profiles for a Specific Test Case With Wall Expansion Angle $\alpha = 90°$ and Swirl Vane Angle $\phi = 45°$

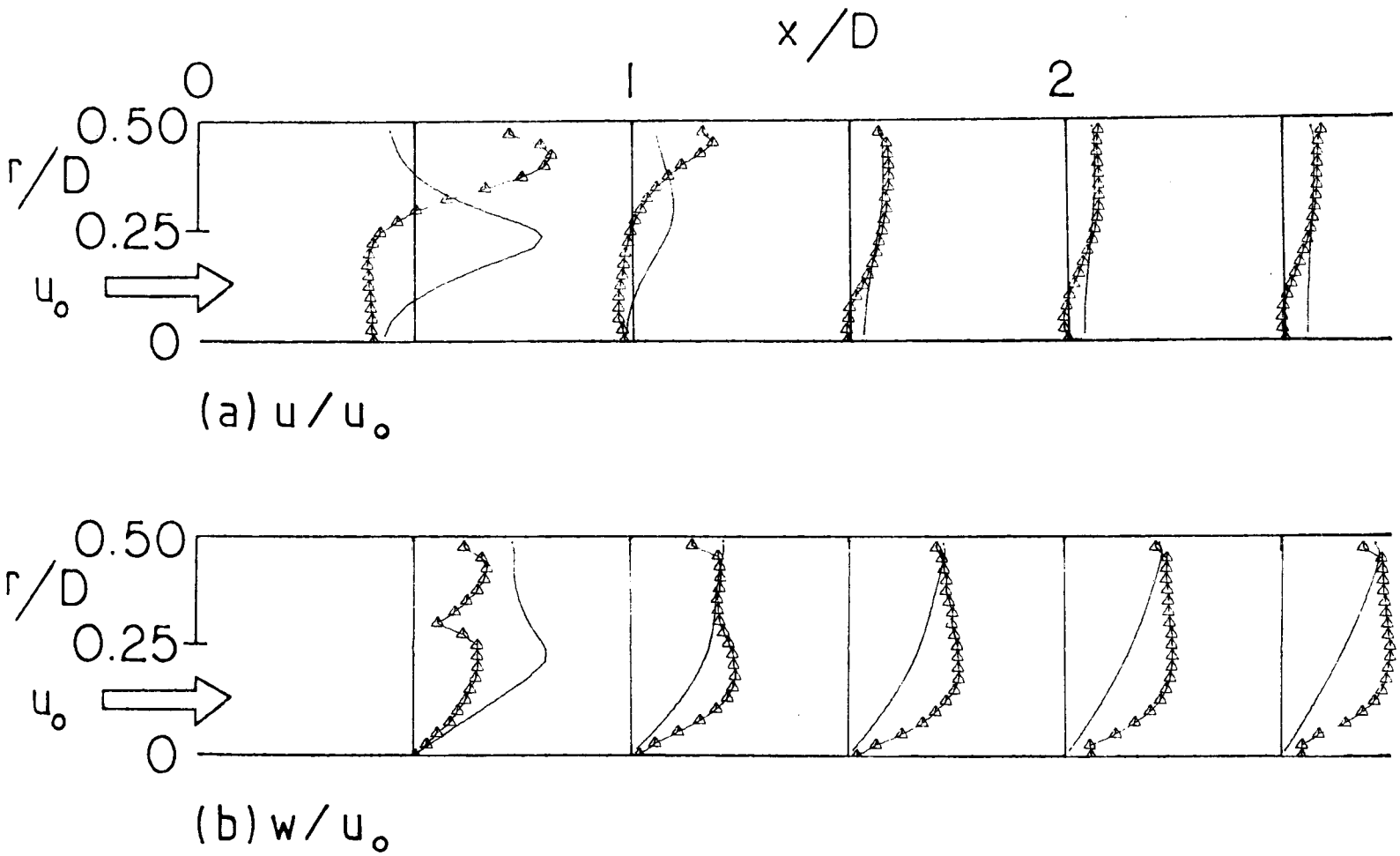

Figure 46. (Continued)

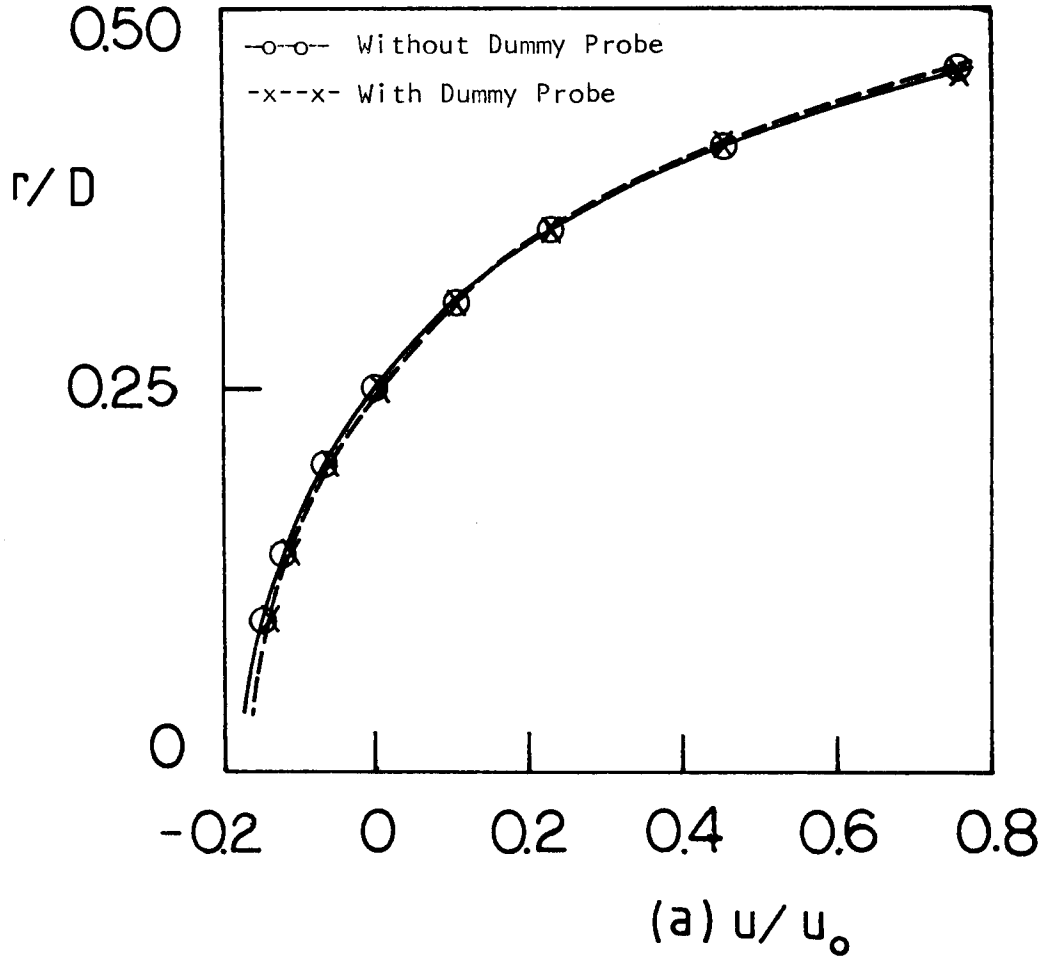

Figure 47. Probe Interference Effect on Measured Velocity Profiles With Wall Expansion Angle α = 90° and Swirl Vane Angle ϕ = 45° at Axial Station x/D = 1.0 for (a) Axial Velocity and (b) Swirl Velocity

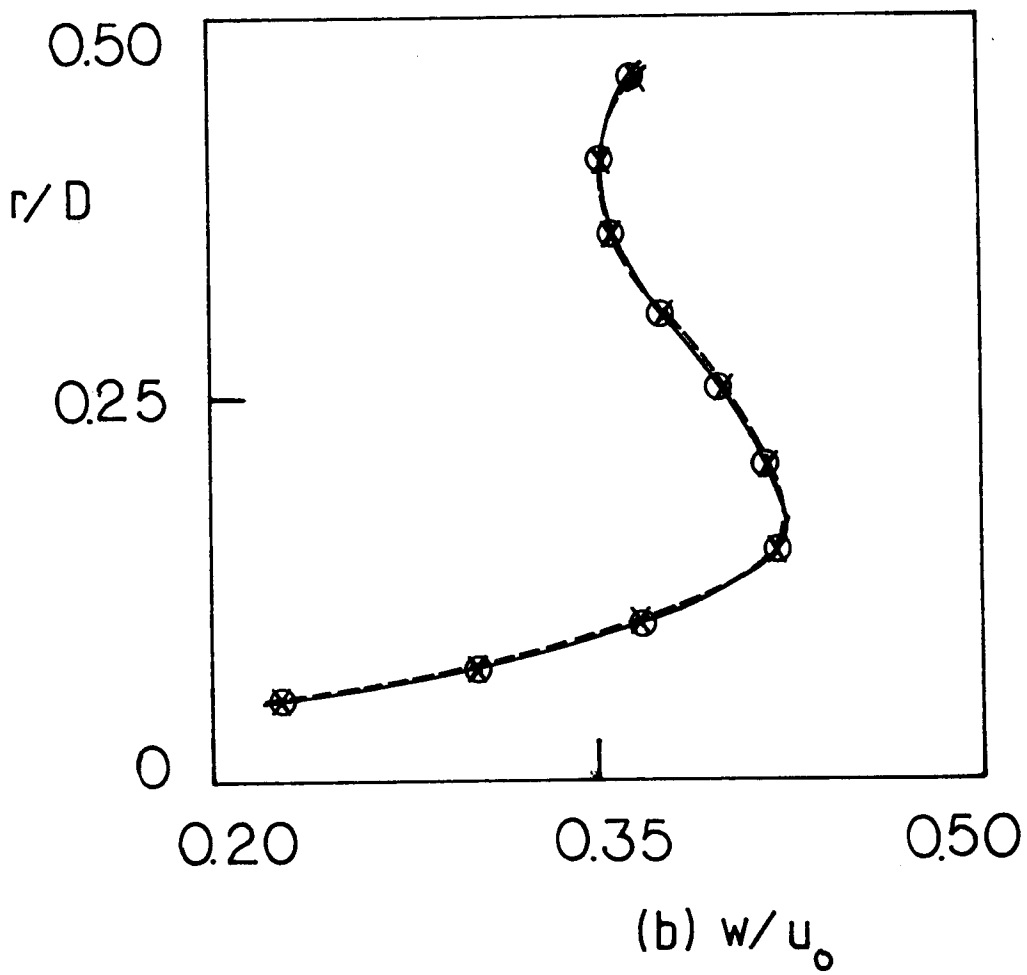

Figure 47. (Continued)

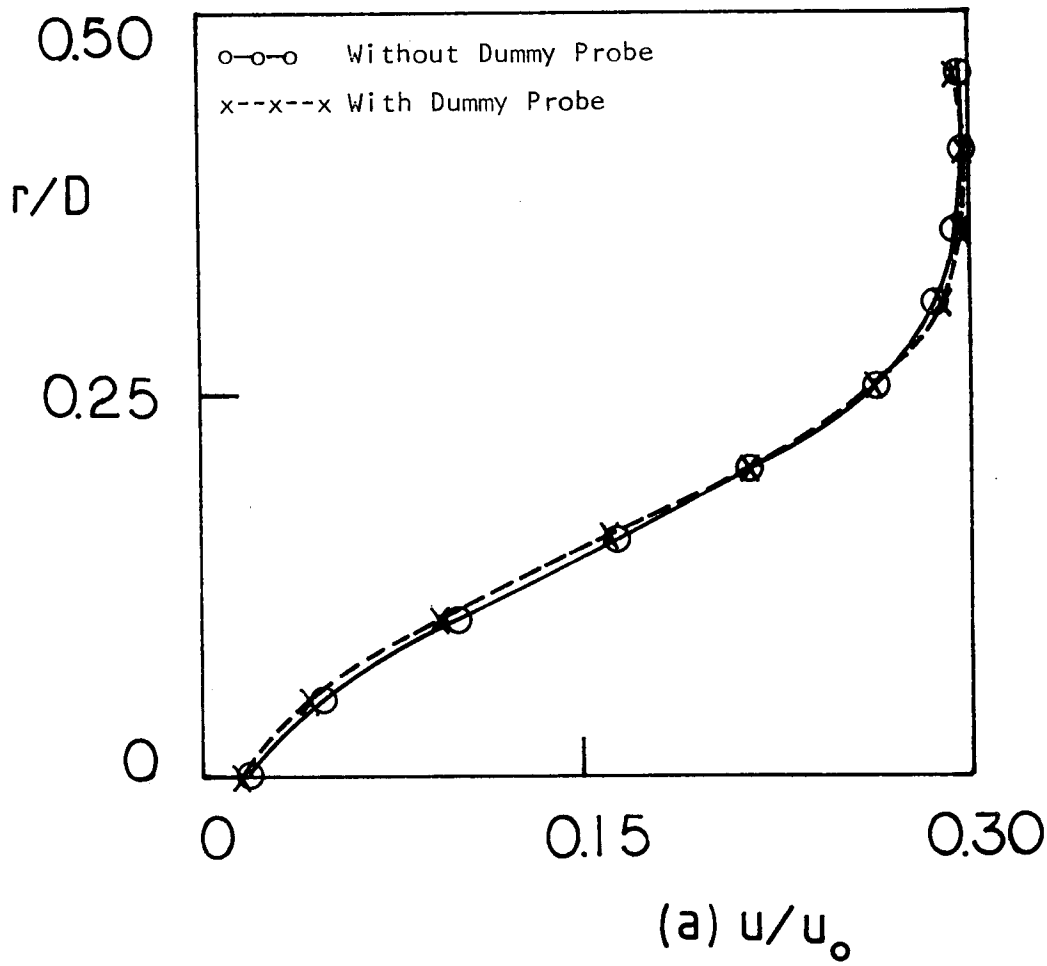

Figure 48. Probe Interference Effect on Measured Velocity Profiles With Wall Expansion Angle α = 90° and Swirl Vane Angle ϕ = 45° at Axial Station x/D = 2.5 for (a) Axial Velocity and (b) Swirl Velocity

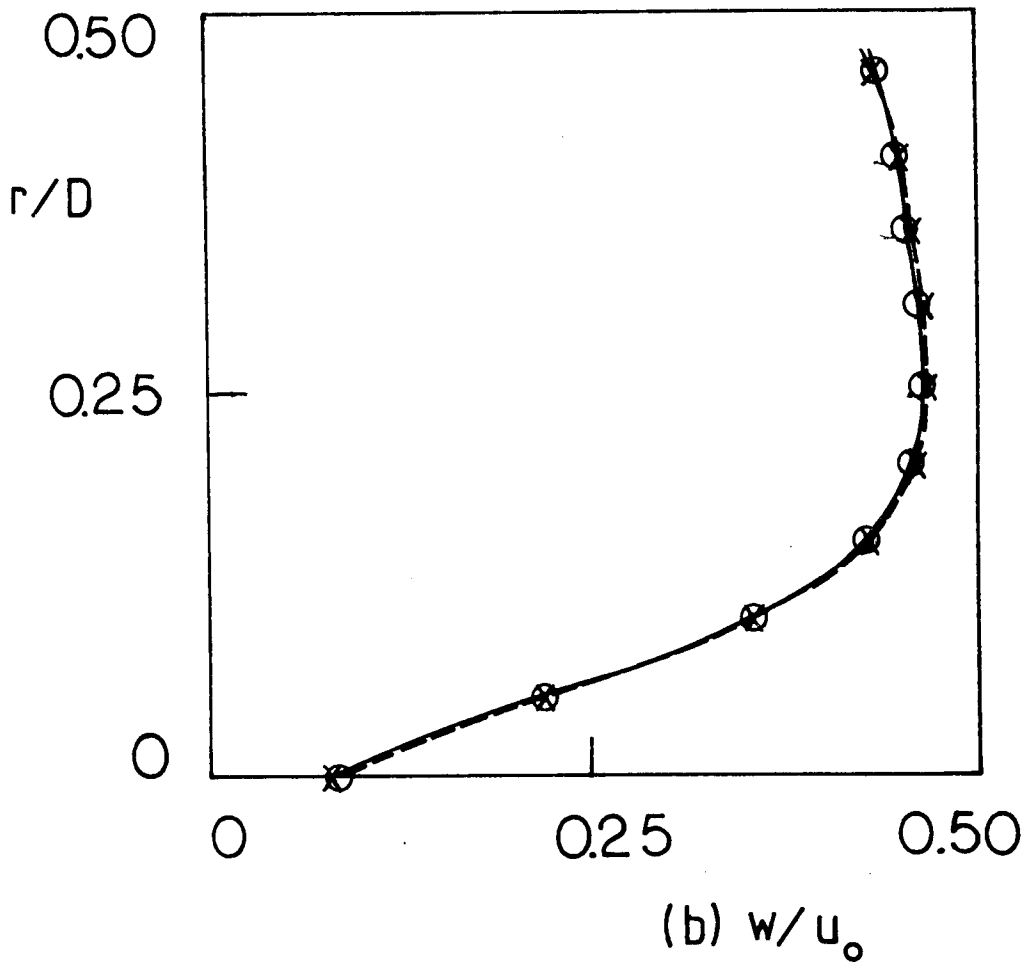

Figure 48. (Continued)

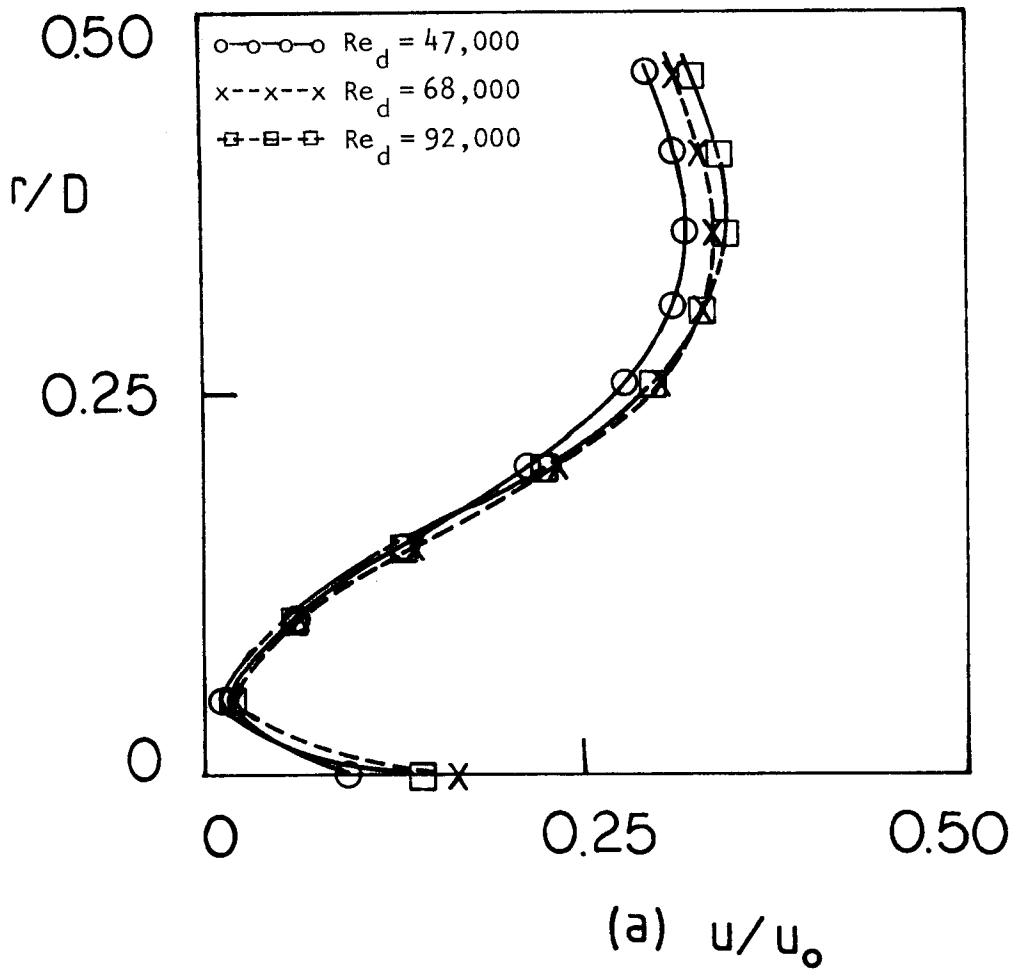

Figure 49. Effect of Inlet Reynolds Number on Measured Velocity Profiles With Wall Expansion Angle $\alpha = 90°$ and Swirl Vane Angle $\phi = 45°$ at Axial Station $x/D = 2.5$ for (a) Axial Velocity and (b) Swirl Velocity

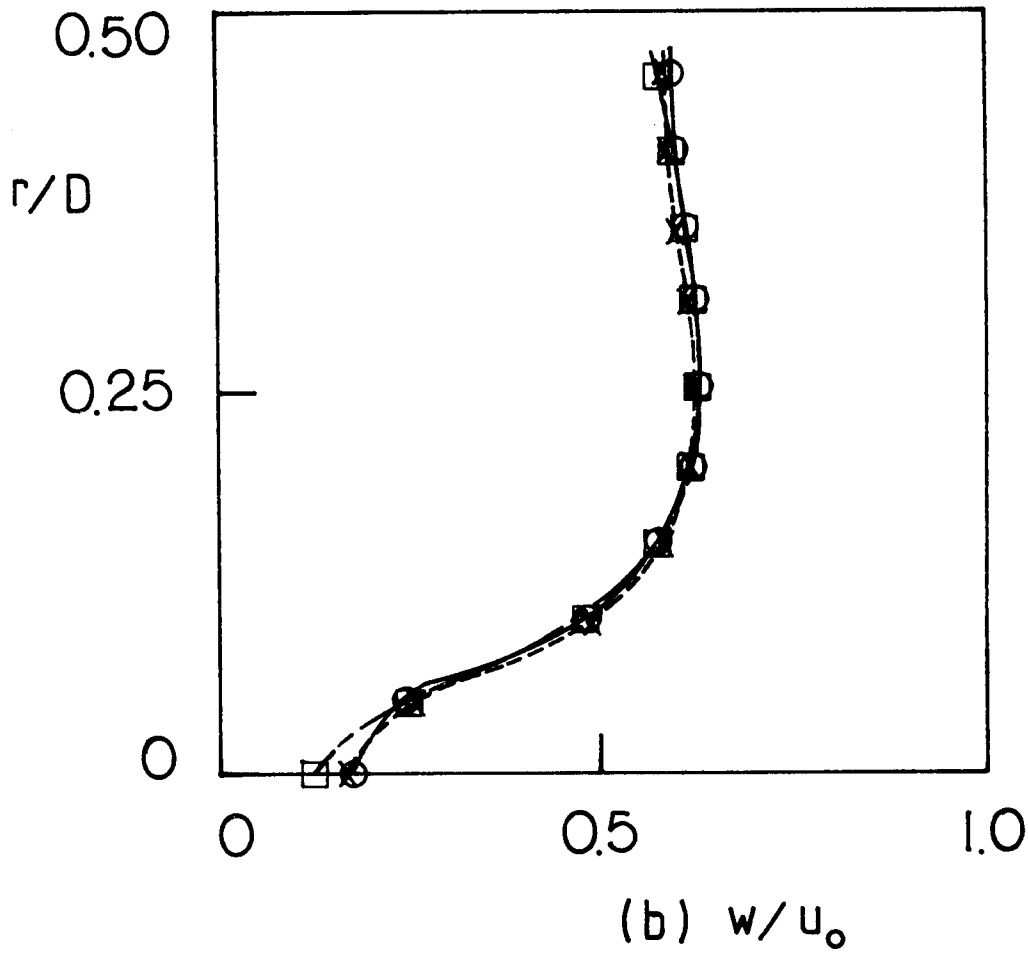

Figure 49. (Continued)

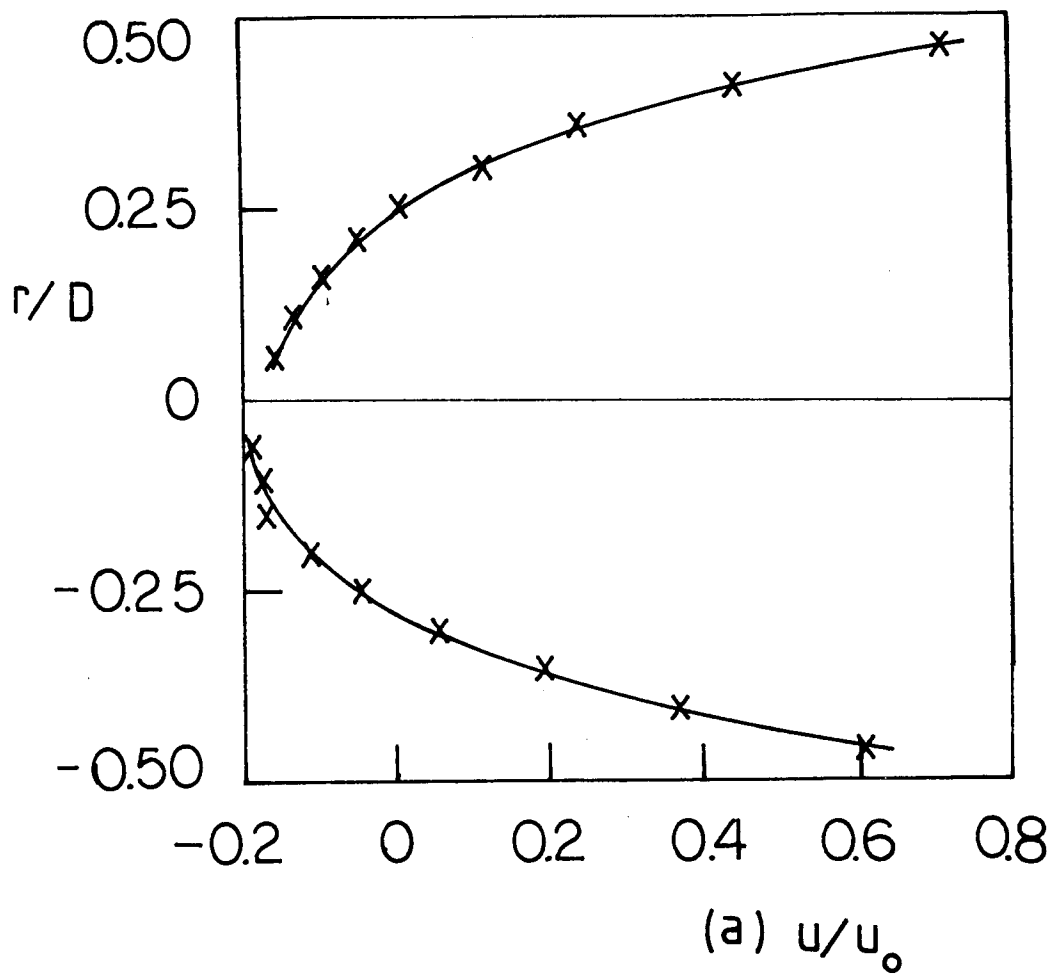

Figure 50. Measured Velocity Profiles From an Entire Diameter Traverse With Wall Expansion Angle α = 90° and Swirl Vane Angle ϕ = 45° at Axial Station x/D = 1.0 for (a) Axial Velocity and (b) Swirl Velocity

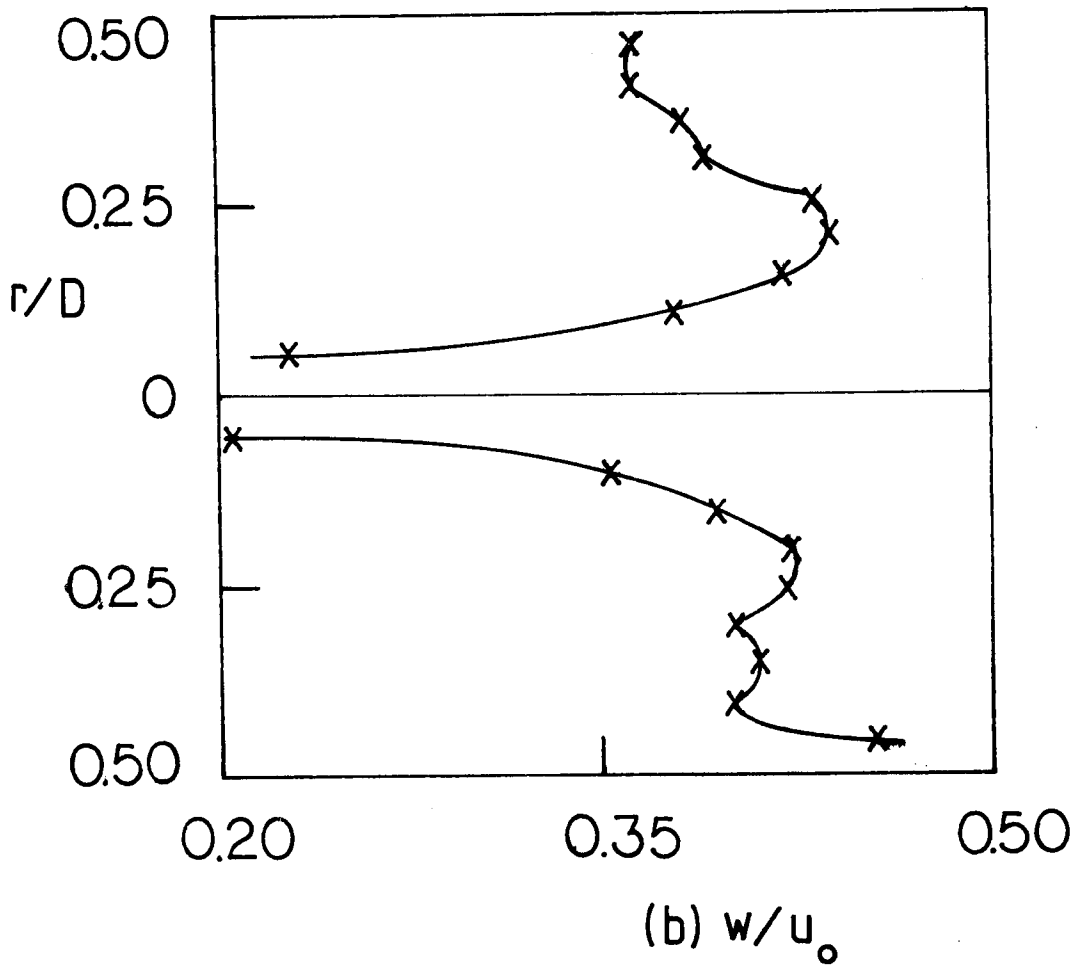

Figure 50. (Continued)

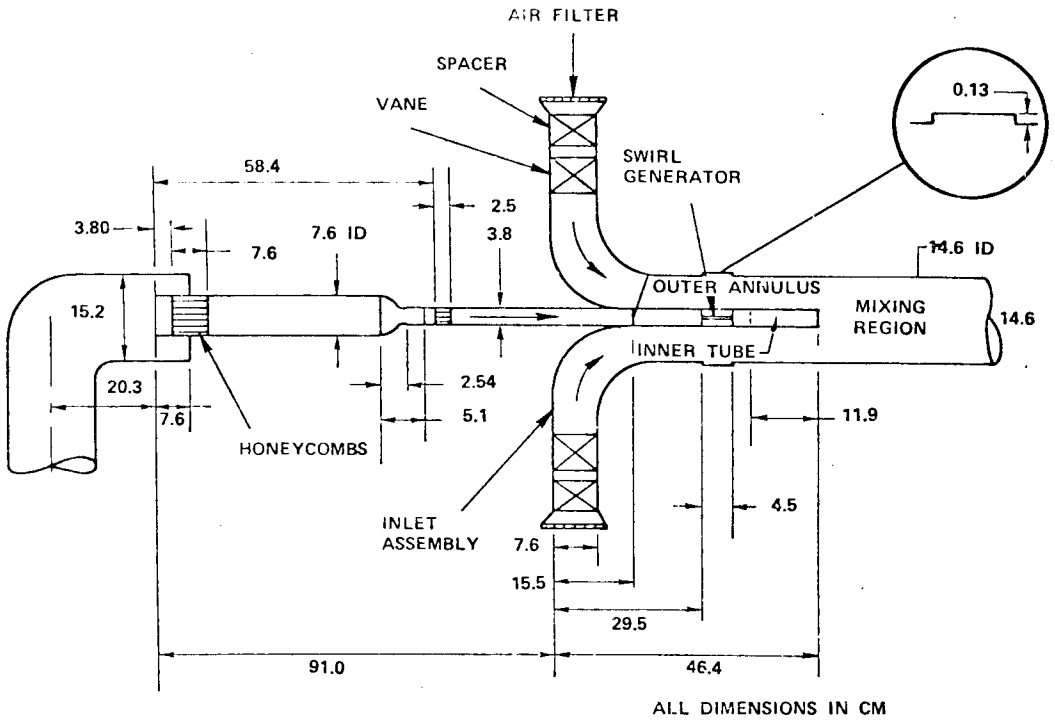

Figure 51. Flow Facility for Counterswirling and Coswirling Flow for Coannular Pipe Flow Prediction Test Cases (49)

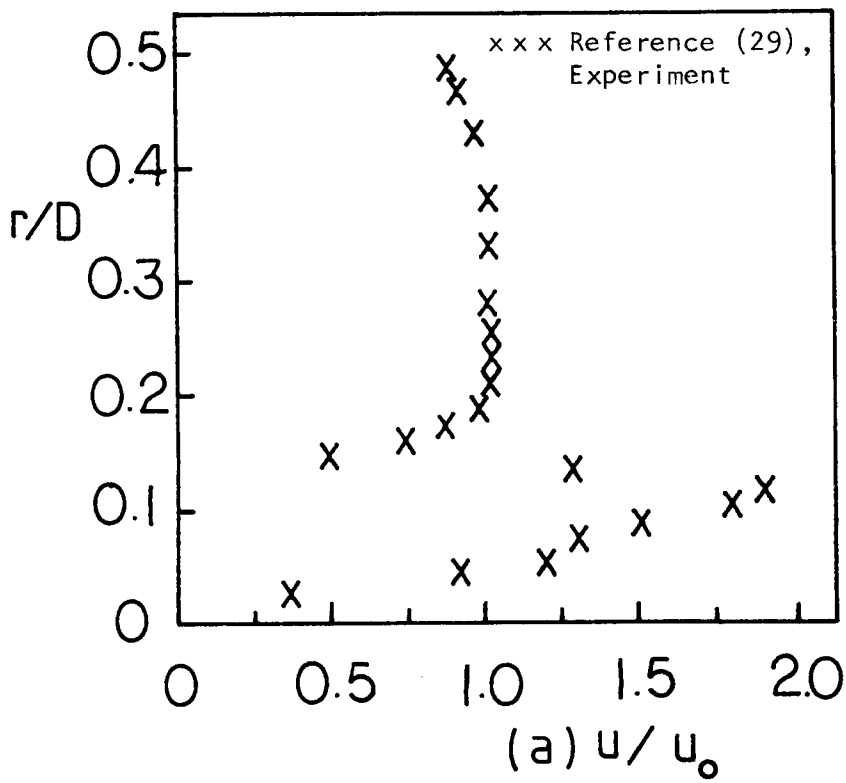

Figure 52. Inlet Velocity Profiles at x/D = 0.01375 (x = 0.002 m) for the Counterswirling Coannular Pipe Flow Test Case (a) Axial Velocity and (b) Swirl Velocity

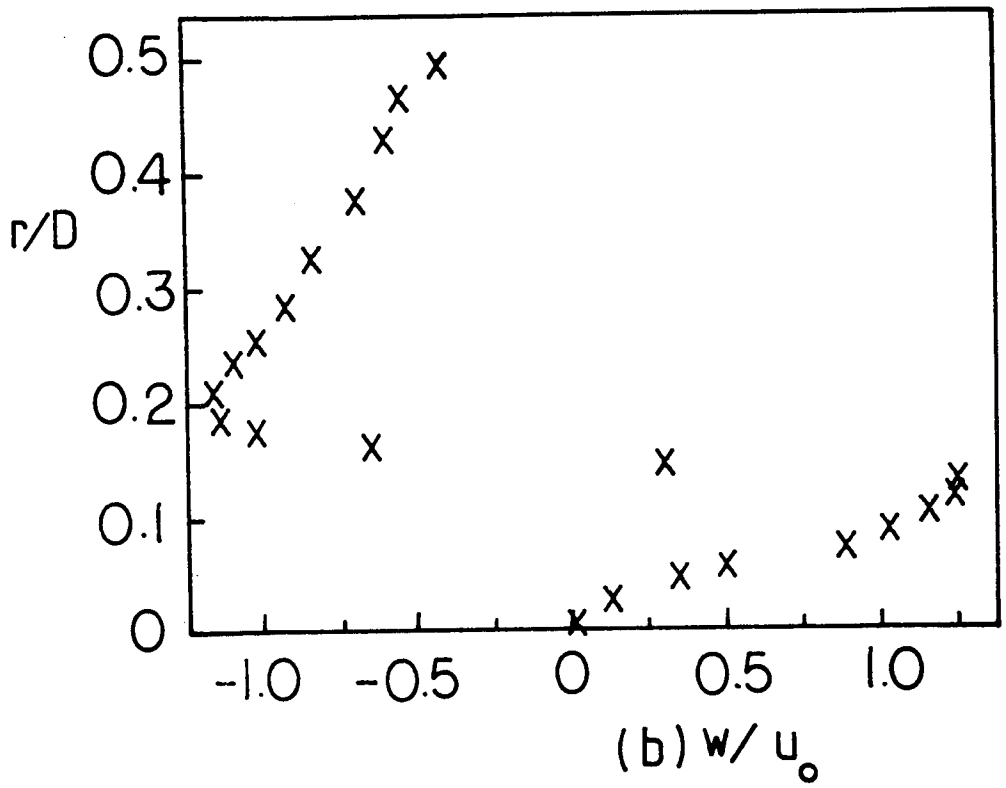

Figure 52. (Continued)

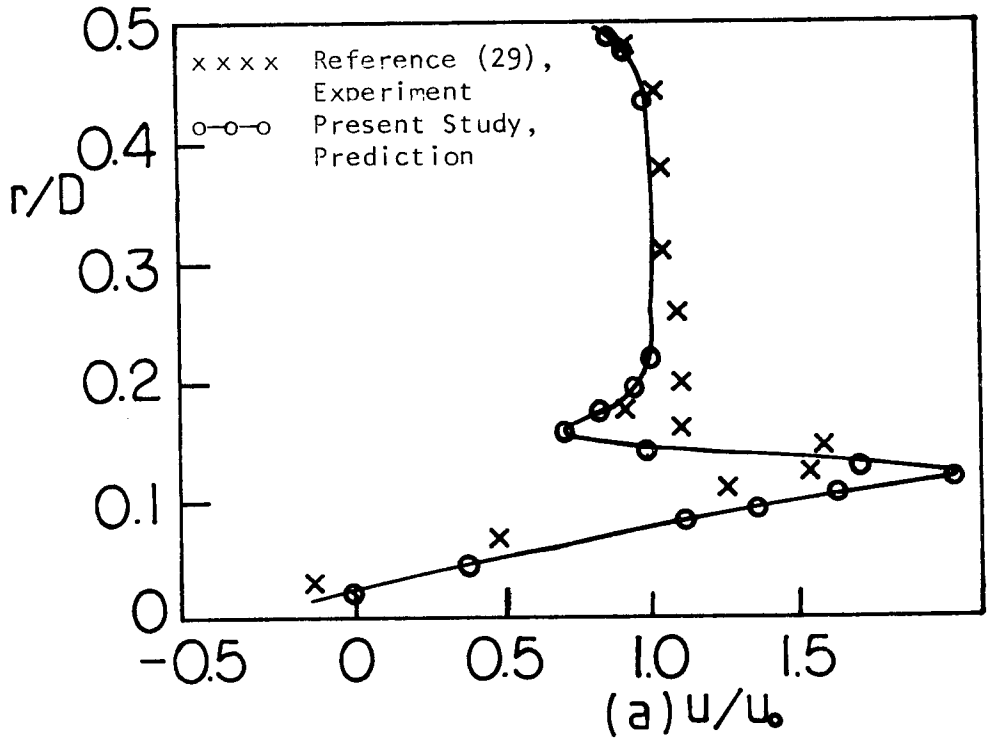

Figure 53. Velocity Profiles at x/D = 0.137 (x = 2 cm) for the Counterswirling Coannular Pipe Flow Test Case (a) Axial Velocity and (b) Swirl Velocity

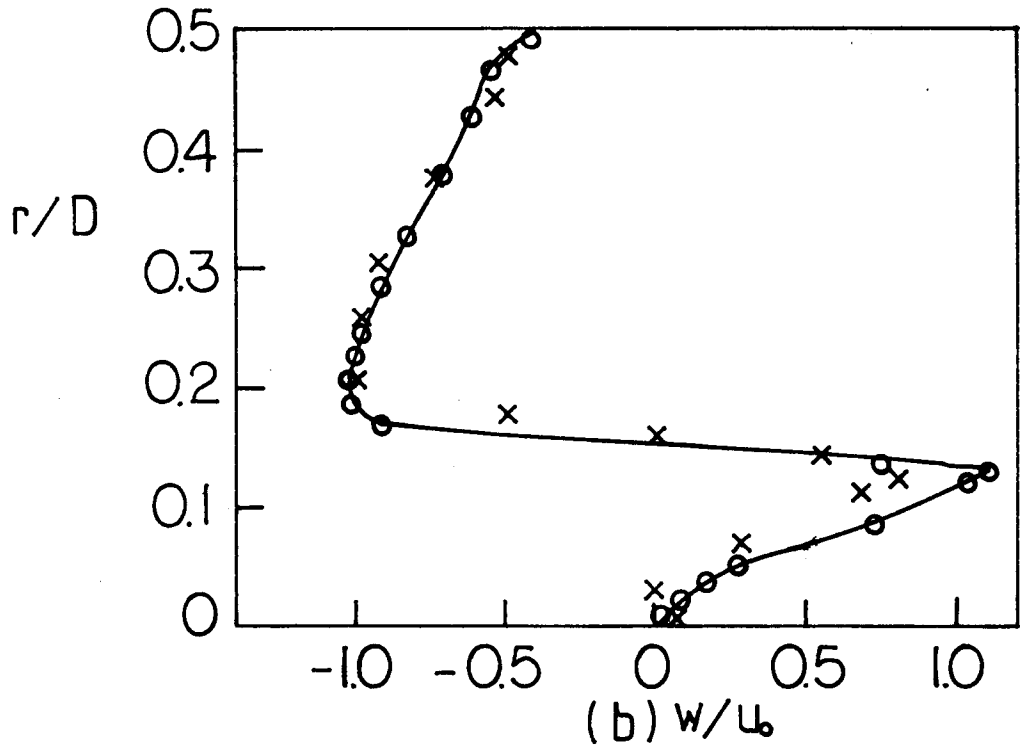

Figure 53. (Continued)

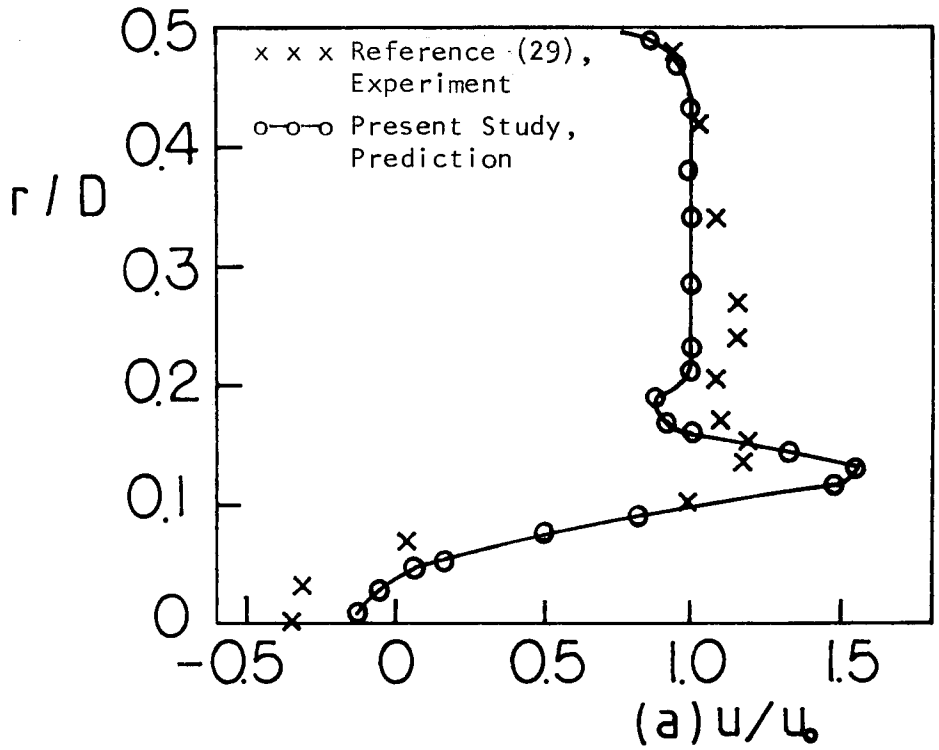

Figure 54. Velocity Profiles at x/D = 0.274 (x = 4 cm) for the Counterswirling Coannular Pipe Flow Test Case (a) Axial Velocity and (b) Swirl Velocity

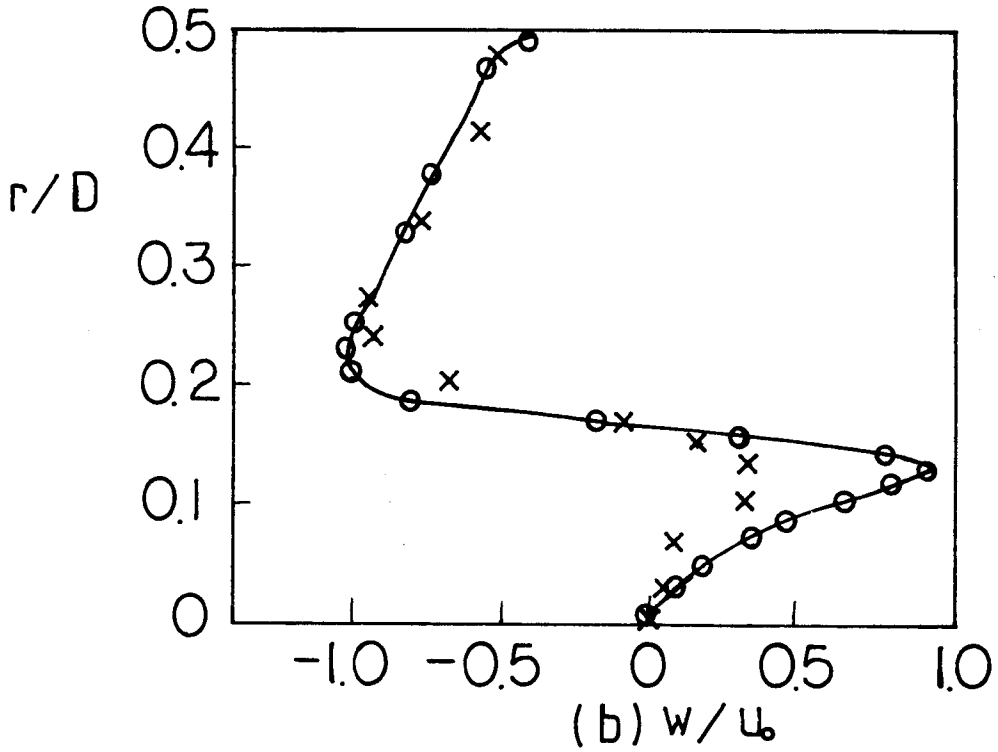

Figure 54. (Continued)

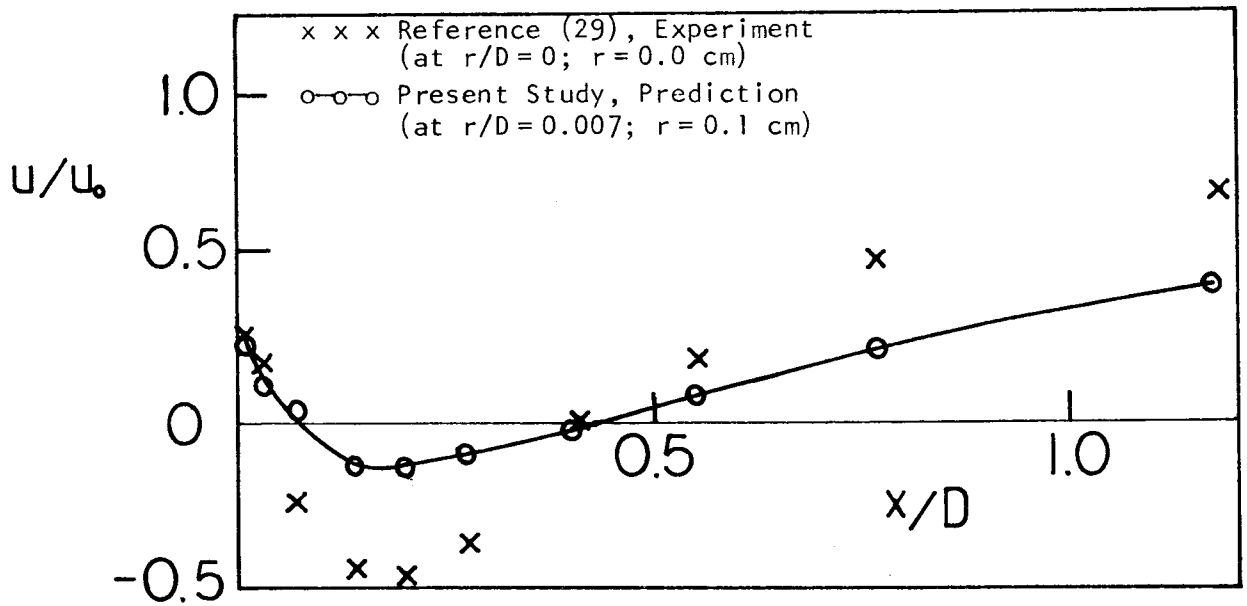

Figure 55. Centerline Axial Velocity Development for the Counter-swirling Coannular Pipe Flow Test Case

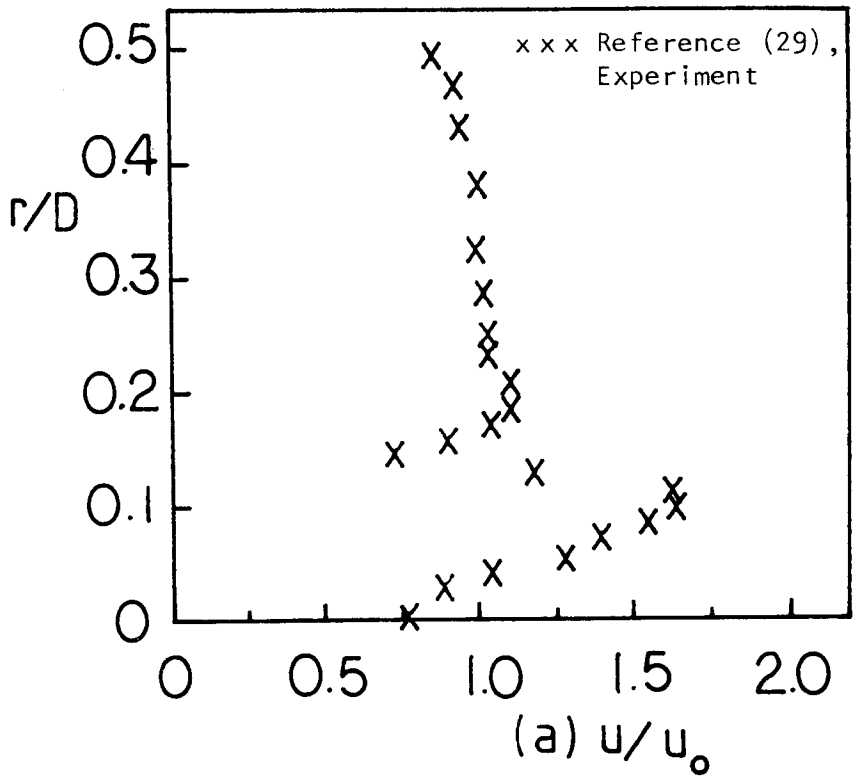

Figure 56. Inlet Velocity Profiles at x/D = 0.01375 (x = 0.2 cm) for the Coswirling Coannular Pipe Flow Test Case (a) Axial Velocity and (b) Swirl Velocity

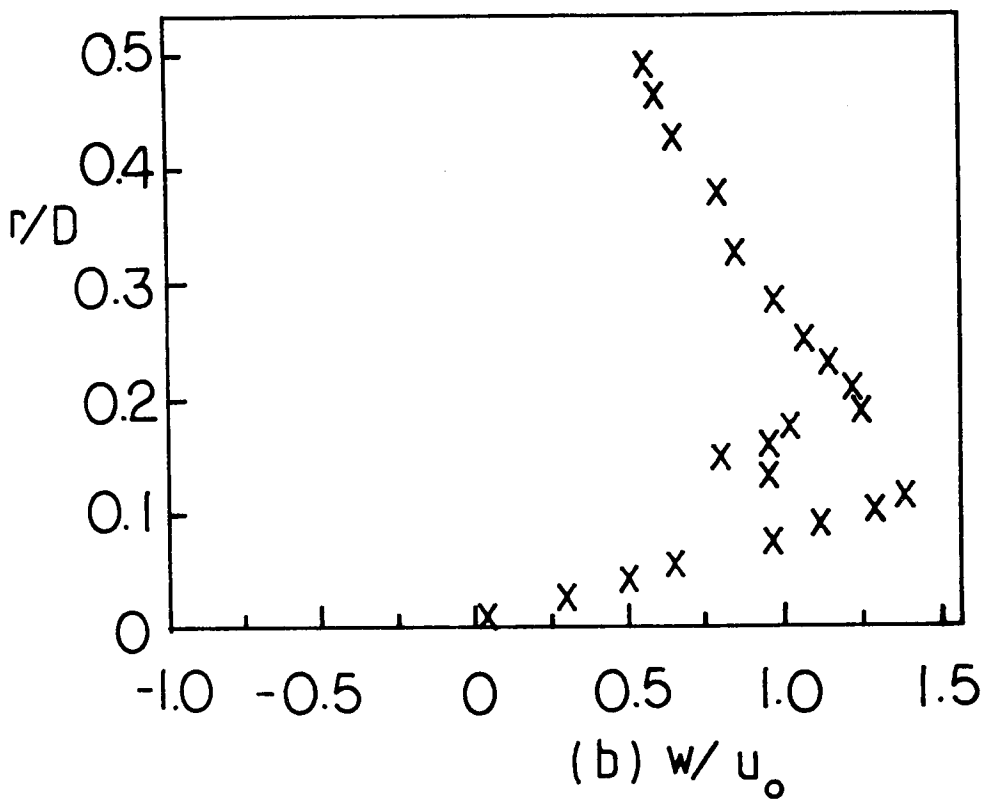

Figure 56. (Continued)

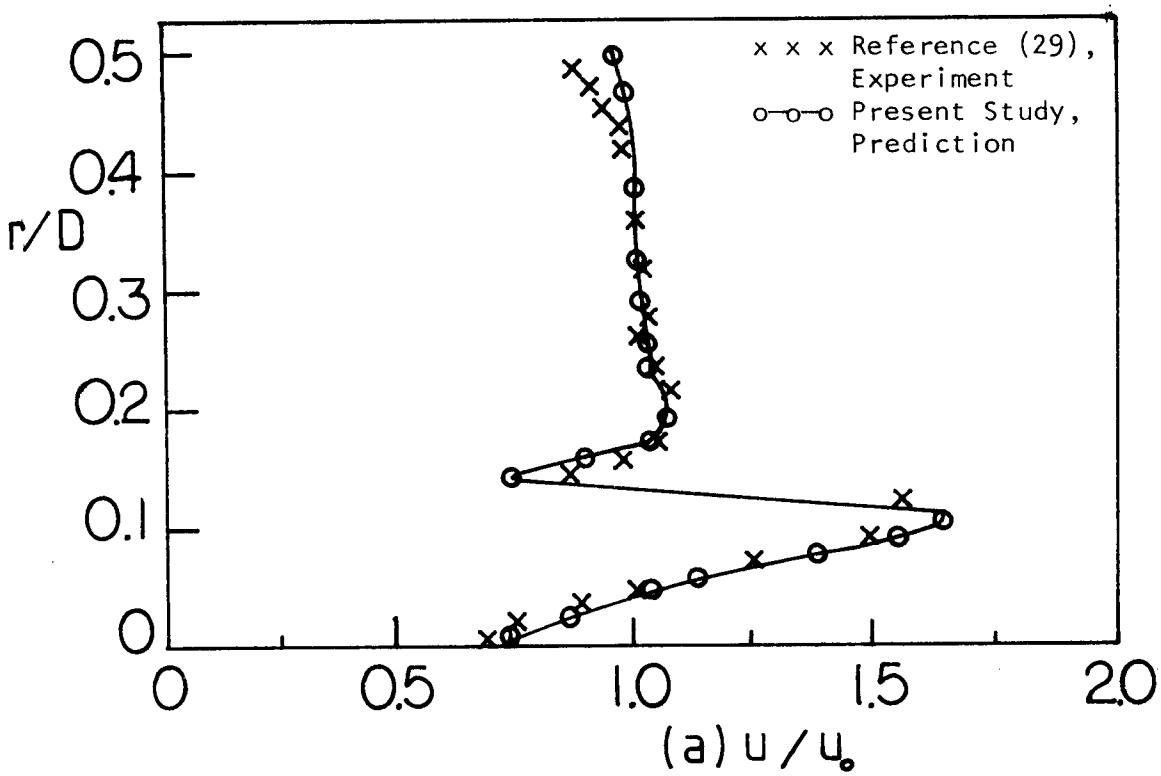

Figure 57. Velocity Profiles at x/D = 0.069 (x = 1 cm) for the Coswirling Coannular Pipe Flow Test Case (a) Axial Velocity and (b) Swirl Velocity

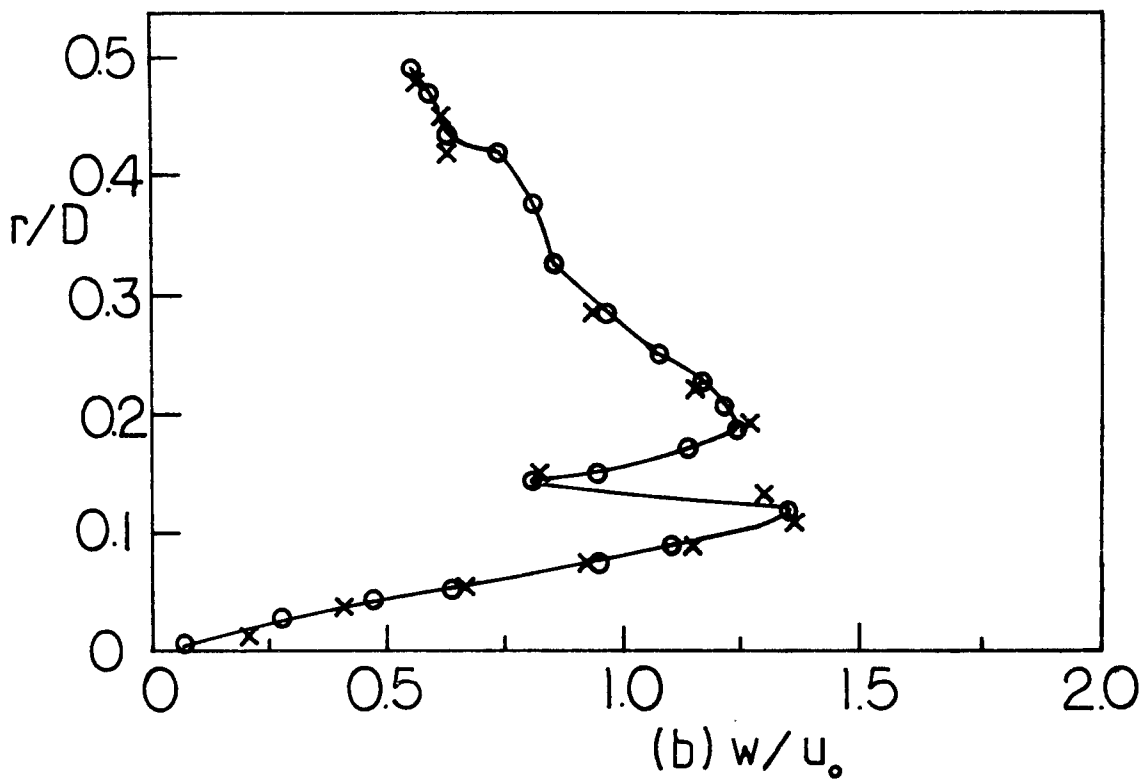

Figure 57. (Continued)

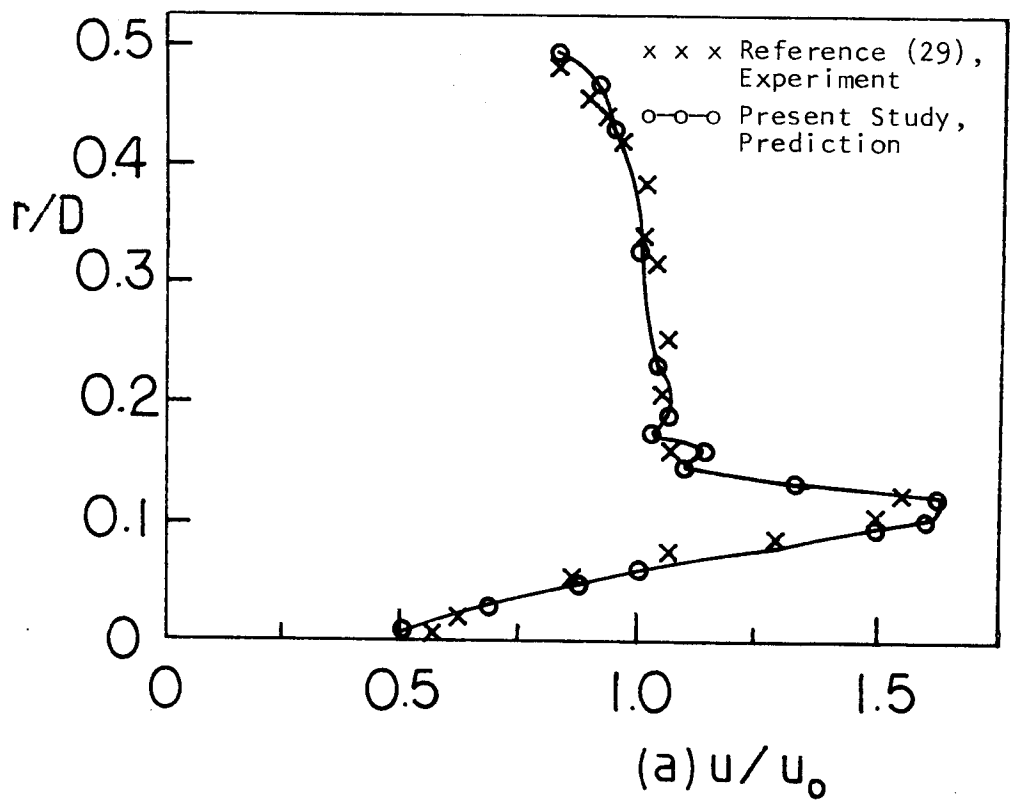

Figure 58. Velocity Profiles at x/D = 0.206 (x = 3 cm) for the Coswirling Coannular Pipe Flow Test Case (a) Axial Velocity and (b) Swirl Velocity

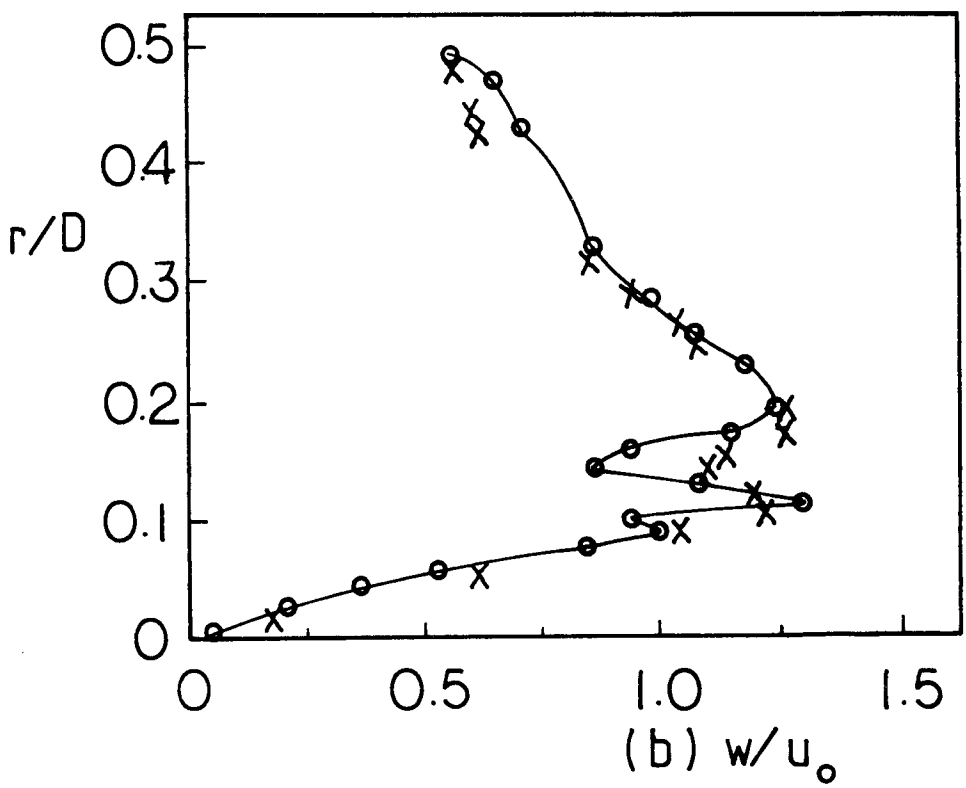

Figure 58. (Continued)

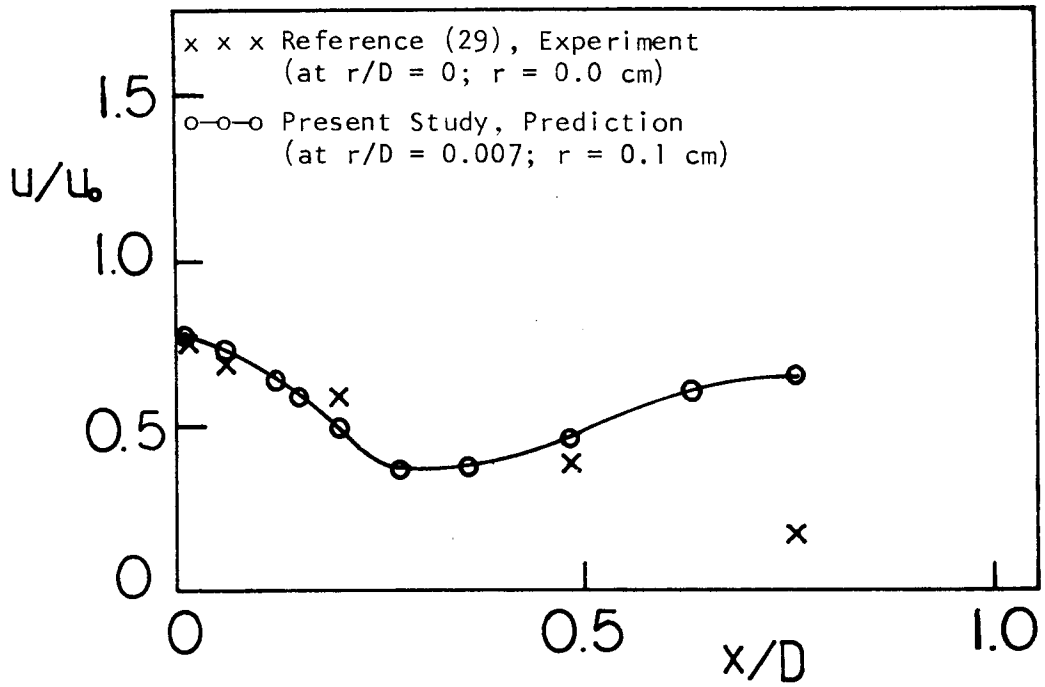

Figure 59. Centerline Axial Velocity Development for the Coswirling Coannular Pipe Flow Test Case

APPENDIX C - DATA REDUCTION COMPUTER PROGRAM LISTING FOR FIVE-HOLE PITOT PROBE MEASUREMENTS

```
C     A COMPUTER PROGRAM FOR DATA REDUCTION OF FIVE-HOLE PITOT
C     MEASUREMENTS IN TURBULENT, SWIRLING, RECIRCULATING, FLOW
C     IN COMBUSTOR GEOMETRIES
C
C     VERSION OF MAY, 1981
C
C     D L RHODE
C     MECHANICAL AND AEROSPACE ENGINEERING
C     OKLAHOMA STATE UNIVERSITY
C     STILLWATER, OK      74078
C
C
CA*********************************************************************
CHAPTER  0  0  0  0  0  0  0  0  PRELIMINARIES  0  0  0  0  0  0  0  0
C
      DIMENSION HEDM(9),HEDUMN(9),HEDNMS(9),HEDCMW(9),
     #HEDU(9),HEDV(9),HEDW(9),HEDVT(9),HEDUST(9),
     #HEDVST(9),HEDWST(9),HEDVTS(9),HEDDEL(9),HEDBET(9),
     #HEDMMF(9),HEDMIV(9),HEDMIF(9),HEDMPP(9),HEDAM(9)
C
      COMMON
     #/CALIB/CPITCH(26),CDELTA(26),CVELCF(26)
     #/MEASUR/RBETA(48,24),RPNMPS(48,24),RPCMPW(48,24),NDATA(48),MAXJPT,
     #    RDNPRS(48)
     #/GEOM/X(48),R(24),XND(48),RND(24),DYPS(24),DYNP(24),
     #    SNS(24),NSTATN,XINCHS(48),RINCHS(24)
     #/CALC/VTOTAL(48,24),U(48,24),V(48,24),W(48,24),
     #    VTSTAR(48,24),USTAR(48,24),VSTAR(48,24),WSTAR(48,24),
     #    PICHCF(48,24),VELCF(48,24),DELTA(48,24),BETA(48,24),
     #ANGMOM(48), UMEAN(48),MASS(48),MASFLO(48),UIN(48)
      REAL MASS,MASFLO
      LOGICAL IWRITE,DIAGNS
C---------SET IWRITE=.TRUE. FOR WRITING SOLN. ON DISK STORAGE
C---------SET DIAGNS=.TRUE. TO ACTIVATE DIAGNOSTIC WRITE STATEMENTS
C---------NSTATN IS NO. OF AXIAL STATIONS FOR WHICH DATA IS
C              SUPPLIED
C---------MAXJPT IS MAX. NO. OF RADIAL POSITIONS FOR ALL AXIAL
C               STATIONS
C---------CPITCH IS CALIBRATION PITCH COEFF.
C---------CDELTA IS CALIBRATION PITCH ANGLE(DEG.)
C---------CVELCF IS CALIBRATION VELOCITY COEFF.
C---------NCAL IS NO. OF CALIBRATION POINTS
C---------XINCHS IS AXIAL POSITION(IN.) OF EACH PARTICULAR
C              RADIAL TRAVERSE
C---------NDATA IS NO. OF RADIAL LOCATIONS FOR WHICH DATA IS
C              SUPPLIED FOR EACH PARTICULAR RADIAL TRAVERSE
C---------RDNPRS IS MEASURED DYNAMIC PRESSURE ENTERING THE
C              SWIRLER
C---------RINCHS IS RADIAL POSITION(IN.) OF EACH MEASUREMENT
C              LOCATION IN EACH PARTICULAR RADIAL TRAVERSE
C---------RBETA IS MEASURED FLOW ANGLE(DEG.) WHERE YAW
C              ANGLE BETA = 360.0 - RBETA
C---------RDNPRS IS MEASURED VOLTS FOR PNORTH - PSOUTH
C              DIFF. PRESSURE
C---------RPCMPW IS MEASURED VOLTS FOR PCENTER - PWEST
C              DIFF. PRESSURE
C---------PICHCF IS REDUCED VALUE FOR PITCH COEFF.
C---------DELTA IS REDUCED VALUE FOR PITCH ANGLE(DEG.)
C---------VELCF IS REDUCED VALUE FOR VELOCITY COEFF.
C---------BETA IS REDUCED VALUE FOR PROBE YAW ANGLE(DEG.)
C---------VTOTAL IS TOTAL VECTOR VELOCITY MAGNITUDE(M/SEC)
C---------U IS AXIAL VELOCITY (M/SEC)
C---------V IS RADIAL VELOCITY (M/SEC)
C---------W IS SWIRL VELOCITY (M/SEC)
C---------VTSTAR IS DIMENSIONLESS TOTAL VELOCITY
C---------USTAR IS DIMENSIONLESS AXIAL VELOCITY
C---------VSTAR IS DIMENSIONLESS RADIAL VELOCITY
C---------WSTAR IS DIMENSIONLESS SWIRL VELOCITY
C---------ALL PRIMARY USER INPUTS ARE LOCATED HERE
      IWRITE=.TRUE.
      DIAGNS=.TRUE.
      ALPHA=90.
      PHI=45.
```

```
      VISCOS=1.8E-5
      NSTATN=6
      MAXJPT=20
      PATM=73.8
      TATM=28.
      IT=48
      JT=24
      RLARGE=11.75/(2.0*39.37)
      RSMALL=RLARGE/2.0
      READ(5,205) HEDM,HEDUMN,HEDU,HEDV,HEDW,
     #    HEDVT,HEDUST,HEDVST,HEDWST,HEDVTS,HEDDEL,HEDBET,
     #HEDNMS,HEDCMW,HEDMMF,HEDMIV,HEDMIP,HEDMPP,HEDAM
  205 FORMAT(9A4)
C---------INITIALIZE VARIABLES TO ZERO
      CALL INIT
C---------READ FIVE-HOLE PITOT CALIBRATION DATA
      NCAL=25
      DO 10 I=1,NCAL
      READ(5,210) CPITCH(I),CDELTA(I),CVELCF(I)
   10 CONTINUE
  210 FORMAT(3F10.5)
      IF(DIAGNS) WRITE(6,400) (CPITCH(I),I=1,25)
      IF(DIAGNS) WRITE(6,400) (CDELTA(I),I=1,25)
      IF(DIAGNS) WRITE(6,400) (CVELCF(I),I=1,25)
  400 FORMAT(///,1X,13(F8.4,1X),//,5X,12(F8.4))
C---------READ RAW MEASURED DATA TO BE REDUCED
      DO 30 I=1,NSTATN
      READ(5,230) XINCHS(I),NDATA(I),RDNPRS(I)
      JPTS=NDATA(I)
      DO 20 J=1,JPTS
      READ(5,220) RINCHS(J),RBETA(I,J),RPNMPS(I,J),RPCMPW(I,J)
   20 CONTINUE
   30 CONTINUE
C---------CONVERT X AND R FROM INCHES TO METERS
      DO 35 I=1,NSTATN
      X(I)=XINCHS(I)*0.0254
      JPTS=NDATA(I)
      DO 32 J=1,JPTS
      R(J)=RINCHS(J)*0.0254
   32 CONTINUE
   35 CONTINUE
  220 FORMAT(4F10.5)
  230 FORMAT(1F10.5,1I10,1F10.5)
      IF(DIAGNS) WRITE(6,470) (NDATA(I),I=1,NSTATN)
      IF(DIAGNS) WRITE(6,450) (X(I),I=1,NSTATN)
      IF(DIAGNS) WRITE(6,500) (R(J),J=1,JPTS)
      DO 37 I=1,NSTATN
      IF(DIAGNS) WRITE(6,500) (RBETA(I,J),J=1,JPTS)
      IF(DIAGNS) WRITE(6,500) (RPNMPS(I,J),J=1,JPTS)
      IF(DIAGNS) WRITE(6,500) (RPCMPW(I,J),J=1,JPTS)
   37 CONTINUE
  450 FORMAT(///,40X,1(F8.4,1X))
  500 FORMAT(///,20X,10(F8.4))
C
CHAPTER  1  1  1  1  1  DATA REDUCTION  1  1  1  1  1  1
C
  470 FORMAT(///,40X,1(I8,1X))
C---------CALC PICHCF AND INTERPOLATE FOR DELTA FROM
C---------    PITOT CALIBRATION CURVE
      IDID=0
      DO 50 I=1,NSTATN
      JPTS=NDATA(I)
      DO 40 J=1,JPTS
      IF((RPCMPW(I,J) .EQ. 0.0) .AND. (RPNMPS(I,J) .EQ. 0.0)) GO TO 38
      PICHCF(I,J)=RPNMPS(I,J)/(RPCMPW(I,J)+1.E-6)
      IF((PICHCF(I,J).GT.3.399) .OR. (PICHCF(I,J).LT.-3.759)) GO TO 38
      IF(IDID .EQ. 0) DELTA(I,J)=SPLINE(CPITCH,
     #    CDELTA,NCAL,PICHCF(I,J))
      IF(IDID .GT. 0) DELTA(I,J)=SP(CPITCH,CDELTA,
     #    NCAL,PICHCF(I,J))
      IDID=1
      GO TO 40
   38 CONTINUE
```

```
      DELTA(I,J)=0.0
      WRITE(6,850) I,J
  850 FORMAT(20X,'PICHCF IS OUT OF RANGE OF CALIBRATION AT I=
     #',I3,' AND J=',I3)
   40 CONTINUE
   50 CONTINUE
C---------INTERPOLATE FOR VELCF FROM PITOT CALIBRATION DATA
      IDID=0
      DO 80 I=1,NSTATN
      JPTS=NDATA(I)
      DO 70 J=1,JPTS
      IF((RPCMPW(I,J) .EQ. 0.0) .AND. (RPNMPS(I,J) .EQ. 0.0)) GO TO 65
      IF((ABS(DELTA(I,J))) .GT. 58.0) GO TO 65
      IF(IDID .EQ. 0) VELCF(I,J)=SPLINE(CDELTA,
     #CVELCF,NCAL,DELTA(I,J))
      IF(IDID .GT. 0) VELCF(I,J)=SP(CDELTA,CVELCF,
     #NCAL,DELTA(I,J))
      IDID=1
      GO TO 70
   65 CONTINUE
      VELCF(I,J)=0.0
      WRITE(6,890) I,J
  890 FORMAT(20X,'DELTA IS OUT OF RANGE OF CALIBRATION DATA
     #AT I=',I3,' AND J=',I3)
   70 CONTINUE
   80 CONTINUE
      DO 85 I=1,NSTATN
      IF(DIAGNS) WRITE(6,500) (PICHCF(I,J),J=1,JPTS)
      IF(DIAGNS) WRITE(6,500) (DELTA(I,J),J=1,JPTS)
      IF(DIAGNS) WRITE(6,500) (VELCF(I,J),J=1,JPTS)
   85 CONTINUE
C---------CALC MAGNITUDE OF TOTAL MEAN VELOCITY VECTOR AND
C---------     U, V, & W COMPONENTS
      RHO=PATM*(136.0/0.102)/(287.0*(TATM+273.0))
      PI=3.14159
      DO 100 I=1,NSTATN
      JPTS=NDATA(I)
      DO 90 J=1,JPTS
      BETA(I,J)=360.-RBETA(I,J)
      IF((RPCMPW(I,J).EQ.0.0) .AND. (RPNMPS(I,J).EQ.0.0)) BETA(I,J)=0.0
      VTOTAL(I,J)=SQRT(ABS(2.0/RHO*VELCF(I,J)*RPCMPW(I,J)*133.9))
      U(I,J)=VTOTAL(I,J) * COS(DELTA(I,J)*PI/180.0) *
     #    COS(BETA(I,J)*PI/180.0)
      V(I,J)=VTOTAL(I,J) * SIN(DELTA(I,J)*PI/180.0)
      W(I,J)=VTOTAL(I,J) * COS(DELTA(I,J)*PI/180.0) *
     #    SIN(BETA(I,J)*PI/180.0)
   90 CONTINUE
  100 CONTINUE
      IF(DIAGNS) WRITE(6,500)(VTOTAL(I,J),J=1,JPTS)
      IF(DIAGNS) WRITE(6,500)(U(I,J),J=1,JPTS)
      IF(DIAGNS) WRITE(6,500)(V(I,J),J=1,JPTS)
      IF(DIAGNS) WRITE(6,500)(W(I,J),J=1,JPTS)
CHAPTER  2  2  2  2  2  2  AUXILIARY CALCULATIONS  2  2  2  2  2
C
      DO 130 I=1,NSTATN
C---------CALC GEOMETRIC QUANTITIES
      JPTS=NDATA(I)
      JPTSM1=JPTS-1
      DYPS(1)=0.0
      DYNP(JPTS)=2.0*(RLARGE-R(JPTS))
      DO 110 J=1,JPTSM1
      DYNP(J)=R(J+1)-R(J)
      DYPS(J+1)=DYNP(J)
  110 CONTINUE
      DO 115 J=1,JPTS
      SNS(J)=0.5*(DYNP(J)+DYPS(J))
  115 CONTINUE
      IF(DIAGNS) WRITE(6,500) (DYNP(J),J=1,JPTS)
      IF(DIAGNS) WRITE(6,500) (SNS(J),J=1,JPTS)
      FLOW=0.0
      WMOM=0.0
      DO 120 J=1,JPTS
      ARDEN=RHO*R(J)*SNS(J)
```

```
      WMOM=WMOM+ARDEN*U(I,J)*W(I,J)*R(J)
      FLOW=FLOW+ARDEN*U(I,J)
      IF(DIAGNS) WRITE(6,900) J,FLOW,ARDEN,WMOM,RHO
  900 FORMAT(///,I5,4(F12.4,2X))
  120 CONTINUE
      ANGMOM(I)=WMOM
      MASS(I)=2.0*PI*FLOW
      UMEAN(I)=MASS(I)/(RHO*PI*RLARGE**2)
  130 CONTINUE
      IF(DIAGNS) WRITE(6,450) (UMEAN(I),I=1,NSTATN)
      IF(DIAGNS) WRITE(6,450) (MASS(I),I=1,NSTATN)
C----------NONDIMENSIONALIZE VELOCITIES
      DO 150 I=1,NSTATN
      XND(I)=X(I)/(2.0*RLARGE)
      JPTS=NDATA(I)
      UIN(I)=(SQRT(2.0/RHO*RDNPRS(I)*249.08))*(6.312/5.94)**2
      MASFLO(I)=2.0*PI*RHO*UIN(I)*RSMALL**2/2.0
      DO 140 J=1,JPTS
      VTSTAR(I,J)=VTOTAL(I,J)/UIN(I)
      USTAR(I,J)=U(I,J)/UIN(I)
      VSTAR(I,J)=V(I,J)/UIN(I)
      WSTAR(I,J)=W(I,J)/UIN(I)
  140 CONTINUE
  150 CONTINUE
      DO 160 J=1,MAXJPT
      RND(J)=R(J)/(2.0*RLARGE)
  160 CONTINUE
C
CHAPTER  3  3  3  3  3  OUTPUT  3  3  3  3  3  3  3
C
      IF(.NOT. IWRITE) GO TO 165
      WRITE(11) X
      WRITE(11) R
      WRITE(11) U
      WRITE(11) V
      WRITE(11) W
  165 CONTINUE
      WRITE(6,311)
      WRITE(6,325) ALPHA
      WRITE(6,330) PHI
      WRITE(6,335) RSMALL
      WRITE(6,340) RLARGE
      WRITE(6,355) VISCOS
      WRITE(6,360) RHO
C
      CALL WRITE(1,1,NSTATN,1,IT,JT,X,R,MASFLO,HEDMMF)
      CALL WRITE(1,1,NSTATN,1,IT,JT,X,R,MASS,HEDM)
      CALL WRITE(1,1,NSTATN,1,IT,JT,X,R,UIN,HEDMIV)
      CALL WRITE(1,1,NSTATN,1,IT,JT,X,R,UMEAN,HEDUMN)
      CALL WRITE(1,1,NSTATN,1,IT,JT,X,R,ANGMOM,HEDAM)
      CALL PRINT(1,1,NSTATN,MAXJPT,IT,JT,X,R,U,HEDU)
      CALL PRINT(1,1,NSTATN,MAXJPT,IT,JT,X,R,V,HEDV)
      CALL PRINT(1,1,NSTATN,MAXJPT,IT,JT,X,R,W,HEDW)
      CALL PRINT(1,1,NSTATN,MAXJPT,IT,JT,X,R,DELTA,HEDDEL)
      CALL PRINT(1,1,NSTATN,MAXJPT,IT,JT,X,R,BETA,HEDBET)
      CALL PRINT(1,1,NSTATN,MAXJPT,IT,JT,X,R,VTOTAL,HEDVT)
      CALL PRINT(1,1,NSTATN,MAXJPT,IT,JT,XND,RND,USTAR,HEDUST)
      CALL PRINT(1,1,NSTATN,MAXJPT,IT,JT,XND,RND,VSTAR,HEDVST)
      CALL PRINT(1,1,NSTATN,MAXJPT,IT,JT,XND,RND,WSTAR,HEDWST)
      CALL PRINT(1,1,NSTATN,MAXJPT,IT,JT,XND,RND,VTSTAR,HEDVTS)
      CALL PRINT(1,1,NSTATN,MAXJPT,IT,JT,XINCHS,RINCHS,RPNMPS,HEDNMS)
      CALL PRINT(1,1,NSTATN,MAXJPT,IT,JT,XINCHS,RINCHS,RPCMPW,HEDCMW)
      CALL WRITE(1,1,NSTATN,1,IT,JT,XINCHS,RINCHS,RDNPRS,HEDMIP)
      CALL PRINT(1,1,NSTATN,MAXJPT,IT,JT,XINCHS,RINCHS,FICHCF,HEDMPP)
      STOP
C---------FORMAT STATEMENTS
  311 FORMAT(1H1,T37,'AXISYMMETRIC,ISOTHERMAL, GT COMBUSTOR FLOWFIELD
     *MEASUREMENTS',//,T53,'USING A FIVE-HOLE PITOT PROBE')
  325 FORMAT(////,T40,'EXPANSION ANGLE(DEG.) =',T77,1PE13.3)
  330 FORMAT(//,T40,'SWIRL VANE ANGLE(DEG.) =',T77,1PE13.3)
  335 FORMAT (//,T40,'INLET RADIUS(M) =',T77,1PE13.3)
  340 FORMAT(//,T40,'COMBUSTOR RADIUS(M) =',T77,1PE13.3)
  355 FORMAT(//,T40,'LAMINAR VISCOSITY(KG/M/SEC) =',T77,1PE13.3)
```

```
  360 FORMAT(//,T40,'DENSITY(KG/CU. M) =',T77,1PE13.3,////)
      END
C
      SUBROUTINE INIT
C*****************************************************************
C
      COMMON
     #/MEASUR/RBETA(48,24),RPNMPS(48,24),RPCMPW(48,24),NDATA(48),MAXJPT,
     #    RDNPRS(48)
     #/GEOM/X(48),R(24),XND(48),RND(24),DYPS(24),DYNP(24),
     #    SNS(24),NSTATN,XINCHS(48),RINCHS(24)
     #/CALC/VTOTAL(48,24),U(48,24),V(48,24),W(48,24),
     #    VTSTAR(48,24),USTAR(48,24),VSTAR(48,24),WSTAR(48,24),
     #    PICHCF(48,24),VELCF(48,24),DELTA(48,24),BETA(48,24),
     #     ANGMOM(48),UMEAN(48),MASS(48),MASFLO(48),UIN(48)
      REAL MASS,MASFLO
C
      DO 20 I=1,NSTATN
      MASFLO(I)=0.0
      MASS(I)=0.0
      ANGMOM(I)=0.0
      UMEAN(I)=0.0
      UIN(I)=0.0
      DO 10 J=1,MAXJPT
      VTOTAL(I,J)=0.0
      U(I,J)=0.0
      V(I,J)=0.0
      W(I,J)=0.0
      VTSTAR(I,J)=0.0
      USTAR(I,J)=0.0
      VSTAR(I,J)=0.0
      WSTAR(I,J)=0.0
      RBETA(I,J)=0.0
      BETA(I,J)=0.0
      RPNMPS(I,J)=0.0
      RPCMPW(I,J)=0.0
      PICHCF(I,J)=0.0
      VELCF(I,J)=0.0
      DELTA(I,J)=0.0
   10 CONTINUE
   20 CONTINUE
      RETURN
      END
C
      FUNCTION SPLINE(X, FX, N, X1)
C*****************************************************************
C     CUBIC SPLINE CURVE FITTING IN 2 DIMENSIONAL DATA PLANE
C     INPUT VALUES :
C     X, FX      DATA ARRAYS, ONE DIMENSIONAL, X IN INCREASING ORDER
C     N          NUMBER OF DATA POINTS IN X, MAX 26
C     X1         POINT OF INTEREST, WHERE F(X1) IS TO BE FOUND
C
C     RETURN VALUE :
C     SPLINE OR SP = F(X1)
C     THIS ROUTINE ACTIVATES ROUTINE ABUILD, H, AND GAUSS.
C     FOR INTERPOLATION OF A LARGE NUMBER OF DATA POINTS, FUNCTION
C     SPLINE MAY BE CALLED ONLY ONCE , AND SUBSEQUENT CALLS MAY USE
C     ENTRY POINT SP.
C*****************************************************************
      DIMENSION X(1), FX(1), A(26,27)
C---------CONSTRUCT SPLINE MATRIX
      N1=N+1
      DO 10  I=1, N
      DO 10  J=1, N1
10    A(I,J)=0.
      M1=N-1
      DO 20  I=2, M1
20    CALL ABUILD(X, FX, A, N, I)
      A(1,1)=H(X,2)
      A(1,2)=-H(X,1)-H(X,2)
      A(1,3)=H(X,1)
      M2=N-2
      A(N,M2)=H(X,M1)
```

```
      A(N,M1)=-H(X,M2)-H(X,M1)
      A(N,N)=H(X,M2)
C---------FIND SECOND DERIVATIVES
      CALL GAUSS(A, N, N1)
      ENTRY SP(X, FX, N, X1)
C---------FIND F(X1)
      DO 40  I=1, M1
      I1=I+1
      IF(X1 .EQ. X(I)) GO TO 50
      IF(X1 .LT. X(I) .AND. X1 .GT. X(I1)) GO TO 41
      IF(X1 .GT. X(I) .AND. X1 .LT. X(I1) ) GO TO 41
40    CONTINUE
      IF(X1 .EQ. X(N)) GO TO 60
      WRITE(6, 42) X1
42    FORMAT(' X1=', G14.7, ' OUT OF INTERPOLATION RANGE, RETURNED VALUE
     *=0')
      SP=0.
      SPLINE=0.
      STOP
41    CONTINUE
      I1=I+1
      HI=H(X,I)
      HX=X(I1)-X1
      HX2=X1-X(I)
      FX1=HX**3/HI-HI*HX
      FX1=FX1*A(I,N1)
      STO=HX2**3/HI - HI*HX2
      FX1=(FX1+STO*A(I1,N1) )/6.
      SPLINE=(FX(I)*HX+FX(I1)*HX2)/HI+FX1
      SP=SPLINE
      RETURN
C
50    CONTINUE
      SPLINE=FX(I)
      SP=SPLINE
      RETURN
C
60    CONTINUE
      SPLINE=FX(N)
      SP=SPLINE
      RETURN
      END
C
      FUNCTION H(X,I)
C*********************************************************************
C     CALCULATE DELTA X WHICH IS USUALLY CALLED AS H.
C*********************************************************************
      DIMENSION X(1)
      I1=I+1
      H=X(I1)-X(I)
      RETURN
      END
C
      SUBROUTINE ABUILD(X, F, A, N, I)
C*********************************************************************
C     CONSTRUCT  SPLINE MATRIX FOR FINDING 2ND DERIVATIVES.
C*********************************************************************
      DIMENSION X(1), F(1), A(26,27)
      IM1=I-1
      I1=I+1
      N1=N+1
      STO=H(X,I)
      HIM1=H(X,IM1)
      A(I,IM1)=HIM1
      A(I,I)=2.*(HIM1+STO)
      A(I,I1)=STO
      A(I,N1)=( (F(I1)-F(I))/STO - (F(I)-F(IM1))/HIM1 )*6.
      RETURN
      END
C
      SUBROUTINE GAUSS(A, K, M)
C*********************************************************************
C     GAUSS-JORDAN ELIMINATION
```

```
C*********************************************************************
      DIMENSION A(26,27)
      M1=M-1
      K1=K-1
      DO 3  L=1, K1
      L1=L+1
      DO 3  I=L1, K
      CONST=A(I,L)/A(L,L)
      DO 3  J=L, M
3     A(I,J)=A(I,J)-CONST*A(L,J)
      DO 6 I=1, K1
      I1=I+1
      DO 6  L=I1, M1
      CONST=A(I,L)/A(L,L)
      DO 6  J=I, M
6     A(I,J)=A(I,J)-CONST*A(L,J)
      DO 10  I=1, K
      A(I,M)=A(I,M)/A(I,I)
10    A(I,I)=1.
      RETURN
      END
C
      SUBROUTINE PRINT(ISTART,JSTART,NI,NJ,IT,JT,X,Y,PHI,HEAD)
CA*********************************************************************
C
      DIMENSION PHI(IT,JT),X(IT),Y(JT),HEAD(9),STORE(48)
      ISKIP=1
      JSKIP=1
      WRITE(6,110)HEAD
      ISTA=ISTART-12
  100 CONTINUE
      ISTA=ISTA+12
      IEND=ISTA+11
      IF(NI.LT.IEND)IEND=NI
      WRITE(6,111)(I,I=ISTA,IEND,ISKIP)
      WRITE(6,114)(X(I),I=ISTA,IEND,ISKIP)
      WRITE(6,112)
      DO 101 JJ=JSTART,NJ,JSKIP
      J=JSTART+NJ-JJ
      DO 120 I=ISTA,IEND
      A=PHI(I,J)
      IF(ABS(A).LT.1.E-20) A=0.0
120   STORE(I)=A
  101 WRITE(6,113)J,Y(J),(STORE(I),I=ISTA,IEND,ISKIP)
      IF(IEND.LT.NI)GO TO 100
      RETURN
  110 FORMAT(1H0,17(2H*-),7X,9A4,7X,17(2H-*))
  111 FORMAT(1H0,13H       I =     ,I2,11I9)
  112 FORMAT(8H0 J     Y)
  113 FORMAT(I3,0PF8.5,1X,1P12E9.2)
  114 FORMAT(11H        X = ,F8.5,11F9.5)
      END
C
      SUBROUTINE WRITE(ISTART,JSTART,NI,NJ,IT,JT,X,Y,PHI,HEAD)
CA*********************************************************************
C
      DIMENSION PHI(IT),X(IT),Y(JT),HEAD(9),STORE(48)
      ISKIP=1
      JSKIP=1
      WRITE(6,110)HEAD
      ISTA=ISTART-12
  100 CONTINUE
      ISTA=ISTA+12
      IEND=ISTA+11
      IF(NI.LT.IEND)IEND=NI
      WRITE(6,111)(I,I=ISTA,IEND,ISKIP)
      WRITE(6,114)(X(I),I=ISTA,IEND,ISKIP)
      DO 101 JJ=JSTART,NJ,JSKIP
      J=JSTART+NJ-JJ
      DO 120 I=ISTA,IEND
      A=PHI(I)
      IF(ABS(A).LT.1.E-20) A=0.0
120   STORE(I)=A
```

```
  101 WRITE(6,113) (STORE(I),I=ISTA,IEND,ISKIP)
      IF(IEND.LT.NI)GO TO 100
      RETURN
  110 FORMAT(1H0,17(2H*-),7X,9A4,7X,17(2H-*))
  111 FORMAT(1H0,13H       I =     ,I2,11I9)
  113 FORMAT(12X,1P12E9.2)
  114 FORMAT(11H        X = ,F8.5,11F9.5)
C
      END
```

1. Report No.	2. Government Accession No.	3. Recipient's Catalog No.
NASA CR-174916		

4. Title and Subtitle	5. Report Date
Predictions and Measurements of Isothermal Flowfields in Axisymmetric Combustor Geometries	May 1985
	6. Performing Organization Code
7. Author(s)	8. Performing Organization Report No.
D.L. Rhode and D.G. Lilley	None
	10. Work Unit No.
9. Performing Organization Name and Address	11. Contract or Grant No.
Oklahoma State University School of Mech. and Aerospace Engineering Stillwater, Oklahoma 74074	NAG 3-74
	13. Type of Report and Period Covered
12. Sponsoring Agency Name and Address	Contractor Report
National Aeronautics and Space Administration Washington, D.C. 20546	14. Sponsoring Agency Code
	533-04-1A

15. Supplementary Notes

Final report. Project Manager, James D. Holdeman, Internal Fluid Mechanics Division, NASA Lewis Research Center, Cleveland, Ohio 44135. This report was a dissertation submitted by D.L. Rhode to the Faculty of the Graduate School of Oklahoma State University in partial fulfillment of the requirements for the degree Doctor of Philosophy in December 1981.

16. Abstract

Numerical predictions, flow visualization experiments and time-mean velocity measurements were obtained for six basic nonreacting flowfields (with inlet swirl vane angles of 0 (swirler removed), 45 and 70 degrees and sidewall expansion angles of 90 and 45 degrees) in an idealized axisymmetric combustor geometry. A flowfield prediction computer program was developed which solves appropriate finite difference equations including a conventional two-equation k-ε eddy viscosity turbulence model. The wall functions employed were derived from previous swirling flow measurements, and the stairstep approximation was employed to represent the sloping wall at the inlet to the test chamber. Recirculation region boundaries have been sketched from the entire flow visualization photograph collection. Tufts, smoke, and neutrally-buoyant helium-filled soap bubbles were employed as flow tracers. Further, a five-hole pitot probe was utilized to measure the axial, radial, and swirl time-mean velocity components.

17. Key Words (Suggested by Author(s))	18. Distribution Statement
Combustor; Swirl; Turbulent flow; Axisymmetric; Prediction; Flow visualization experiments; Velocity measurements	Unclassified - unlimited STAR Category 07

19. Security Classif. (of this report)	20. Security Classif. (of this page)	21. No. of pages	22. Price*
Unclassified	Unclassified	169	A08

*For sale by the National Technical Information Service, Springfield, Virginia 22161